

Jupiter Europa Orbiter Mission Study 2008

Assessment of Radiation Effects on Science and Engineering Detectors for the JEO Mission Study

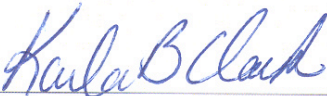
Rev. A

Primary Contributors:

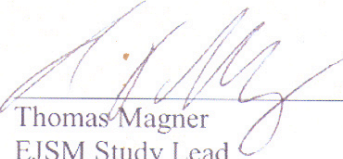
John Boldt, APL, Lead
James W. Alexander, JPL
Heidi Becker, JPL
Edward Blazejewski, JPL
E. Hugo Darlington, APL
Clifford Frez, JPL

Siamak Forouhar, JPL
Paula Grunthaner, JPL
Dennis Haggerty, APL
Insoo Jun, JPL
Dave Roth, APL

Approved by:



Karla Clark Date
EJSM Study Lead
California Institute of Technology
Jet Propulsion Laboratory

 10/30/08

Thomas Magner Date
EJSM Study Lead
Applied Physics Laboratory
Johns Hopkins University

Paper copies of this document may not be current and should not be relied upon for official purposes. The current version is available from a link in the JEO DocuShare Library: <https://www.alpha-lib.jpl.nasa.gov/docushare/dsweb/View/Collection-77606>

Information included herein is controlled under the International Traffic in Arms Regulations (ITAR) by the U.S. Department of State. Export of transfer of this information to a foreign person or foreign entity requires an export license by the U.S. State Department or an ITAR exemption prior to the export or transfer.

APL

November 3, 2008
JPL D-48256

JPL

TABLE OF CONTENTS

1.	Executive Summary	1-1
2.	Introduction.....	2-1
2.1	JEO Detector Working Group.....	2-1
2.2	Notional Detectors for the JEO Planning Payload	2-1
2.3	Overview of Radiation Risks to Photonic Detectors and Components.....	2-3
3.	External Radiation Environment	3-1
4.	Radiation Environment Behind the Nominal Shield	4-1
4.1	First-Order Model.....	4-1
4.2	Detector Response to Single Event Effects	4-2
4.3	Ongoing Modeling Effort.....	4-3
4.4	Future Effort	4-4
5.	Visible Detector Technology	5-1
5.1	Charge Coupled Devices	5-1
5.1.1	Total Dose and Displacement Dose Survivability	5-2
5.1.2	Transient Effects.....	5-8
5.1.3	Mitigation Techniques.....	5-10
5.1.4	Planetary Protection	5-10
5.1.5	Overall Assessment	5-11
5.2	CMOS Imagers or Active Pixel Sensors	5-11
5.2.1	Total Dose and Displacement Dose Survivability	5-12
5.2.2	Transient Effects.....	5-18
5.2.3	Mitigation Techniques.....	5-19
5.2.4	Planetary Protection	5-19
5.2.5	Overall Assessment	5-19
5.3	Performance of the CCD Imager in the Galileo Solid-State Imaging System	5-20
5.3.1	Introduction	5-20
5.3.2	Radiation Effects	5-21
5.3.3	Summary	5-25
6.	Infrared Detector Technology	6-1
6.1	MWIR Focal Plane Arrays	6-1
6.1.1	Total Dose and Displacement Dose Survivability	6-2
6.1.2	Transient Effects.....	6-6
6.1.3	Mitigation Techniques.....	6-9
6.1.4	Planetary Protection	6-11
6.1.5	Overall Assessment	6-12
6.2	Thermal Detector Arrays	6-13
6.2.1	Total Dose and Displacement Dose Survivability	6-14
6.2.2	Transient Response.....	6-15

6.2.3	Mitigation Techniques.....	6-15
6.2.4	Planetary Protection	6-16
6.2.5	Overall Assessment	6-16
7.	Avalanche Photodiodes.....	7-1
7.1	Radiation Environment and Effects on APDs	7-1
7.2	APD Detector Survivability	7-2
7.3	Transient Effects.....	7-2
7.4	Planetary Protection	7-3
7.5	Overall Assessment	7-3
8.	Photomultipliers and Microchannel Plates	8-1
8.1	Total Dose Survivability	8-1
8.2	Transient Effects.....	8-2
8.3	Planetary Protection	8-2
8.4	Overall Assessment	8-2
9.	Lasers and Laser-Related Components.....	9-1
9.1	GaAs Diode Pump Laser	9-1
9.2	Nd:YAG Crystal.....	9-2
9.3	LiNbO ₃ Q-Switching Component	9-3
9.4	Optical Fibers	9-3
9.5	Transient Effects.....	9-4
9.6	Planetary Protection	9-4
9.7	Overall Assessment	9-4
10.	Stellar Reference Unit.....	10-1
10.1	System Overview	10-1
10.2	Radiation Environment and Effects on SRU.....	10-1
10.3	SRU Detector Survivability.....	10-2
10.3.1	SRU Detector Technologies and Associated Radiation Effects.....	10-2
10.3.2	Existing SRU Products	10-3
10.4	Transient Mitigation Approaches.....	10-4
10.4.1	Expected Transient Noise Contribution	10-4
10.4.2	Algorithmic Mitigation for Initialization and Acquisition	10-5
10.4.3	System-Level Mitigation for Tracking on Approach to JOI	10-6
10.4.4	Algorithmic Mitigation Approaches for Tracking	10-6
10.4.5	Hardware Mitigation Approaches (Associated Trades)	10-7
10.6	Planetary Protection	10-7
10.7	Overall Assessment	10-7
11.	Feasibility of the JEO Notional Payload Detectors.....	11-1
11.1	Science Detectors	11-1
11.2	Stellar Reference Unit	11-6
11.3	Test as You Fly.....	11-6

1 Executive Summary

The NASA Review Board for the 2007 Europa Explorer Study concluded that a compelling case had not been made for the suitability of existing detector technologies given the harsh radiation environment of Europa. For the follow-on 2008 Europa Orbiter Study, a Detector Working Group (DWG) was created to assess the new notional payload and determine if a feasible pathway exists for known technologies to satisfy science measurement requirements.

The DWG was comprised of experienced instrument, detector, and radiation environment experts from the Applied Physics Laboratory at John Hopkins University and the Jet Propulsion Laboratory. For each detector and key component technology required for the notional payload, the key tasks for the DWG included (a) reviewing available radiation literature and test reports, (b) estimating the radiation environment seen by a detector behind its shield and (c) assessing the total dose survivability (both ionizing and displacement damage) and radiation-induced transient noise effects. The DWG examined each of the detector technologies needed by the notional payload and stellar reference unit—visible detectors, mid-infrared and thermal infrared detectors, microchannel plates and photomultipliers, avalanche photodiodes, and laser-related components (diode laser, solid-state laser and associated components, fiber optics).

The high-energy electrons and protons in the Jupiter magnetosphere are the dominating contributors for the life-limiting total ionizing dose (TID) and displacement damage dose (DDD) effects as well as the radiation-induced transient noise effects. TID and DDD are integral effects that build with time and degrade the performance of a component until it no longer meets science requirements or possibly fails entirely. Radiation-induced transient noise is a result of particles striking a detector and creating signal carriers. During

periods when the spacecraft is traversing through high particle flux, a detector system can be swamped by excess noise.

In order to evaluate the total dose and transient noise impact on a given detector technology, two topics were addressed: (i) the radiation environment at the detector behind radiation shields of various thicknesses and (ii) the response of the active volume of the detector to the incident electrons, protons, and photons.

For this study, the end-of-mission TID and DDD incident on a detector were determined using well-understood dose-depth curves. Electron and proton fluxes (particles/cm²-s) incident on the detector during Europa orbit and Io fly-by were estimated using the integral flux of external particles at the minimum energy needed to penetrate a given shield thickness. Several different shield thicknesses were explored in order to allow for trade of radiation effects and shielding mass.

The response of the active volume of a detector to particles is a complicated problem that requires significant modeling and validation. A comprehensive Monte Carlo modeling effort is underway and will be completed in FY 2009. For the near term needs of this study, there is enough empirical information to determine worst-case estimates of the effects of electrons and protons incident on the various notional detector technologies for the payload. Where experimental data exists, it compares well with the DWG estimate on the magnitude of detector response.

The DWG concludes that the radiation and challenges facing the JEO notional payload, SRU detectors and laser components are well understood. A comprehensive review of the literature and available test reports were used to establish the nominal total dose tolerance that can be expected for each technology. With the recommended shielding allocations, the total dose survivability of these

components is not considered to be a significant risk for JEO. In many cases, the shielding allocation was driven not by total dose survivability, but by the need to reduce radiation-induced transient noise effects to meet science and engineering performance requirements in the high particle flux environment at Europa. For these technologies—notably mid-infrared detectors, avalanche photodiode detectors, and visible detectors for star tracking—extensive shielding (up to ~3-cm-thick Ta) for transient noise reduction effectively mitigates all concern over total dose degradation. For the remaining technologies, more modest shielding thicknesses (0.3–1.0 cm Ta, depending upon the specific technology) were judged to be sufficient to reduce the total dose exposure and transient noise effects.

For all detector technologies, the recommended shielding allocations were intended to be used in concert with other well-established mitigation techniques such as detector design, detector operational parameters, algorithmic approaches and instrument-level mitigations. There is no intent to imply that the particular detector mitigation techniques used by the notional payload (*see 2008 Jupiter Orbiter Study Report, D-48279*) represent a unique solution and different instruments or different point designs may likely find their “sweet spot” at a different point in the mitigations trade space.

The transient noise assessment was performed for the flux conditions for Europa orbit. The particle flux received during Io fly-by will be a factor of approximately eight higher. The DWG believes there is adequate trade space between additional shielding, detector exposure times and signal from the higher albedo of Io to acceptably mitigate transient noise effects during Io fly-by. A complete analysis should be performed in the future taking into account the different instrument operational parameters that are

required for fly-by as compared to orbital observations.

The DWG also concludes that the challenges facing the payload detectors with respect to the desired planetary protection protocol of dry heat sterilization are well understood. The detector active materials themselves are expected to tolerate dry heat sterilization, provided that appropriate attention is given to ensuring that device packaging (i.e. adhesives, optical coatings, thermo-electric coolers) is likewise tolerant. The one exception is HgCdTe detector technology and, while a bake-out protocol is now used for military applications, it must be qualified for JEO’s mid-wavelength IR scientific application to confirm that performance is not degraded by the heat treatment.

The DWG recommends caution in inferring detector performance in the Jovian environment based on existing radiation test results where the irradiation species is typically not representative of JEO’s expected flight spectra. A rigorous test-as-you-fly policy with respect to detector radiation testing, including irradiation with flight-representative species and energies for TID, DDD, and transient testing, should be adopted for JEO.

2 Introduction

The scientific and engineering instruments on a mission to explore Europa and the Jupiter system must be able to withstand exposure to the harsh radiation environment without excessive degradation in performance. Radiation-induced effects on photonic detectors and other key photonic elements pose significant risk to the quality and quantity of the mission science return as well as the reliability of the engineering sensor data critical to flight operations. The NASA Technical, Management, and Cost Review Board for the 2007 Europa Explorer Mission Study Report concluded, among other findings, that a compelling case had not been made for the suitability of existing detector technologies in terms of radiation total dose survivability or transient radiation-induced detector noise impact.

In December of 2007, NASA requested a phase-2 study for a possible joint NASA/ESA Europa–Jupiter System Mission (EJSM). The NASA-led element of this mission, the Jupiter Europa Orbiter (JEO), addresses a very rich subset of the EJSM science objectives with a comprehensive notional planning payload. The JEO Detector Working Group (DWG) was formed and chartered to assess whether a feasible pathway exists for detectors and key components unique to the planning payload described in the 2008 JEO Study Report. The purpose of this document is to summarize the findings of the DWG.

2.1 JEO Detector Working Group

A joint working group was established with participants from the Applied Physics Laboratory (APL) at John Hopkins University and the Jet Propulsion Laboratory (JPL). The joint APL/JPL DWG consisted of experienced instrument, detector, and radiation environment experts knowledgeable of current detector technologies and technologies in development. When needed, the DWG sought

additional expertise. The DWG was charged with the following goal.

Assess the radiation susceptibility of the photonic detector and key component technologies required by (i) the notional planning payload established by the EJSM Joint Jupiter Science Definition Team (JJSdT) and (ii) and the spacecraft stellar reference unit.

Specific tasks include:

- Identify the notional planning detector and component technologies
- Review available radiation test reports and literature for each technology
- Model the radiation environment incident on the detector and components behind appropriate shielding for the JEO mission design
- Assess the impact of total ionizing dose and displacement damage dose on performance for each technology
- Assess the radiation-induced transient noise for selected detectors
- Recommend future testing when existing data is not representative of JEO mission conditions

In addition, the DWG was asked to assess whether the notional detector technologies would be tolerant of the planetary protection protocols base-lined for JEO.

2.2 Notional Detectors for the JEO Planning Payload

An international NASA/ESA Joint Jupiter Science Definition Team (JJSdT) defined the science requirements for the NASA JEO mission study and provided the science traceability to the planning payload summarized in [Table 2–1](#). Extensive discussion of the science traceability to this planning payload may be found elsewhere [*JEO 2008 Study Report, D-49279*].

For the purposes of this detector assessment, this planning payload, while only

notional, is used to establish the detectors and key component technologies to be included in the radiation assessment in order to demonstrate a feasible pathway to acceptable

detector performance in the JEO mission radiation environment. The information provided in this assessment should not be taken as a final selection for a particular

Table 2–1: Summary of detector and key component technologies required by the JEO planning payload and engineering sensors.

Instrument	Acronym	Detector and Key Component Technologies	Similar Instruments
Ocean Team			
Radio Science	RS	No active photonic detector	
Laser Altimeter	LA	Avalanche photodiode GaAs diode laser (809 nm) Nd:YAG laser (1.064 μm) Fiber optics	NEAR NLR LRO LOLA
Ice Team			
Ice Penetrating Radar	IPR	No active photonic detector	ME MARSIS MRO SHARAD
Chemistry Team			
Vis-IR Imaging Spectrometer	VIRIS	HgCdTe (400–5200 nm)	MRO CRISM Chandrayaan MMM
UV Spectrometer	UVS	Micro-channel plate	Cassini UVIS New Horizons Alice Juno UVS
Ion and Neutral Mass Spectrometer	INMS	Micro-channel plate	Rosina RTOF
Geology Team			
Wide Angle Camera and Medium Angle Camera	WAC + MAC	CMOS or CCD	MRO MARCI MESSENGER MDIS New Horizons MVIC
Narrow Angle Camera	NAC	CMOS or CCD	LRO LROC New Horizons LORRI
Thermal Instrument	TI	Thermopiles	MRO CTX LRO Diviner
Fields and Particles Team			
Magnetometer	MAG	No active photonic detector	MESSENGER MAG Galileo MAG Juno MAG
Particle and Plasma Instrument	PPI	Micro-channel plate	DSI PEPE MESSENGER FIPS Juno JADE & JEDI New Horizons PEPSSI
Spacecraft Engineering			
Stellar reference unit	SRU	CMOS or CCD	JUNO SRU

detector technology, nor is there any intent to imply that specific technologies are fully viable as currently implemented.

2.3 Overview of Radiation Risks to Photonic Detectors and Components

Energetic particles passing through matter lose kinetic energy through a variety of interactions and scattering mechanisms and, as a result, produce a wide variety of effects in different material and device structures. Serious degradation effects in devices occur primarily as a result of two interaction mechanisms— ionization, which creates electron-hole pairs via the disruption of electronic bonds in the material, and displacement, which creates lattice defects via displaced atoms and the vacancies left behind. Energetic particles transversing a material lose most of their energy to ionization and the term “total ionizing dose” (TID) is used to refer to the ionizing radiation exposure due to this fraction. TID is typically measured in rads or Grays (1 Gy = 100 rads). A smaller amount of energy is lost as “non-ionizing energy loss”, the major element of which is atomic displacement. The term “displacement damage dose” (DDD) is used to refer to the non-ionizing radiation exposure. DDD is measured in units of MeV/g.

The performance degradation effects of TID and DDD are integral effects. Total dose builds with time as the mission progresses and the performance of the device degrades with time until it is no longer able to meet science performance requirements or even fails entirely. TID and DDD effects in photonic imagers include flat band voltage shifts, increased dark current, increased dark current non-uniformities, reduced responsivity, creation of “hot pixels”, and many other surface and interface related degradation. Other key components such as lasing crystals and fiber optics are susceptible to such effects as loss of transmission (optical darkening) due to defect centers. The type of degradation and

the magnitude of the degradation depend greatly upon the device technology— types of materials, details of the device structure, how the device is operated and the conditions under which it is operated. The intent of this study is not an exhaustive review of all possible devices and operating conditions, but rather a selected overview of currently available technologies and the feasibility of these technologies to meet the JEO mission needs using conventional radiation mitigation strategies.

Radiation-induced transient effects are as important to understand as the total dose degradation effects discussed above. The external environment can cause Single Event Effects (SEE) in detector and electronic components. Particles and Bremsstrahlung photons striking the detector active area will register like image signal electrons and appear as an output signal voltage proportional to the charge collected. Electron or photon “hits” due to the background radiation will appear as momentary spikes across multiple pixels and proton “hits” can “white out” multiple pixels. These transient effects are unlikely to cause any long-term degradation of the device, but can seriously impact the signal/noise ratio of the instrument. High rates of SEEs may swamp a detector system during periods when the spacecraft is traversing a high flux portion of the environment.

In §3 and §4, the external radiation environment and the environment at the detector level behind various shielding thicknesses are discussed. Subsequent sections examine each of the component technologies needed by the notional payload— visible detectors, mid-infrared and thermal infrared detectors, micro-channel plates and photomultipliers, and laser-related technologies. These technologies are assessed in terms of their survivability to total dose effects, impact of transient effects, and tolerance to planetary protection protocols.

3 External Radiation Environment

The JEO mission would be subjected to four major radiation environment sources: (1) solar energetic particles (protons, electrons, and heavy ions) during the interplanetary cruise, (2) galactic cosmic rays (protons and heavy ions) during the interplanetary cruise, (3) trapped particles (electrons, protons, and heavy ions) in the Jovian magnetosphere during the Jupiter tour and the orbits at Europa, and (4) particles (neutrons and gammas) from the onboard nuclear power source.

Among these, the high-energy electrons and protons at Jupiter are the dominating contributors for the life-limiting TID and DDD effects as well as for the radiation-induced noise transient effects in the scientific and engineering sensors. Thus, the discussion here will be focused on defining the Jovian radiation environments for the notional JEO mission.

Figure 3–1 shows the reference TID depth curve for the JEO 2008 mission concept as a function of aluminum spherical shell thickness. As shown, the 2008 reference mission expects to accumulate 2.9 Mrad (Si) behind a 100-mil (2.5 mm) shell of aluminum

at the end of Europa Campaign 3 (corresponding to 105 days in orbit around Europa). **Figure 3–2** is the DDD depth curve for the JEO 2008 reference mission. JEO would accumulate a displacement damage dose of 1×10^{11} MeV/g (Si) behind a 100-mil-Al shell by the end of Europa Campaign 3. The dose estimate for the Europa orbit includes the self-shielding effect by the moon itself [Paranicas *et al.* 2007]. Note that a 1-cm tantalum (or WCu) shield is approximately equivalent to a 3-inch aluminum shield.

To evaluate the transient radiation effects on sensors, the flux energy spectra are needed. The JEO 2008 mission concept includes 4 Io fly-bys prior to the Europa Orbit Insertion (EOI). This is to increase both Io science and delivered mass. Thus, the mission peak flux occurs during the Io fly-bys. **Figure 3–3** shows the electron and proton fluxes at 5R_J (latitude 0). Also included in the figure are the energy spectra of electrons and protons at 9R_J (latitude 0), which can be used for estimating the radiation-induced transient effect while at the Europa orbits. The flux data presented here do not include the self-shielding effect of the moons.

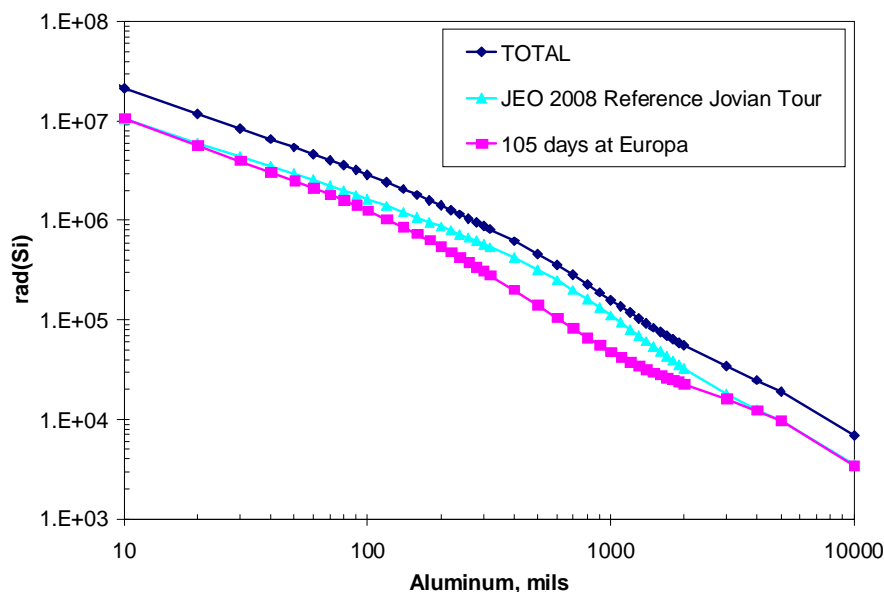


Figure 3–1. JEO Reference Total Ionizing Dose-Depth Curve. (No radiation design factor (RDF) included)

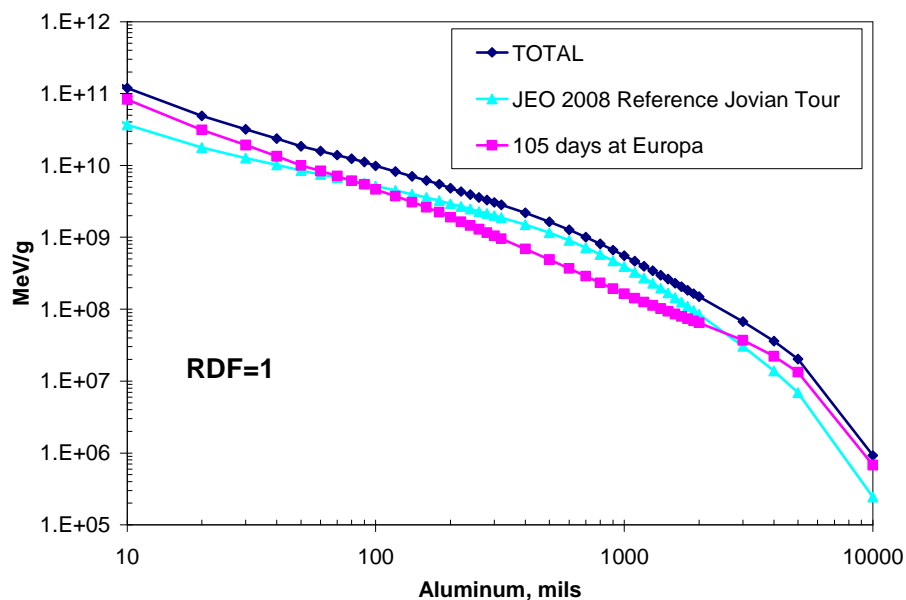


Figure 3–2. JEO reference displacement damage dose-depth curve. (No radiation design factor (RDF) included.)

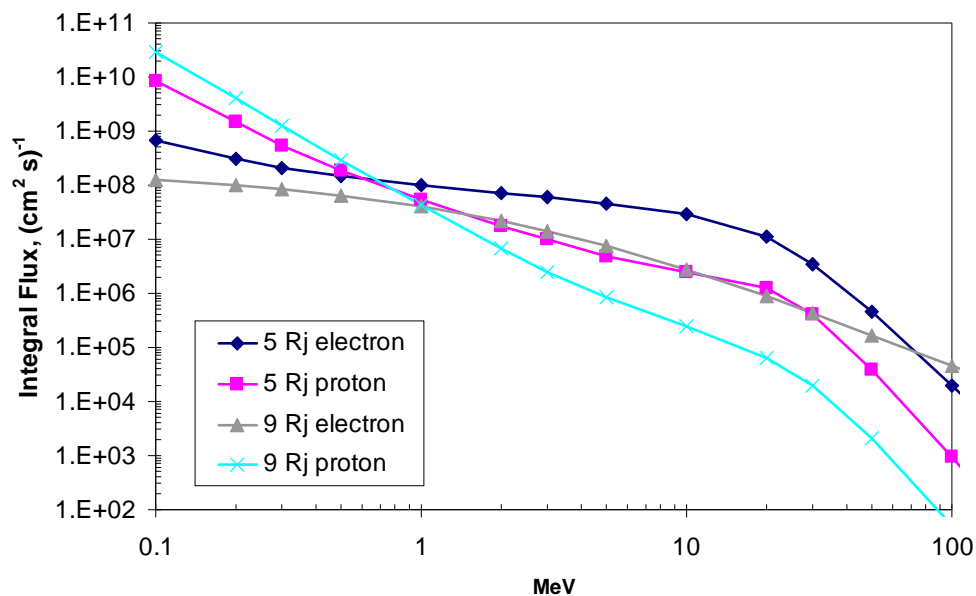


Figure 3–3. Integral spectra of electron and proton fluxes at 5 Rj (Io) and 9 Rj (Europa) with RDF=1

4 Radiation Environment behind the Nominal Shield

4.1 First Order Model

Given the intensity of the external environment described in §3, significant shielding is required for survivability in terms total dose (TID and DDD), as well to suppress radiation-induced transient noise effects from SEEs.

The total dose accumulation at the end of the primary Europa campaign (105 days in orbit) for a component behind several different thicknesses of Ta shielding is shown in [Table 4–1](#). These TID and DDD calculations are based on dose-depth curves discussed in §3, taking into account the density differences between Al and Ta. Because the various detector technologies are assessed against these TID and DDD levels, the required factor-of-2 radiation design guideline is applied.

The rate of SEEs dominates the concerns for detector performance during periods of high particle flux. Peak flux for JEO would occur during Io fly-bys at 5 R_J, but primary science requirements are driven by the flux seen during Europa orbit at 9 R_J. This report examines both of these high-flux periods for impact on sensor performance.

The particles hitting the detectors will both primary particles, albeit with degraded energy, and secondary particles that are a result of an interaction of primary particles with the instrument shielding mass. For the

Table 4–1. *Total JEO end-of-mission ionizing and displacement damage dose behind various shield thicknesses considered in this report.*

Ta Shield Thickness (cm)	Mission TID krad (Si) RDF=2	Mission DDD MeV/g (Si) RDF=2
0.3	400	1.3×10^9
0.6	140	3.6×10^8
1.0	70	1.3×10^8
2.0	32	2.2×10^7
3.0	20	1.9×10^6

purposes of this study, the incident protons and electrons are estimated as described below. A comprehensive Monte Carlo based modeling of the particles incident on the detectors is currently underway (see §4.3, §4.4) and will allow for refinement of the assessments in this report at a later date.

To minimize confusion, the following terminology is used throughout this report:

- The external environment is defined as the environment outside the shielding.
- An external particle is a particle from the external environment.
- The incident environment is the environment at the detector behind the shield.
- An incident particle is a particle that has penetrated the shield and is striking the detector
- A signal electron is an electron created by the passage of a incident particle (electron, proton, photon) through the detector pixel volume

The incident electron and proton flux behind a given shield thickness is approximated for this study using the integral flux of external particles at the minimum energy required to penetrate the shield. For example, for a 1-cm-thick Ta shield, the integral proton flux at 100 MeV is selected because that is approximately the proton energy required to penetrate a 1-cm-thick Ta shield and deposit energy in the sensitive volume of the detector. (Note: The integral flux of 100 MeV protons is the sum of all protons with energies ≥ 100 MeV.) The 30 MeV integral electron flux is selected for the same reason. The proton and electron flux incident on a detector for Ta shield thicknesses of 1.0 cm at both 5 R_J and 9 R_J are summarized in [Table 4–2](#) below. Tables for 0.3-cm and 1.0-cm Ta shield thicknesses may be found in Appendix A.

Table 4–2. Expected electron and proton flux incident on detectors behind a 1-cm Ta shield during Europa science (9 Rj) and Io flybys (5 Rj)

	Electrons	Protons
Incident Flux at 5 Rj	$3.5 \times 10^6 \text{ e/cm}^2\cdot\text{s}$	$9.2 \times 10^2 \text{ p/cm}^2\cdot\text{s}$
Incident Flux at 9 Rj	$4.3 \times 10^5 \text{ e/cm}^2\cdot\text{s}$	$50 \text{ p/cm}^2\cdot\text{s}$
Signal Electrons per “hit” for Si	~1,600	~10,000
Signal Electrons per “hit” for HgCdTe	~12,000	~60,000

Note 1: Estimates incident electron flux based on Integral Flux of 30 MeV external electrons. This external energy is the minimum required to penetrate 1-cm Ta.

Note 2: Estimates incident proton flux based on Integral Flux of 100 MeV external protons. This is the minimum energy required to penetrate 1-cm Ta.

Note 3: Estimates signal generation for electron “hits” based on 10 MeV average energy for incident electron

Note 4: Estimates signal generation for proton “hits” based on 100 MeV average energy for incident proton

Note 5: Assumes charge collection thickness of 10 μm with an additional geometrical factor of 1.7 (longest pathlength in a 10 μm cube). An additional factor of 1.5 is assumed to account for variations in pathlength and variations in diffusion charge collection.

4.2 Detector Response to Single Event Effects

The magnitude and distribution of SEE events within a detector array is a complicated problem and requires significant analysis including a modeling and experimental validation. The ongoing modeling effort is described in §4.3 and §4.4, as well as recommendations for future work. For this study, there is enough empirical information to get a worst-case estimate of events in various geometries and volumes from the electron and proton incident on the detector.

The size or amount of signal electrons generated by a passing proton depends on proton energy, path length, target density and charge collection efficiency. This empirical model will take the worst-case approach and assume 100% charge collection efficiency. The empirical model is explained below for the case of a 1-cm-thick Ta shield.

A 100 MeV proton incident on a silicon detector deposits about 1.4 KeV/ μm as it passes through the active region of the detector. The charge generated by this proton “hit” produces signal electrons that are not

easily distinguished from the science signal electrons. Given a typical path length of 10 μm and 3.6 eV required for each electron-hole pair produced in Si, the amount of charge generated by a 100 MeV proton “hit” is about 4,000 signal electrons. In the case of a CCD these electrons are stored in a well. Allowing for a geometric factor of 1.7 (the longest path length in a 10 μm cube) and an additional factor of 1.5 to account for variations in charge collection, path lengths, and proton energies, it is estimated that ~10,000 signal electrons are detected by the CCD as a result of the passage of a proton incident on the detector behind a 1-cm-thick Ta shield.

HgCdTe is more dense than Si and therefore the Linear Energy Transfer (LET) is higher (factor of ~2). The band gap in HgCdTe is about factor of three lower than for Si. Therefore the amount of signal electrons collected for HgCdTe is about a factor of 6 greater than that for Si. Thus, it is estimated that ~60,000 signal electrons are produced in a HgCdTe-based detector as a result of the passage of a proton incident on the detector

behind a 1-cm-thick shield. End of range protons or stopping protons are rare events and will deposit significantly more energy in a small sensitive volume.

The physics of electron transport through 1-cm of Ta shielding is also a complex problem and is part of the ongoing modeling effort discussed later. The empirical model used for this study assumes the average energy for an electron incident on a Si detector to be 10 MeV and an electron with this energy will deposit about 0.4 KeV/ μm as it passes through the detector. Using the same nominal detector assumptions discussed above for a proton “hit”, an electron “hit” will yield ~1,600 signal electrons. This agrees well with other reports of 1000–2000 signal electrons per incident electron [Becker *et al.* 2005, Liebe 2001]. Measurements with a decay source also confirms this estimate yielding 1500 signal electrons per incident electron [Klaasen *et al.* 1984]. Finally, this range is consistent with all Juno testing of detectors with the nominal depth assumptions used here.

Table 4–2 summarizes the signal electrons per proton “hit” and per electron “hit” for a 1.0-cm Ta shield. Tables for additional shield thicknesses (0.3 cm, 0.6 cm, 3.0 cm) and the assumptions required for each may be found in Appendix A.

4.3 Ongoing Modeling Effort

Various tools are available to transport external radiation environment into a secondary radiation environments behind various spacecraft structures. Three representative codes that can be used to model radiation transport through shielding material

are NOVICE, MCNPX and GEANT4, among others. We choose to implement the model in GEANT4 for several reasons. First, GEANT4 is sufficient to generate the geometry and track the radiation interactions required for small sensitive volumes. We have some understanding of the state of the physics within the code and have heritage from previous usage. Finally, this approach doesn’t require large resources in terms of labor and computer time.

The model was setup to estimate worst-case noise rates, TID as well as DDD in various notional detectors. The majority of the notional detectors are pixilated detectors with sensitive volume dimensions on the order of 10 μm . This approach included a number of shielding configurations shown in **Table 4–3**. The shielding materials investigated are tantalum, aluminum and a tungsten copper alloy. The tungsten copper alloy studied is roughly 80% tungsten and 20% copper with a density of 15.8 g/cm³. Limiting some of the geometrical configurations greatly streamlined the code development. The shielding slabs shown in **Figure 4–1** are semi-infinite. The alumina backing and copper board layer are in place to account for backscatter. The alumina layer is 0.254 cm and the copper board layer is 0.3175 cm.

Several hundred mono-energetic GEANT4 runs have been carried out for the matrix of shielding variations shown in **Table 4–3**. The GEANT4 outputs have been scaled to mission fluence predictions to support TID and DDD estimates. The outputs have also been normalized to peak flux rates to support SEE rate and magnitude estimates.

Table 4–3. A matrix of three shielding material and three thicknesses being investigated in the ongoing Monte Carlo modeling effort. The data in the table shows the thicknesses for the various areal shielding.

Areal Shielding g/cm ²	Ta		Al		W-Cu	
	16.7	g/cm ²	2.7	g/cm ²	15.8	g/cm ²
1.6	0.096	cm	0.593	cm	0.101	cm
8	0.479	cm	2.963	cm	0.506	cm
16	0.958	cm	5.926	cm	1.013	cm

Currently we are examining the results to validate the approach.

4.4 Future Effort

The recommendations for future effort fall into two categories of modeling and experiment. A more comprehensive 3-dimensional model than the current ongoing work is needed to better define the secondary environment behind various spacecraft shielding materials. For example DDD is higher for high Z shields such as tantalum as compared to aluminum shields of the same areal shielding [Dale et al. 1993].

Experimental measurements to confirm the relative contribution of DDD from electrons and protons is very important. The DDD dose from electrons is negligible for most missions but given the hard electron spectrum for a Jovian mission this can not be neglected. Radiation induced noise rates and magnitudes from electrons also need to be collected at various energies. Electrons lose energy via collisions and bremsstrahlung. At high electron energies the bremsstrahlung mechanism dominates and at low energies the collision mechanism dominates. The energy dependency is a strong function of the target and shield material. Therefore any model used to predict SET rates and distributions will need some experimental validation.

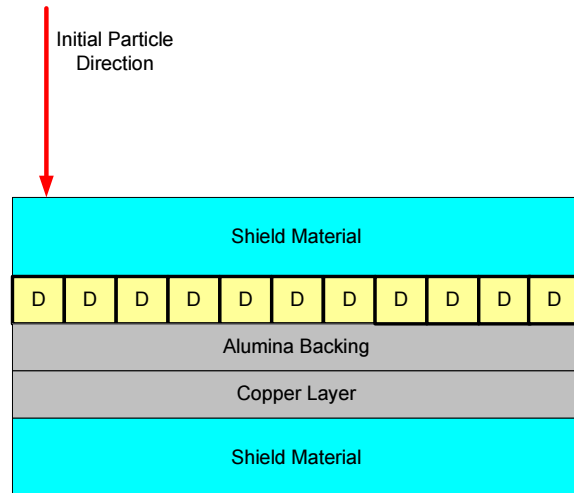


Figure 4–1. Above is a schematic of GEANT4 geometric model. The detector, alumina and the copper layers are enlarged for clarity.

5 Visible Detector Technology

The Charge-Coupled Device (CCD) and the Active Pixel Sensor (APS) or CMOS imager are considered the key visible imaging technologies for space applications. Both of these approaches are fabricated using high quality single crystal silicon material. Of the two, the CCD has dominated due to its low noise and technical maturity. In the late 1980's the CMOS imager concept was introduced largely for commercial applications. Recently the CMOS imager technology has undergone significant development in an effort to improve its performance characteristics and achieve the same levels of performance as scientific grade CCDs.

A summary of the performance of CCDs and CMOS visible imagers is presented in **Table 5-1** [Janesick and Putnam 2003]. Key differences for the CCD include lower dark

current and higher quantum efficiency and dynamic range. The method of charge readout is also a distinguishing characteristic between the two technologies. CCDs depend on a noiseless charge transfer as measured by charge transfer efficiency (CTE) while CMOS utilizes a direct X-Y addressing scheme. In radiation environments a critical issue for CCDs is the degradation of the charge transfer efficiency. In the following Sections each technology will briefly be described along with their performance under radiation environments.

5.1 Charge Coupled Devices (CCDs)

Typically CCDs are comprised of an array of Metal-Oxide-Semiconductor capacitors, typically built on a p-type silicon epitaxial layer on the order of 10 to 20 μm thick. Potential wells are created by the

Table 5-1. Performance of CMOS and CCD pixels. Acronyms are: PD – photodiode, PPD – pinned photodiode, PG – photogate, CS – charge share. [From Janesick and Putnam 2003]

Parameter	PD pixel	PPD pixel	PG pixel	CS pixel	CCD
pixel pitch, μm	8	8	8	8	8
dark current, pA/cm^2 (300 K)	200–2000	50–500	200–2000	200–2000	3–50 MPP
dark current FPN, % rms	10–30	10–30	10–30	10–30	10–30
sensitivity, V/e^-	15	25	25	15	5
read noise, e-rms (progressive scan)	60 rolling shutter	5	70	150	2
charge capacity, e^- (hard reset)	100,000	50,000	75,000	100,000	80,000
dynamic range	1667	10000	1070	666	40,000
fill factor, %	75	65	65	65	100
interacting QE, % (400 nm)	35	35	4	35	90
pixel FPN, % rms	1	1	1	1	2
MTF, % (900 nm) (Nyquist)	10–25	10–25	10–25	10–25	50
nonlinearity, % (full well)	7	7	7	7	1

application of a bias to one of the gate electrodes. The conversion of visible photons to signal carriers occurs in the silicon and is collected under a gate or more recently a photodiode. Converted signal charge is moved from one pixel to the next by switching the applied voltage from one electrode to the next, first vertically then horizontally to the readout amplifier. Three or four clock phases per pixel are typically used for vertical transfers. The charge transfer process is essentially lossless and the amplifier noise is small. The transfer typically occurs in a n-type buried channel that is $\sim 1 \mu\text{m}$ away from the surface, thus avoiding any noise generated by the Si/SiO₂ interface. The quality of these transfers is measured by the Charge Transfer Efficiency (CTE) which for high quality devices can be as high as 99.99995%.

This charge transfer process makes CCDs especially susceptible to displacement damage introduced into the silicon by energetic particles. Electronic traps are created in the silicon and degrade the signal charge packets as they move from pixel to pixel or gate-to-gate. Degradation of the CTE has been observed and will be discussed in the following paragraphs along with other effects due to operation in a radiation environment. Recently CCDs have been fabricated in n-type silicon which results in charge transfers in a p-channel. A noticeable improvement in CTE has been observed.

5.1.1 Total Dose and Displacement Damage Survivability

Total Ionizing Dose (TID)

Ionizing radiation creates traps at the silicon dioxide/ silicon interface and produces oxide charging in the pixel gate oxide and in the source-follower output amplifier. Modern CCDs use a buried channel to avoid degradation due to the interface traps. In addition many current CCDs use an architecture called multipinned phase (MPP)

to further reduce effects due to the surface. MPP technology causes surface inversion which fills surface traps and results in dark currents at very low levels ($< 10 \text{ pA/cm}^2$ at 300 K). This technology has led to a significant hardening against TID since surface dark current generation is no longer significant (assuming the surface remains inverted). Flatband voltage shifts due to standard thick oxide charging are also observed with typical flatband shifts $< 0.1 \text{ V/krad (Si)}$ for biased irradiations. The radiation tolerance of these devices can be improved by using adjustable bias voltages. The same is true for the output amplifier.

More recently, inverted mode devices from e2v, CCD55-20 and CCD57-10 and one MPP device from Atmel, TH7890M were irradiated with ^{60}Co up to $\sim 18 \text{ krad(Si)}$. [Hopkinson 2003]. The operating voltages were optimized after irradiation. The shift in flatband voltage was 0.14 to 0.15 V/krad (Si) for biased devices, which is slightly higher than previously measured. Since the CCD55 and the TH7890M were operated in an inverted mode, the surface dark current at 18 krad was almost completely suppressed and the dark current due to total ionizing dose was negligible. No significant changes in full well capacity, responsivity or response nonuniformity were observed.

The frame transfer n-channel CCDs, TH7890M and TH7891M were also studied by F. Julien and J. Vaillant [Julien 2001]. These devices have formats of 512 x 512 and 1024 x 1024, respectively. Mean dark before irradiation was $\sim 5 \text{ pA/cm}^2$. After 80 krad(Si) the dark current rose to 920 pA/cm^2 and after 100 krad(Si) rose to $3,700 \text{ pA/cm}^2$ at 20° C. The devices used the MPP architecture which demonstrated improved hardness as compared to a non-MPP device that exhibited a dark current increase of $3,000 \text{ pA/cm}^2$ after only 6 krad(Si) irradiation.

Significant improvements in TID hardness were observed for the MPP TH7890M and the TH7891M n-channel CCDs. However, the absolute dark currents increased ~ 180 times at 80 krad. Successful operation of these devices will require operation at reduced temperatures. Since dark current is an exponential function of temperature this is feasible as will be discussed later.

In general, operation in inversion can significantly reduce the surface ionization induced dark current resulting from Total Ionizing Dose environments. All visible imagers are subject to ionizing radiation effects but with proper techniques can be hardened. However, all these devices are also susceptible to displacement damage effects, which are difficult to mitigate. The main source of radiation induced dark current observed in MPP CCDs is a consequence of energetic particle induced displacement damage. Displacement damage also results in the degradation of the Charge Transfer Efficiency of CCDs.

Displacement Damage Dose (D_d or DDD)

Dark Current

Radiation-induced increases in dark current can have a significant effect on the performance of image sensors through an increase in dark current shot noise, loss of dynamic range, fixed pattern noise and the effects of dark current spikes. Dark current created by displacement damage originates from bulk defects or traps in the silicon material due to the thermal generation of carriers in the depletion region. Dark current has been extensively studied over the past 30 years.

Seven years ago J.R. Srour developed a concept based on a universal damage factor for radiation induced dark current in silicon [Srour 2000]. This concept addressed the mean dark or leakage current produced by radiation

induced carrier generation centers (defects) in the depletion region of the bulk material. These centers dominate as a source of dark current in many silicon devices. The theory places emphasis on effects that occur at or near room temperature for a sufficient time such as one week after irradiation.

After review of over thirty years of data, Srour derived a universal damage constant (K_{dark}) which is the increase in thermal generation rate per unit deposited displacement damage dose. The mean and standard deviation for K_{dark} (except for low-energy electrons and ^{60}Co photons) are $(1.9 \pm 0.6) \times 10^5$ carriers/cm³ sec per MeV/g. This damage factor applies to a wide variety of silicon based devices including both n and p-channel CCDs, CIDs, bipolar transistors, JFETS and MOS capacitors.

The dark current density can then be determined using

$$\Delta J_d = qW D_d K_{\text{dark}}$$

where D_d is the displacement dose deposited into a specific device that has a depletion width of W . q is the elemental charge. Determining D_d for the irradiation with penetrating monoenergetic particles only requires the fluence times the NIEL value. Obtaining D_d for an energy spectrum is more involved [Messinger *et al.* 1999]. The above equation is then used with the universal damage constant and the depletion width to find the dark current density. The displacement dose (D_d) value for Europa for instruments with a 1 cm Ta shield was found to be approximately 1.3×10^8 MeV/g (RDF = 2). The increase in mean dark current density at 300K is then calculated to be ~ 1,600 pA/cm² for a silicon device with a 4 micron depletion region. Typically this value, depending on the experiment, is then adjusted for both temperature and time since irradiation.

Table 5–1 lists the dark currents measured in a clear environment for scientific grade MPP CCDs which ranges from 3 to 50

pA/cm² and the CMOS PPD imager which ranges from 50 to 500 pA/cm².

Approximate agreement between the universal damage constant theory and practice was found by measuring a 512 x 512 TH7895M n-channel CCD manufactured by Thomson-CSF [Hopkinson 1996]. Surface dark current was suppressed by surface inversion. This device received a fluence of 10 MeV protons up to $\sim 8 \times 10^8$ protons/cm². The calculated D_d was 6.2×10^7 which is a factor of 2 lower than the value calculated for Europa with an RDF = 2. The measured mean dark current density was ~ 240 pA/cm² at 20°C. The calculated value using the universal damage constant at 20°C was ~ 400 pA/cm². This value was not corrected for time after irradiation.

P-channel versions of the standard e2v 3 phase CCD02 (non MPP devices) were characterized under proton bombardment [Hopkinson 1999]. One device was operated in the partially inverted mode. After $\sim 1.8 \times 10^{10}$ irradiation of 10 MeV protons ($D_d = 1.4 \times 10^8$ MeV/g) the device exhibited a dark current density increase of ~ 4000 pA/cm² at 25 C.

Hopkinson [Hopkinson 2003] irradiated three devices with 10 and 60 MeV protons. Two devices from e2v were characterized, an inverted mode CCD55-20 and an anti blooming devices, CCD57-10 and one MPP device from Atmel, TH7890M. The dark currents at ~ 300 K measured from these devices were consistent with the universal damage constant proposed by Srour.

Irradiations of the Atmel TH7890M MPP devices by to a D_d of $\sim 4.3 \times 10^7$ MeV/g using 2-, 10- and 50 MeV electrons resulted in an average increase in dark current of 56 pA/cm² at 20° C [Becker et al. 2006]. Since the device uses a multiphase pinned architecture (MPP), surface dark current was suppressed. The NIEL ratios for 50-MeV/10 MeV electrons of 1 ± 0.2 and 1.5 ± 0.3 compared well with a prior report of 1.42 [Summers et al. 1993]. The NIEL ratio for 50-MeV/2 MeV electrons

was found to be 1.7 as compared to the previous work's NIEL ratio of 2.95.

Recently the Jet Propulsion Laboratory tested a Semiconductor Technology Associates p-channel CCD design was fabricated by DALSA . [Becker and Elliot 2006]. The devices utilized the MPP architecture, had an approximate depletion depth of 10 μ m and a collection depth of 680 μ m. The samples were irradiated with 63 MeV protons ($D_d \sim 5 \times 10^7$ MeV/g) with leads shorted and unbiased at ambient temperature. The STA0120 device exhibited a post radiation dark current of 1,000 pA/cm² at ~ 30 °C and dropped to < 1.0 pA/cm² at -40 °C. Dark current distributions were also observed with the STA0120 sample producing a mean dark current of 422 electrons/pixel/sec with a one sigma value of 826 at 0 °C for this 21 μ m pixel device.

Although the discussion above centered about 300K, typical high performance CCDs are operated at reduced temperatures to further suppress the dark current. Numerous workers have measured the temperature dependence of bulk thermally generated dark current for devices operating both in clear and radiation environments. Plotting dark current as a function of inverse temperature yields an activation energy of ~ 0.63 eV [Marshall et al. 2005, Hopkinson 1996]. In general both the increase in dark current density and the universal dark current constant are proportional to the inverse temperature:

$$\Delta J_d, K_{\text{dark}} \propto \exp(-0.63 \text{ eV}/kT)$$

Becker [Becker et al. 2006] found this relationship to hold for the Atmel TH7890M MPP CCDs for temperatures from -40 C to room temperature while deriving an activation energy of ~ 0.27 eV in the -60 to -85 °C range. Dark currents were found to drop over 4 orders of magnitude in going from room temperature to -85 °C consistent with the exponential dependence of dark current on inverse temperature. These experiments also observed significant short term annealing effects after irradiation with 2 MeV electrons during a post-

irradiation hold at -85°C . Additional annealing was achieved by warming the CCD above -85°C .

P-channel CCDs from LBNL were characterized after irradiation with 12 MeV protons as a function of dose in the range of $1 - 10 \times 10^{10}$ protons/cm². The devices were irradiated unpowered and at room temperature. These devices were not backside processed, were fabricated on 600 μm high resistivity wafers and could not be fully depleted. At D_d of $\sim 6.7 \times 10^7$ MeV/g (Europa is a factor of 2 higher), the dark current measured was ~ 1 electron per hour at 128 K or -145°C [Bebek *et al.* 2002]. The author concluded the dark current of less than 4 electrons per exposure has little impact on the CCD performance. The device had a read noise of 2 electrons.

LBNL's new p-channel CCDs, fabricated at Dalsa Semiconductor, were compared to more conventional n-channel CCDs from e2v. Both notched and regular channel devices were examined. The devices were fabricated in high resistivity silicon and were 600 μm thick. A detector bias of 50 V was applied resulting in a depletion region of 300 μm . All measurements were performed using the Hubble Space Telescope's Wide Field Camera 3 (WFC3) timing. Dark current histograms were measured after exposures to 2.5×10^9 and 5.69×10^{10} cm⁻² 63 MeV protons. The average dark current was not reported. The data produced at -83°C indicated that the p-channel CCD technology was evidently more susceptible as compared to n-channel CCDs with respect to the formation of hot pixels. [Marshall *et al.* 2004].

More recently Dawson [Dawson *et al.* 2008] reported the response of backside-illuminated p-channel CCDs to 12.5 and 55 MeV protons with no bias voltages present. The creation of hot pixels was studied under using a fluence of 2×10^{10} protons/cm². The fraction of hot pixels before anneal (2.0×10^{-5}) and the fraction of hot pixels after anneal (1.3×10^{-6}) were detected at a temperature of -133

$^{\circ}\text{C}$. The devices were designed for the SNAP satellite operating at L2. Pre-irradiation dark current was measured at 3 – 4 electrons/hour with an expected increase to 20 electrons/hour after a six-year mission.

As mentioned previously in the discussion related to the universal damage coefficient, the change in dark current density was directly proportional to the displacement damage dose and the depletion layer width. ($\Delta J_d = qW D_d K_{\text{dark}}$) Typical n-channel CCDs are reported to have depletion regions around 4 μm and use low resistivity p-type silicon material. The new p-channel CCDs are reporting depletion widths of $\sim 300 \mu\text{m}$ and utilize high resistivity n-type material. The theory would suggest the thicker p-channel devices would produce as much as 75 times the amount of dark current at 300 K as compared to n-channel devices. Further work in to resolve this concern would be particularly important, including the impact of high resistivity material on both the theory and the actual dark current. The previous two references to p-channel CCDs acquired dark current measurements at -145°C and -83°C respectively.

Charge Transfer Efficiency (CTE)

Displacement damage resulting from impinging energetic particles degrades the charge transfer efficiency (CTE) in CCDs. This results in a loss of signal charge. Literature also commonly uses the charge transfer inefficiency (CTI) when discussing radiation effects. $\text{CTI} = 1 - \text{CTE}$.

In the past n-channel CCDs were found to be very sensitive to displacement damage from energetic particles as a consequence of the formation of a phosphorous-vacancy complex (E-center) [Janesick *et al.* 1989, Waczynski 2001]. These 'induced material defects' trap signal charge as it is transferred through the pixel and subsequently release it at some time later. This process can seriously

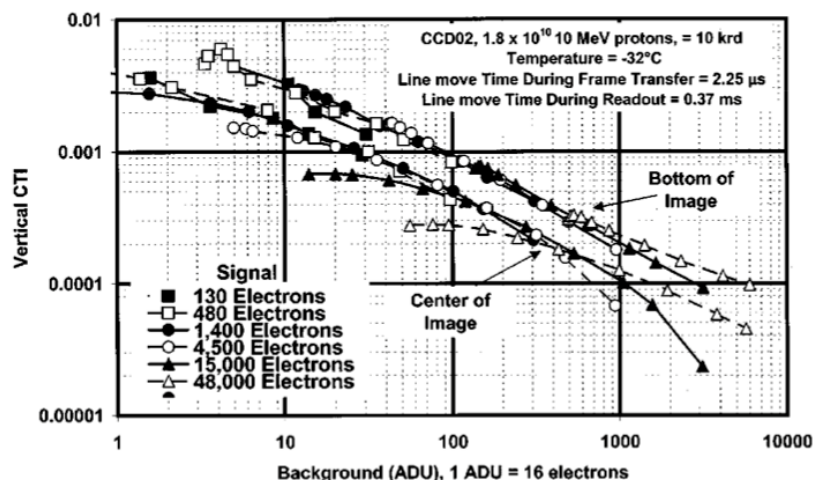


Figure 5-1. Example of CTI degradation produced by 1.8×10^{10} 10 MeV protons on an e2v CCD. [From Hopkinson 2000].

affect the transfer efficiency of CCDs operated near room temperature.

Recently p-channel CCDs were predicted to be more resistant to displacement damage than n-channel CCDs. The dominant hole trap created by energetic particles should be a divacancy hole trap formed by a second order process. Consequently there should be fewer divacancies than E-centers formed for a given NIEL, leading to improved hardness at any temperature for p-channel devices.

The total signal loss was found not to be a simple function of the amount of charge in the signal packet and the number of transfers it experiences. The CTI was found to be dependent on the history of the charge packets previously transferred through a given pixel and is extremely sensitive to damage caused by particle radiation. CTI also depends on signal and background charge levels, temperature and clock rate. CTI is found to increase with deposited displacement damage dose (D_d). **Figure 5-1** shows an example of the measured vertical CTI for an e2v CCD02 as a function of background [Hopkinson 2000]. The proton fluence and energy translates into a D_d equal to 1.4×10^8 MeV/g which is approximately the value calculated for the secondary environment behind the shield for Europa. At a low signal level and a

background of 1600 electrons the CTI degraded to .001 or a CTE of .999 at -32°C . After the worst case of 512 vertical transfers this CTE would degrade the signal to $\sim 60\%$ of its original value. The signal would then still have to undergo the horizontal transfer. When the well is \sim half full with signal electrons the CTI improves to $\sim .0003$ and signal degradation becomes 86% of the original value for 512 transfers.

The dominant defect controlling CTI was found to have an energy level of 0.44 eV [Hopkinson 2001]. At low temperature this level can be permanently filled which results in a significantly improved charge transfer efficiency.

Another example of n-channel CTI is shown in **Figure 5-2** where CTI is plotted as a function of signal charge with temperature as a parameter. An Atmel TH7890M CCD was tested. This device endured a displacement damage dose of 1.33×10^8 which is approximately that anticipated for Europa [Hopkinson 2003]. Reducing the temperature and/or increasing the signal levels and/or the background levels dramatically improved the charge transfer efficiency.

Figure 5-3 depicts the results of testing a n – channel Tekronix TK512 CCD 512 x 512 backside illuminated device [Hardy et al. 1998]. The chart plots the CTI as a function of signal packet size in electrons. Two curves were generated as a result of two 3 MeV proton irradiations. The first was at a fluence of 6×10^9 p/cm² ($D_d \sim 1.4 \times 10^8$ MeV/g) and the second at a fluence of 1.5×10^9 p/cm² ($D_d \sim 3.6 \times 10^7$ MeV/g). The D_d values bracket the calculated Europa. For a 1,000 electron packet the lower fluence yields a CTI of $< .0002$ while the higher fluence produces a CTI of $\sim .0007$ at a temperature of 155K or -118°C . As

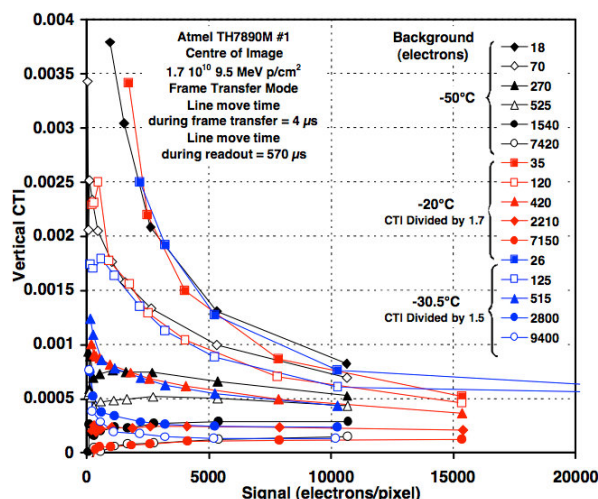


Figure 5-2. Charge transfer inefficiency resulting from the irradiation of a Atmel TH7890 CCD by 1.7×10^{10} 9.5 MeV protons/cm². [From Hopkinson 2003]

the signal size increases the CTI for both fluences becomes progressively better.

Recently p-channel CCDs have been developed at the Lawrence Berkeley National Laboratory (LBNL) using high resistivity n-type silicon [Bebek 2002]. Such devices are expected to offer more radiation tolerance. Standard n-channel CCDs are fabricated on low resistivity p-type silicon with typical

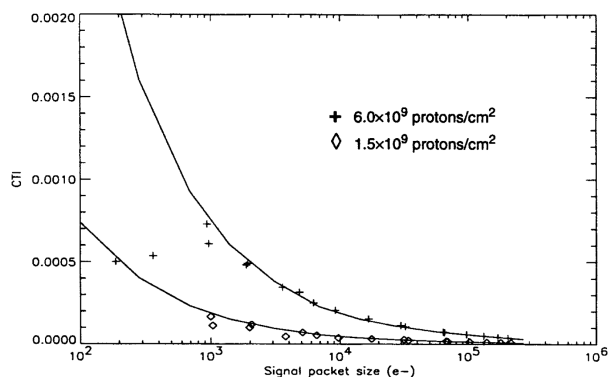


Figure 5-3. CTI in a n-channel CCD as a function of charge packet size at 155K or -118 °C. Symbols differentiate data from the low and high radiations sections of the device. The lines indicated calculated results with a trap level of 0.21 eV, a cross section of 5×10^{-16} cm² and a trap density of 5.2×10^{10} cm⁻³ (high) and 1.3×10^{10} cm⁻³ (low). [From Hardy et al. 1998].

depletion widths of several microns. The new p-channel CCDs are fabricated on high resistivity n-type silicon and allow the application of an external voltage to create a depletion zone of 300 μm or more. The thicker depletion region results in both improved red response and an improved blue response without thinning. Finally, since divacancy formation is considered less favorable, the p-channel devices are expected to have improved radiation hardness.

The devices tested were 600 μm thick and therefore could not be fully depleted. The devices were irradiated unpowered and at room temperature. **Figure 5-4** plots the measured CTE as a function of temperature for both the parallel and the serial transfers. The device was irradiated with 1×10^{11} 12 MeV protons/cm². The D_d was $\sim 7.4 \times 10^8$ MeV/g. The serial CTE shows inefficiency of the traps at higher temperature where the clock overlap time is longer than the detrapping time. In the low temperature region the serial CTE is high because the traps are mostly full and have a long decay time. The figure shows that there exists an optimum temperature for a given clock rate and CCD design.

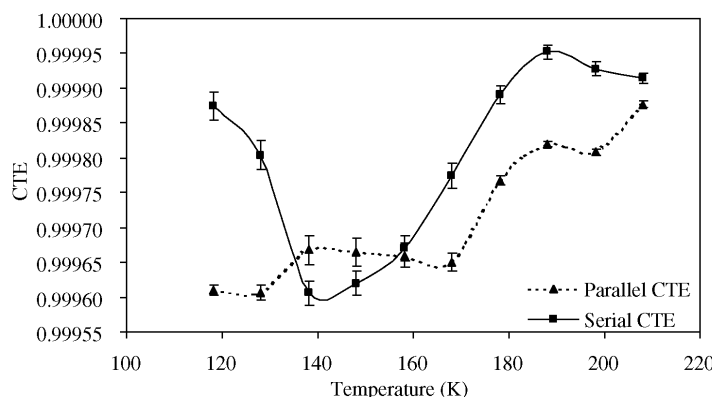


Figure 5-4. The CTE as a function of temperature for a LBNL p-channel CCD irradiated with 1×10^{11} protons/cm². [From Bebek et al. 2002]

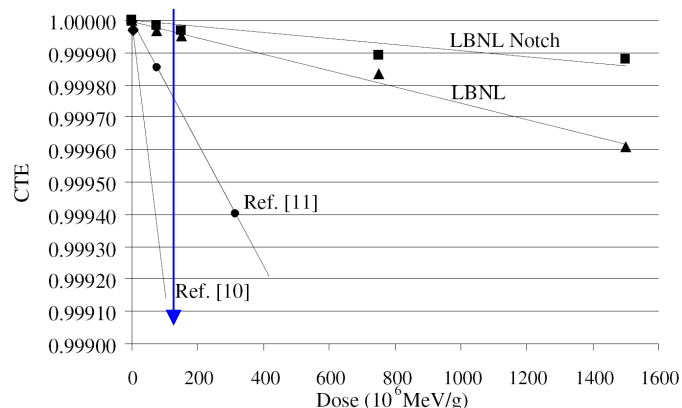


Figure 5–5. Measured CTE values from two p-channel CCDs from LBNL compared to two n-channel CCD values as a function of deposited displacement damage dose (D_d). Straight lines were added to assist in the comparisons. The blue line indicates the D_d of 1.3×10^8 MeV/g for Europa. [From Hardy et al. 1998]

Figure 5–5 compares the CTE degradation for the new p-channel CCDs and modern n-channel devices. Two sets of lines as a function of deposited displacement damage dose (D_d) are plotted for the LBNL p-channel devices both with and without a notch. These are compared n-channel devices from Hardy [Hardy et al. 1998]. The value calculated for Europa would appear at ~ 130 (for 1-cm Ta shielding) on the horizontal Dose axis. In this chart both n- and p-channel CCDs exhibit acceptable CTEs at this displacement damage Dose.

Figure 5–6 presents a comparison of the Charge Transfer Inefficiency (CTI) as a function of signal level at -83°C after exposure to $2.5 \times 10^9 \text{ cm}^2$ 63 MeV protons ($D_d \sim 8.3 \times 10^6$ MeV/g). LBNL's new p-channel CCDs, fabricated at Dalsa Semiconductor, are compared to more conventional n-channel CCDs from e2v. Both notched and regular channel devices were examined. The CTI degradation of the p-channel devices was almost an order of magnitude less severe than the n-channel devices. All measurements were performed using

the Hubble Space Telescope's Wide Field Camera 3 (WFC3) timing. CTI is expected to vary with temperature and the current tests were optimized for the n-channel CCD. Greater than 10x improvement was postulated in the paper at other temperatures [Marshall et al. 2004].

5.1.2 Transient Effects

Transient radiation effects occur when an energetic particle (electron or proton) traverses the active signal conversion volume of a detector such as a CCD. Energy is deposited by the particle via ionization and induces charge generation along its entire path through the device. Given the electron and proton energies that are expected to penetrate the shield, these particles will traverse the device volume and will deposit a limited amount of their total energy. In general the particles will not be at normal incidence to the detector and consequently may cross multiple pixels. Thinned detectors will have the greatest immunity to this effect. Transient effects are not permanent, and the spurious charge is swept out during readout but the additional charge constitutes a source of noise in the image.

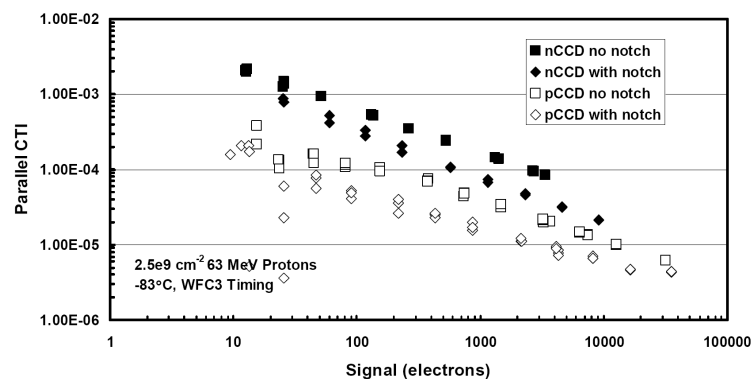


Figure 5–6. CTI comparisons at -83°C between n-channel and p-channel CCDs both with and without notches. The devices were exposed to $2.5 \times 10^9 \text{ cm}^2$ 63 MeV protons. CTI improvement using the p-channel CCD was somewhat dependant on signal but ranged from a factor of 5 to 10. [From Marshall et al. 2004]

The secondary environment behind the shield is expected to pass > 30 MeV electrons at a flux of $\sim 4.28 \times 10^5$ electrons/cm²/sec at 9 R_j and 3.5×10^6 e⁻/cm²/sec at 5 R_j. The shield will pass > 100 MeV protons with an \sim flux of 50 protons/cm²/sec at 9 R_j and 920 p/cm²/sec at 5 R_j. Previous work has shown that 10 MeV electrons can create a transient signal of ~ 900 electrons per incident particle [Becker *et al.* 2005]. For this example it is estimated that shield penetrating electrons produce 1000 to 2000 secondaries in the silicon pixel material. Protons are expected to deposit ~ 1.4 keV/ μ m for 100 MeV protons. Given a 10 micron depletion width and an electron-hole pair production energy of 3.6 eV/e-h the number of carrier pairs produced is expected to be $\sim 4,000$. Given the uncertainties in incident angle, carrier generation from 100 MeV protons could reach $\sim 10,000$. Less energetic protons could produce a higher numbers of carrier pairs, since the linear energy transfer (LET) increases with decreasing proton energies

Details of the chosen CCD device and its mode of operation will affect the impact of transient radiation behind the shield. Assuming a $15.2 \mu\text{m}$ pixel size similar to that of the Galileo CCD, an integration time of 40 ms and an electron fluence of 4.28×10^5 electrons/cm²/sec at 9 R_j there are 0.041 electron strikes produced per integration time per pixel. For a 1k x 1k array this means that on the average 4.1% of the pixels will be hit by an electron and subsequently produce $\sim 2,000$ false signal electrons. At 5 R_j there are 0.32 electron strikes per 40 ms integration time per pixel. On the average 32% of the pixels will be hit by an energetic electron per frame.

Klaasen, et al (1984) obtained empirical data on the details of particle interaction with a CCD. The test setup utilized strontium-90 which is a source of 2 MeV electrons. Signal and noise were generated solely by exposure to the ionizing strontium-90 radiation. A plot of random noise versus mean signal was

created. The linear portion of this curve was fitted by an equation of the form

$$n = J\sqrt{S},$$

where n = rms noise and S = mean radiation-induced signal per pixel, and J is a constant. S is equivalent to $M * P$, where M = the mean total charge produced per radiation interaction and P = the mean number of incident particles per pixel. J was found empirically to be equal to 35 from the plot of measured noise versus signal using the strontium 90 source.

For the environment under consideration at 9 R_j, $P = 0.042$ incident particles per pixel and $M = 2000$ electrons. The rms noise, n , is then found to be ~ 317 electrons. For 5 R_j, $P = .32$ and n , the total noise, is found to be 885 electrons. To arrive at a total system noise this number must be root mean squared with the photon and dark current shot noise.

The preceding is a simplified calculation and assumes normal incidence with a short track confined to one pixel with a thickness of less than $10 \mu\text{m}$. (This characterizes thin depletion layer n-channel devices but will become a concern for thick $200 \mu\text{m}$ silicon p-channel devices where the charge generation per incident energetic particle is expected to scale with the thickness of the material). Also in general, the particles may affect nearest neighbor pixels but should share the charge generated.

For CCDs with well capacities of $\sim 100,000$ electrons and reasonable signal, the additional false charge for thin devices will increase the detector noise. The transients may prohibit the detection of small signals as a consequence of possible increased integration times and lower absolute incident signal photons. Theoretically the transient hits produced by the incident electrons will be spatially random and could potentially be filtered out.

Protons will produce a much higher false signal per hit but are far fewer, 920 p/cm²/sec

at 5 R_j and 50 p/cm²/sec at 9 R_j. Assuming a pair-production of 10,000 carriers, these hits will be imaged as bright pixels and will most likely be unusable. In the worst case of 5 R_j, ~ 0.1 % of the pixels would be affected per frame. If signal processing is used, this large event could theoretically be discriminated and dropped.

5.1.3 Mitigation Techniques

A number of methods for improving the radiation tolerance of CCD were reported by Hopkinson [Hopkinson *et al.* 1996]. These include increasing shield thickness, choice of device architecture which include notched buried channels, reducing device internal electric fields to reduce dark current spikes, optimizing active region thicknesses to improve response to transient event, use of an inverted mode (MPP) device that produces a negligible ionization induced dark current, and reducing flatband voltage shifts by a suitable choice of oxide technology.

Dark current can be significantly reduced by cooling since it has an exponential dependence on inverse temperature. Cooling increases the emission times of particle induced traps which results in improved CTE. CTE of irradiated devices can be improved by optimum choice of clocking rate which affects, deferred charge, dark signal and transient hit rate (through the integration time).

Data processing software can be utilized to discriminate against transient events and permanent dark current spikes. Techniques include subframe data sampling, thresholding and dropping bad pixels and good pixel averaging.

Performance can be improved by periodic heating (annealing) to room temperature and perhaps to 100-150 °C to anneal out trap centers and improve CTE and reduce dark current.

Device hardening can be improved by material engineering such as the introduction of controlled levels of impurities such as

oxygen into the pure silicon to act as sinks for vacancies.

CTI was found to be a function of background charge. Use of increased background charge or 'fat zero' can also give a dramatic improvement in CTI by a factor as much as 10. Background or 'fat zero' will improve CTI at the expense of increased shot noise.

A notched or supplementary buried channel can be useful in small signal applications by confining the charge into a smaller volume.

5.1.4 Planetary Protection

JEO's baseline approaches for meeting planetary protection sterilization requirements include dry heat sterilization at 125 °C for 50 hours for qualification and 115 °C for 50 hours for acceptance testing, analysis proving that a sterilizing ionizing dose of 7 Mrad(Si) or unit assembly and test under sterile conditions through ATLO. Dry heat sterilization is viewed as the most practical approach, considering the logistical difficulty of assembly and test under sterile conditions, and the inability of most CCD devices to withstand an ionizing dose of 7 Mrad(Si).

Silicon CCD devices are fairly robust to the level of temperature cycling listed above and could be sterilized at these times and temperatures. However, they are likely to be packaged with adhesives, or optical coating processes that will not withstand JEO dry heat sterilization requirements. Typically ceramic packages are used which are temperature resistant. The packaging and coating processes will depend on particular applications and will need to be assessed. The imager chip will then likely be integrated with the system including coolers. The assembly and test procedures will need to be reviewed and modified.

5.1.5 Overall Assessment

Proper shielding is critical to the feasible operation of CCDs during the Europa Mission. As discussed in the secondary radiation environment section, 1 cm of Ta will reduce both the total ionizing dose and the displacement damage dose to fairly manageable levels for both n- and p-channel CCDs. The key parameters are the displacement damage dose (D_d) which creates dark current and reduces CTE. An exact determination can only be made after a detailed signal-to-noise calculation based on the imager and system design chosen and the mission science desired.

The exponential decrease of dark current with temperature permits the CCDs to operate with acceptable dark current by cooling to low temperature such as $< -85^\circ\text{C}$ or $< 188\text{K}$. Some of the data shown previously was taken at 128K. This same temperature decrease improves the CTE after irradiation. It is interesting to note that the CCD's superior initial dark current as compared to CMOS imagers rapidly degrades to CMOS levels of dark current when irradiated.

Degradation of CTE is seen to be a critical issue. Data was presented that showed that CTE depended on temperature, type of device (n- or p-channel), clocking rate, background and signal levels. P-channel devices were reported to exhibit a factor of ten improvement in CTE under similar displacement damage dose conditions and temperature ranges. A more detailed assessment (via a signal to noise calculation) of the suitability of either n- or p-channel CCD is required once the system definition occurs and science requirements are defined in detail.

A key concern relates to the transient radiation flux that will be present under the expected mission conditions. Energetic electrons and protons will impact the detectors and create electron-hole pairs that are collected by the device as false signals. The major

mitigation technique for transient radiation is a reduction in the volume of the signal-charge generating region. Detection volumes can be reduced by using small pixels with micro lenses. In addition, CCDs with reduced depletion areas are favored. Currently p-channel devices are being developed that utilize 200 μm depletion regions in order to enhance both the blue and red response of the new CCDs. This thick depletion region can become a detriment to high signal-to-noise operation when exposed to transient particles. Further testing and development are needed to reduce the p-channel CCD active silicon thicknesses to values of less than 20 μm , which would be comparable to the current n-channel devices.

5.2 CMOS Imagers or Active Pixel Sensors

Complementary Metal-Oxide-Semiconductor (CMOS) visible imaging technology is an important alternative to the CCD. This competitive technology is also based on single crystal silicon material and is also known as the Active Pixel Sensor (APD) since it contains active transistors in its unit cell. Recently, CMOS imagers have experienced impressive growth and have emerged as a viable imaging approach for many commercial, scientific, space and military applications. Unlike CCD technology, CMOS imagers use mainstream microelectronics fabrication processes. Three key advantages are: 1) CMOS imagers can be monolithically integrated with other CMOS digital and analog circuits including timing and control modules, analog signal processing circuits for noise suppression and analog-to-digital converters, 2) CMOS imagers are inherently low power, for example [*Eid et al. 2002*] at a video rate of 30 frames per second and a 1.5V power supply, the image sensor can consume as little as 550 μW and 3) CMOS imagers have an economic advantages since they take advantage of commercial foundries that routinely fabricate large volumes of

integrated circuits and the imagers are highly integrated thus reducing the total component count for a sensor. A large number of publications have addressed the comparisons of CCD and CMOS imagers. [Janesick 2001, Janesick 2004, Janesick et al. 2007, Janesick & Putnam 2003, Bigas et al. 2006, Janesick et al. 2006, Magnan 2003, Janesick et al. 2008, Bai 2008]. One of the major disadvantages of CMOS imagers in the past has been higher readnoise (typically $\sim 30 e^-$ for CMOS compared to $\sim 2 e^-$ for science grade CCDs) and lower quantum efficiency.

CMOS imagers have the ability to X-Y address specific areas of the array and can be designed with multiple windowing capability. Designs exist that can also readout these selectable windows at increased rates.

Each CMOS unit cell contains a photodiode for photon detection and 3 or more field effect transistors (FETs). The most common CMOS imager is a three-transistor (3T) unit cell device which contains a source follower per pixel amplifier, a reset FET and a row switch FET. CMOS imagers have the advantage that each pixel is directly addressed in order to readout the image so there are no energetic particle induced CTE losses such as those experienced with CCDs.

CMOS imagers are subject to increases in dark current and dark current nonuniformity, fixed pattern noise, and random telegraph noise as a result of proton exposure. There is also the potential for latch-up as a result of the on chip signal processing circuitry.

Recently Janesick [Janesick et al. 2008] reported a high performance CMOS imager that incorporates a five-transistor (5T) charge coupled pixel that exhibits a 2-electron noise floor. The 479 x 476 test device showed a 99.5% CTE for low signal levels of less than $20 e^-$ and can maintain the CTE to levels of 1 Mrad. This is a remarkable CMOS feature since CCD imagers stop working at considerably lower dose levels. While CCDs

require thousands of transfers and are hampered by radiation induced defects the new CMOS device involves only one transfer because the pixels are addressed directly. CMOS imager technology is insensitive to radiation induced deferred-charge CTE issues. The devices also used innovative signal processing techniques and pixel designs with high voltage-to-electron conversion efficiency.

Typical front side illuminated CMOS imagers possess quantum efficiencies at 500 nm of $\sim 35\%$ partially as a consequence of a 65% to 75% fill factor. New micro lens designs improve this figure to 60 to 70%. Recently backside illuminated CMOS imagers have demonstrated quantum efficiencies of $> 60\%$ at 500 nm for 6 μm thick silicon devices and $> 80\%$ for 21 μm thick devices [Janesick et al. 2007].

Recently Teledyne has reported frontside QE values with micro lens $> 80\%$ and similar values for backside illuminated devices [Bai et al. 2008]. This company has produced monolithic CMOS imagers up to $\sim 8\text{k} \times 8\text{k}$ designers with 3T pixels. They have reported monolithic CMOS imaging arrays with demonstrated 2.8 electrons readnoise and dark currents of less than 10 pA/cm^2 for frontside illuminated devices.

5.2.1 Total Dose and Displacement Damage Survivability

Total Ionizing Dose (TID) and Proton Bombardment

Ionizing radiation effects are typically attributed to buildup or trapping of positive charge (holes) with the oxide as well as the creation of interface state traps in the silicon/silicon dioxide interface. They also can be responsible for threshold voltage shifts that increase leakage currents in NMOS transistors and N-channel intertransistor leakage currents. Modern CMOS technology takes advantage of extremely thin gate oxides ($< 12 \text{ nm}$), consequently the effects of threshold shifts and

hole trapping are deemed small. The created interface traps have energy levels within the silicon bandgap and as a result contribute to the dark current through generation / recombination thermal processes.

Eid [Eid *et al.* 2001] have reviewed a number of previous publications related to the total dose testing of CMOS imagers. They presented a summary table reproduced here as **Table 5–2**. These are earlier references that report progress up to ~ 2001. None of the approaches described in the references below utilize new radiation hardness by design techniques. New radiation hardness by design techniques specify physical CMOS circuit layouts with enclosed geometry intertransistor isolation and P-channel guard rings combined with a standard deep submicrometer CMOS fabrication that utilizes thin gate oxides.

Eid [Eid *et al.* 2001] utilized the enclosed geometry and P-channel guard rings to design a set of four N-type radiation tolerant CMOS active photodiode pixels. These were compiled into a 256 x 256 array with four subarrays. The chip was fabricated using standard 0.35 μm CMOS fabrication process with 7 nm thick gate oxides. The devices were irradiated with Co^{60} at room temperature with the test chip biased and the pixels set to reset voltage to simulate actual operation. Dark current at ambient temperature as a function of total ionizing dose with pixel design as a parameter is plotted in **Figure 5–7**. Dark current at a total dose estimated for Europa behind the 1 cm Ta shield (70 krad(Si) with $\text{RDF} = 2$) ranged from ~ 200 to ~600 pA/cm^2 (at ambient temperature) with slopes ranging from 1.1 to 1.8 $\text{pA}/\text{cm}^2/\text{krad}(\text{Si})$. The dark

Table 5–2. Comparison of previous work on tolerance of CMOS APS image sensors to ionizing radiation. [From Eid *et al.* 2001].

Reference and Year	Array Size	Pixel Size	Fabrication Process	Maximum Total Dose (Si)	Dark Current at Maximum Total Dose	Comments
[21] 2000	512 X 512	25 μm X 25 μm	0.7 μm Standard	21 Krd	45 nA/cm^2	PD
[22], [25] 2000 and 1999	32 X 32	50 μm X 50 μm	1.2 μm Standard	10 Krd	1.5 nA/cm^2 25 nA/cm^2	PD PG
[28] 1997	32 X 32	26.4 μm X 26.4 μm	1.2 μm Standard	10 Krd	6 nA/cm^2	PD
[27] 2001	Not reported	12 μm X 12 μm	0.5 μm Standard	25 Krd ^a	Not reported ^b	220° K
[23], [24], [26] 2000 and 2001	512 X 512	25 μm X 25 μm	0.5 μm and 0.7 μm Standard ^c	3.4 Mrd 22.5 Mrd	1.25 V/s 0.8 V/s	PMOS PD NMOS PD ^{d,e}
[27] 2001	256 X 256	20 μm X 20 μm	0.5 μm Specialized	5.5 Mrd	60 nA/cm^2	PD ^f

- a) After 25 Krd (Si), the image sensor went through a catastrophic and permanent failure.
b) Dark current was reported to be large enough to saturate the pixels (no pixel rate or frame rate was reported).
c) Some test structures were fabricated in the 0.5- μm standard process, but the reported dark current data was for image sensors fabricated in the 0.7- μm standard process.
d) Irradiation of the NMOS PD pixel chip was stopped after 3.4 Mrd. The chip was left to anneal at room temperature for 562 hours before irradiation resumed.
e) Neither conversion gain nor PD capacitance was reported for the PMOS PD pixel. Based on the PD capacitance reported for the NMOS PD pixel (10 fF), its dark current is about 7 nA/cm^2 .
f) Pre-radiation dark current was 30 nA/cm^2 .

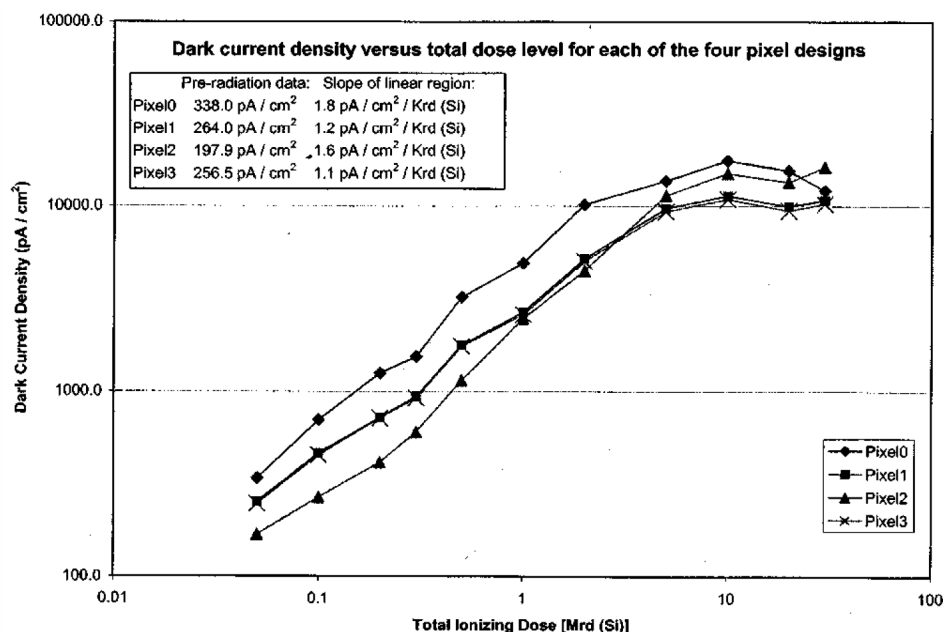


Figure 5-7. Dark current density as a function of total ionizing dose for each of the four pixel designs. [From Eid et al. 2001]

current slopes are considered very low values. The most pronounced affect on performance was an increase in dark current which was found to be linear with dose. Little annealing was observed when the devices were stored unbiased at room temperature for 2 months. Radiation hardness by design was found to be very effective.

Pain [Pain et al. 2004] has reported on the performance of CMOS devices hardened using a specialized radiation-hard foundry and different devices hardened by design. Devices fabricated using the BAE Manassas 0.5 μm CMOS fabrication line yielded hardened small imagers with threshold voltage shifts of < 10 mV after 1 Mrad of TID. The devices experienced ~ 0.4 pA/cm²/rad increase in dark current with TID for field-stop and surface junction pixel designs at room temperature. Different devices fabricated elsewhere used a deep submicron process with thin gate oxides (< 70 Å). These designs included CMOS pixels with guard-rings and edgeless FETs. These devices yielded dark current increases of 8-9 pA/cm²/krad.

The authors concluded that, although the radiation hardness of CMOS imagers is increased by using radiation-hardened foundries or radiation hardness by design approaches, neither approach is ideal for high performance imagers. Radiation hardness by design approaches suffer from poor fill factors, high field effects and result in poor MTF. Radiation hardness by foundry suffers from high cost, long turnaround times and reduced process stability and reproducibility. A more suitable approach is suggested that takes advantage of process changes already underway in cutting edge submicron CMOS fabrication methods in order to make them more compatible with CMOS imagers. Minor changes in one of more of these process steps can eliminate most of the disadvantages offered by radiation hardening by design. This approach would require the joint cooperation of researchers and the commercial foundry.

Recently the Jet Propulsion Laboratory (JPL) has characterized a large 12 megapixel CMOS imager from Teledyne with a 3T pixel which was not intentionally hardened [Wrigley 2006]. Exposures to both Co⁶⁰ and 51 MeV

Table 5–3: Dark Current Distribution Statistics versus Total Ionizing Dose. [From Hubbs *et al.* 2005]

Total Ionizing Dose (krad(Si))	Median Dark Current (Amperes)	Standard Deviation of Dark Current Distribution (Amperes)	Dark Current Distribution Non-Uniformity (σ /Mean) (%)
Pre-Radiation	6.4×10^{-13}	4.7×10^{-13}	7
100	9.7×10^{-14}	1.3×10^{-14}	13
750	2.4×10^{-12}	1.1×10^{-12}	44

protons occurred. Dark current increased from 230 electrons/sec at 10 °C to 3,500 electrons/sec after exposure to 8 krad. The devices had a pre irradiation readnoise of ~ 28 electrons. After irradiation the total noise (rss of readnoise and dark current noise) at an integration time of 3.73 ms, increased between 2% and 6% above the baseline noise value. Devices were bombarded to a fluence of 5×10^{10} protons/cm² and exhibited a total noise increase of only 1.1 to 3.1% at 10 °C. No change in quantum efficiency as a function of wavelength was observed. The displacement damage dose (D_d) at 51 MeV and a fluence of 5×10^{10} protons is ~ 1.9×10^8 MeV/g which exceeds the value calculated for Europa behind 1 cm Ta.

New CMOS imaging hybrids are now

also available up to 4k x 4k. Recently Hubbs [Hubbs *et al.* 2005] tested a small 128 x 128 P-i-N silicon CMOS hybrid with 60 μ m pixels under total dose and proton irradiation conditions. The increase in dark current after a TID dose of 750 krad(Si) was small at 233 K as seen in Table 5–3. The increase in median dark current as a function of 63 MeV proton fluence is shown in Figure 5–8. The responsivity of the devices is unchanged after either total dose or proton exposures.

Recently Cypress has released two high performance radiation hardened CMOS imagers called the STAR250 and its successor the STAR1000. A number of papers have characterized these devices in detail under radiation environments [Hopkinson 2002, Bogarets *et al.* 2003, Hopkinson 2004].

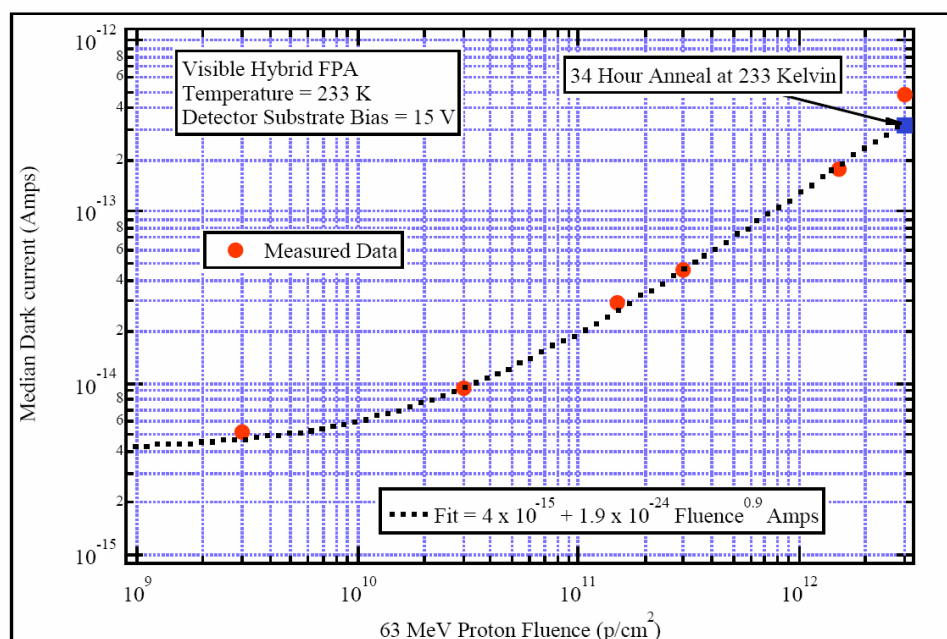


Figure 5–8. Median dark current as a function of 63 MeV proton fluence at $T = 233$ K for a P-i-N silicon CMOS hybrid imagers. [From Hubbs *et al.* 2005]

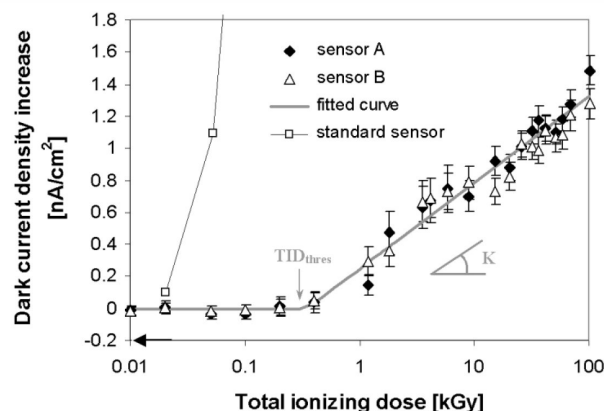


Figure 5-9. Measured dark current as a function of TID in kGy where 1 Gy = 100 rads. TID_{thres} is the ionizing threshold that is necessary to observe and increase in dark current. Data from the STAR250 is compared to a standard CMOS imager. $T = 27^\circ\text{C}$. [From Bogaerts et al. 2003]

The STAR250 sensors have a resolution of 512×512 with $25 \mu\text{m}$ pixels. The mean dark current of this CMOS imager before irradiation was $\sim 200 \text{ pA/cm}^2$ at 27°C with a read noise of $\sim 76 \text{ e}^-$. Figure 5-9 depicts the measured dark current as a function of total ionizing dose. The rate of linear dark current increase is $\sim 0.54 \text{ nA/cm}^2/\text{krad}$. A logarithmic decrease of dark current was observed with annealing time where the slope of the

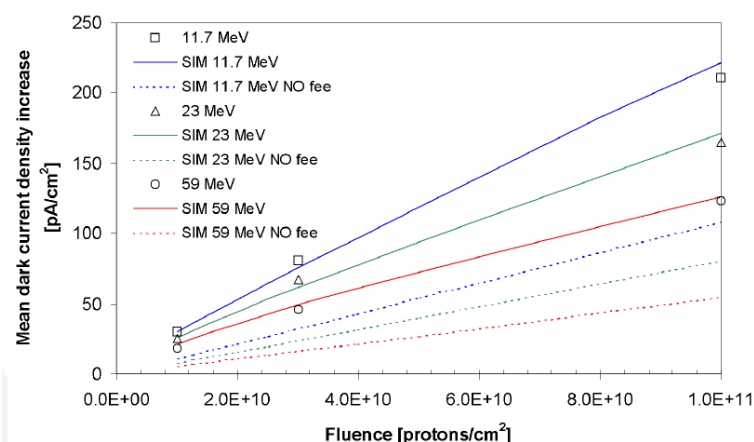


Figure 5-10. Mean dark current density increase measured on nine devices at 27°C along with simulated curves. The D_d for Europa behind a 1 cm Ta shield results in a mean dark current increase of $\sim 50 \text{ pA/cm}^2/\text{s}$. [From Bogaerts et al. 2003]

annealing rate varied from 0.069 to 0.175 nA/cm^2 per decade. The mean dark current density increases as a function of fluence with 11.7, 23 and 59 MeV protons as parameters are shown in Figure 5-10. The equivalent displacement damage dose that would be experienced by the Europa mission occurs at $\sim 4 \times 10^{10} \text{ p/cm}^2/\text{s}$ fluence for 59 MeV protons and would generate an increase of $\sim 60 \text{ pA/cm}^2$ at 27°C [Bogarets et al. 2003].

An average decrease of $\sim 40\%$ in responsivity was reported by Hopkinson after $\sim 80 \text{ krad}$ of ionizing dose. The shape of the spectral curve did not change after irradiation, only the absolute responsivity. This reduction is believed due to a reduction of the gain in the pixel. No degradation was seen under proton bombardment [Hopkinson 2004]. Cypress reports a 10 to 20% wavelength dependent decrease in responsivity due to ionizing radiation. No measureable degradation of the photo-response due to displacement damage was observed [Cypress Document 2005].

The STAR1000 CMOS sensor has a format of 1024×1024 with $15 \mu\text{m}$ 3T pixels and is front illuminated. The device has a readnoise of $\sim 47 \text{ e}^-$ and a dark current of 223 pA/cm^2 in a clear environment. Full well was $135,000 \text{ e}^-$. Peak quantum efficiency was $\sim 30\%$. No latchup was observed at $> 127.8 \text{ MeV cm}^3/\text{mg}$ [Cypress Document 2007]

The response of the STAR1000 has also recently been examined [Duvet et al. 2006]. The expected major influence of proton irradiation on this device was dark current. Protons create dark current and also “RTS” (Random Telegraph Noise). A linear fit of dark current versus temperature yielded the activation energy of $\sim 0.67 \text{ eV}$ expected for silicon. If only lower temperature points are considered, the derived activation energy drops to 0.46 eV . The mean

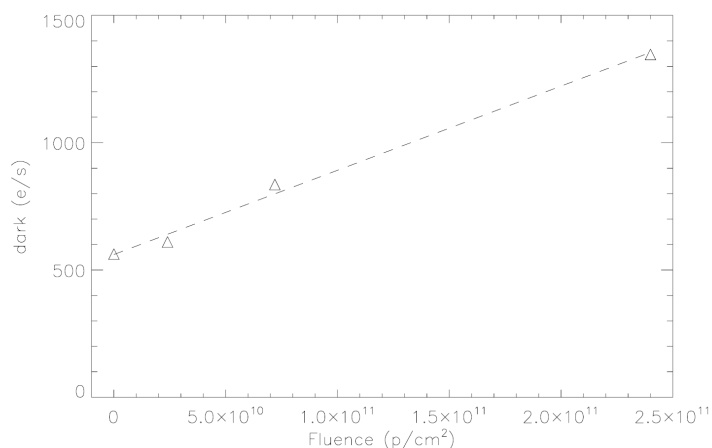


Figure 5–11. Variation of the mean dark current (at 298K) with respect to fluence. [From Duvet et al. 2006]

dark current evolves linearly with fluence as shown in **Figure 5–11**. **Figure 5–12** shows the dark current distribution prior to irradiation and after consecutive irradiations. The evidence of hot pixels is indicated by the observing the tail of the distribution.

Cypress states they have studied total ionizing dose damage in detail and have developed proprietary design techniques to enhance TID tolerance. Both the STAR250 and 1000 are processed using the standard 0.5 μm AMI CMOS technology and their

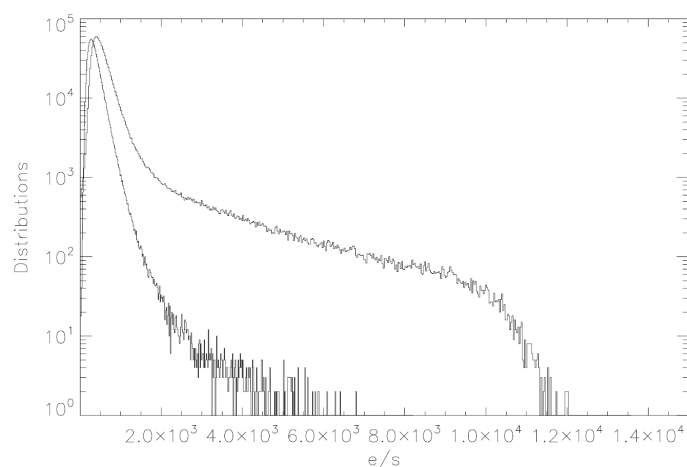


Figure 5–12. The initial and final dark current distribution for which a large tail of hot pixels can be observed. [Duvet et al. 2006]

radiation-tolerant layout rules were applied throughout both designs. All NMOS transistors and photodiodes were designed with special gate geometries and additional guarding structures to reduce or eliminate ionizing radiation degradation effects [Cypress Document 2005].

The p-n-p and n-p-n parasitic bipolar transistors that are inherent in CMOS structures may cause radiation induced latch-up. The guarding of transistors which is a consequence of the design rules mentioned above, reduces the

distributed resistance across any base-emitter junction. This results in highly improved latch-up immunity.

Displacement damage is a consequence of the fundamental interaction of protons with the silicon resulting in the production of defects, which cannot be avoided. Dark current was found to scale proportionally with the depleted volume of the silicon material in which defects are created. Cypress states that the STAR sensors are designed using a proprietary technique that collects photo-

charges in a pixel with a small photodiode and high quantum efficiency. The dark current increase after proton irradiation appears to be significantly lower than in CCDs due to the STAR sensors significantly smaller pixel depletion volume that determines the number of elastic and inelastic recoils in each pixel.

Cypress states that dark current and its non-uniformity increase rapidly with Co^{60} irradiation similar to that of CCDs, however, voltage threshold shifts are much less for CMOS imagers due to their very thin oxides. The sensors use an on-chip Fixed Pattern Noise (FPN) correction scheme to deal with radiation induced voltage

variations. Measurements reveal no increase in FPN with ionizing radiation. The remaining FPN is well below 0.4% of full well for the whole array.

Finally, CCD-like transfers are absent in CMOS imagers, thus eliminating a major degradation mechanism resulting from ionizing radiation or displacement damage.

5.2.2 Transient Effects

Transient radiation effects occur when an energetic particle (electron or proton) traverses the active signal generating volume of a detector such as a CCD or CMOS imager and creates an ionization trail thus producing a false signal. In this respect both CCDs and CMOS imagers are similar since they are based on silicon material and in general have similar pixel volumes. CMOS detectors with small depletion volume pixels such as the STAR sensors described above have the greatest immunity to this effect and are expected to outperform p-channel CCDs with thick silicon absorption regions. Transient signal effects are not permanent, and the spurious charge is swept out during readout but the additional charge constitutes a source of noise in the image.

The CMOS imager will experience the same secondary environment behind the shield as the previously mentioned for CCD devices. The shield is expected to pass > 30 MeV electrons at a flux of $\sim 4.28 \times 10^5$ electrons/cm²/sec at 9 R_j and 3.5×10^6 e⁻/cm²/sec at 5 R_j. The shield will pass > 100 MeV protons with an \sim flux of 50 protons/cm²/sec at 9 R_j and 920 p/cm²/sec at 5 R_j. It is estimated that shield-penetrating electrons produce 1000 to 2000 secondaries in the silicon pixel material. Protons are estimated to deposit ~ 1.4 keV/ μ m for 100 MeV protons. Given a 10 micron depletion width and an electron-hole pair production energy of 3.6 eV/e-h the number of carrier pairs produced is at least $\sim 4,000$. Given the uncertainties in incident angle carrier

generation from 100 MeV protons could reach $\sim 10,000$. Less energetic protons would produce even higher numbers of carrier pairs, since the linear energy transfer (LET) increases with decreasing proton energies

Details of the chosen CMOS imager device will affect the noise calculation of the impact of transient radiation behind the shield. In general CMOS imagers will have similar pixel sizes and active regions as the CCDs previously discussed and thus the estimated 4.1% pixel hit by energetic electrons at 9 R_j and 32% at 5 R_j will be approximately similar [see Section 5.1.2]. These transient electrons will generate ~ 317 e⁻ at 9 R_j and ~ 885 e⁻ of noise at 5 R_j. A further increase in noise might occur if the integration time of the CMOS imager must be extended to compensate for the possible reduction in quantum efficiency. The QE values though are dependent on the type of CMOS imager chosen. Also in general, the incident particles may affect nearest neighbor pixels but these pixels should share the charge generated.

For the STAR1000 mentioned above, the well capacity is $\sim 135,000$ electrons and with reasonable signal, the additional false charge for thin devices should not significantly affect the system signal-to-noise. However, the transients will prohibit the detection of small signals as a consequence of possible increased integration times and lower absolute incident signal photons. Theoretically the transient hits produced by the incident electrons (or protons) will be spatially random, are swept out in an integration time and could potentially be filtered out using signal processing electronics.

Protons will produce a much higher false signal per hit but are far fewer, 50 p/cm²/sec at 9 R_j and 920 p/cm²/sec at 5 R_j. Assuming a pair-production of 10,000 carriers, these hits will be imaged as bright pixels and will most likely be unusable. In the worst case of 5 R_j, ~ 0.1 % of the pixels would be affected per frame. If signal processing is used, this large event can be discriminated and dropped.

5.2.3 Mitigation Techniques

Since CMOS imagers are also based on single crystal silicon material many of the mitigation approaches suggested for CCDs will be similar. These include increasing the shielding, choice of device architecture, reducing active region volumes to decrease displacement damage generated dark current and decrease response to transient events, and use of pinned photodiodes (PPD) to reduce surface and interface generated dark currents. Thin oxides can reduce flatband voltage shifts due to ionizing radiation and can be very effective when used with flexible biasing to further mitigate any threshold shifts.

Dark current can be significantly reduced by cooling since CMOS imagers have the same exponential dependence on inverse temperature as CCDs. Cooling suppresses dark current by increasing the emission times of particle induced traps.

Three key approaches for hardening CMOS which were mentioned previously are: 1) radiation hardness by design, 2) use of a radiation hardened foundry process and 3) more recently, use of new process variations in modern submicron fabrication processes to mitigate radiation effects. Radiation hardening by design requires increased silicon real estate or area while radiation hardened foundries are few, have longer turn around times, reduced process stabilities and larger feature sizes. The hybrid approach which combines radiation hardening by design with key process changes in new submicron processes appears to be more ideal.

Data processing software can be utilized to discriminate against transient events and permanent dark current spikes. Techniques include subframe data sampling, thresholding and dropping bad pixels and good pixel averaging.

Periodic heating (annealing) of the CMOS imager at higher temperature even to room temperature and perhaps to 100-150 °C

to anneal out trap centers and improve performance and reduce dark current may also be effective.

5.2.4 Planetary Protection

JEO's baseline approaches for meeting planetary protection sterilization requirements include dry heat sterilization at 125 °C for 50 hours for qualification and 115 °C for 50 hours for acceptance testing, analysis proving that a sterilizing ionizing dose of 7 Mrad(Si) or unit assembly and test under sterile conditions through ATLO. Dry heat sterilization is viewed as the most practical approach, considering the logistical difficulty of assembly and test under sterile conditions, and the inability of most CCD devices to withstand an ionizing dose of 7 Mrad(Si).

Silicon CMOS imaging devices are fairly robust to the level of temperature cycling listed above and could be sterilized at these times and temperatures. However, they are likely to be packaged with adhesives, or optical coating processes that will not withstand EJS dry heat sterilization requirements. Typically ceramic packages are used which are temperature resistant. The packaging and coating processes will depend on particular applications and will need to be assessed. The imager chip will then likely be integrated with the system including coolers. The assembly and test procedures will need to be reviewed and modified.

5.2.5 Overall Assessment

Demanding high performance scientific applications in the visible wavelength region have favored CCD technology due to its very low readnoise ($\sim 2 e^-$), lower dark current and higher quantum efficiency. However, much of this low noise advantage may be lost under high radiation environments. More recently CMOS or Active Pixel Sensors have gained in performance. Although typical CMOS imager readnoise ($\sim 30 e^-$) and dark currents are higher, under many environments shot noise

from the signal may dominate. (A recent advanced CMOS imager was reported with ~ 2 e^- readnoise as mentioned previously). If cooling is permitted or desired than the dark current impediment is reduced. New CMOS designs now incorporate micro lenses or thinned backside illumination to improve the quantum efficiency.

A major advantage for CMOS imagers in a radiation environment is their addressing scheme. CMOS pixels are readout through an X-Y direct addressing approach while CCD devices use a charge transfer approach. Although the CCD can have very high and noiseless transfer efficiency (CTE), this attribute is seriously affected by particle irradiation. Readout schemes for CCDs must carefully balance temperature, bias and clocking rates for maximum performance. In addition, if any one pixel in a particular vertical column or horizontal transfer line is seriously affected, than any signal detected above that affected channel will also be affected.

CMOS imagers are unaffected by issues related to CTE. The main influence of both ionizing and displacement damage dose appear as an increase in dark current. The first mitigation technique to reduce this degradation is to cool the device, since dark currents decrease exponentially with temperature. System constraints put a limit to this mitigation technique. Recent CMOS designs that incorporate pinned photodiodes and various guard ring approaches appear to offer a high level of performance under both ionizing and displacement damage radiation environments. The underlying material for both CCD and CMOS architectures is single crystal high purity silicon.

Recently p-channel CCDs have offered improved CTE performance under radiation environment. They utilize high resistivity n-type silicon and currently operate with large (~ 200 μm) depletion regions. The thick n-type silicon used in the p-channel devices to date,

make them venerable to higher transient effects. These devices could be thinned. Currently CMOS devices based on p-type material already have been shown to operate with higher quantum efficiency using a thinned backside illuminated architecture.

Hardened 1k x 1k CMOS imagers are commercially available as discussed previously. These devices have been extensively characterized under radiation environments and it is expected that they will be further scrutinized. This technology may be further hardened through the promise of the hybrid approach of combining radiation hardness by design with key specific process variations in some of the new submicron technologies. CMOS imagers should be considered a serious contender for the Jupiter Europa Orbiter Mission applications.

5.3 Performance of the Charge Coupled Imager in the Galileo Solid-State Imaging System

5.3.1 Introduction

The Galileo spacecraft containing the Solid-State Imaging subsystem (SSI) successfully inserted into orbit around Jupiter on December 7, 1995. Subsequently, the SSI acquired a total of 1645 frames of visible data during its 2-year prime mission and an additional 1453 frames during its 4-year extended mission. The SSI stably maintained its calibration throughout its total of 12 years of flight time, delivering valuable data until its end of mission.

The SSI consisted of a 1.5 m focal length Cassegrain telescope coupled to a visible charge coupled device (CCD) with an 800 x 800 format. Spectral discrimination was accomplished through the use of eight spectral filters. The camera head consisted of a radiatively cooled CCD and supporting electronics behind a radiation-shield of 1-cm thick tantalum. The shield completely surrounds the CCD package, except for the

required imaging aperture, which is filled with a flat quartz plug. [Table 5–4](#) lists the physical characteristics and performance parameters of the SSI. [Klassen 1984]

The CCD image sensor is a virtual phase, buried-channel, frontside-illuminated, 800 x 800 device developed by Texas Instruments Inc. The CCD uses a polysilicon gate structure with 15.2- μm -pixel pitch. The serial register is located at the bottom of the array and is 825 pixels long. Each serial pixel is 20 μm x 15.2 μm and has ~ twice the charge capacity of the vertical pixels. The virtual phase (VP) CCD is composed of two potential wells permanently formed by implantation. The charge transfer potential wells are formed under the gate structure in part by ion implantation and in part by the voltage applied to the gate. Charge is transferred in each cycle by switching the gate voltage, with each cycle sequentially forcing the signal charge from a virtual phase to a clock phase to a virtual phase. This is repeated until each of the 800 lines has been readout. [Klassen 1984]

A dose of 2.5 krad(Si) was expected for the Galileo mission. In fact at the end of the

extended mission the device experienced a total dose of 4 krad(Si) with no significant degradation observed. This was primarily due to Jovian trapped radiation. The device also experienced ~ 50,000 energetic neutrons (0.5 to 5 MeV typically) from the onboard plutonium power source . Prior to launch, tests were performed on similar VP CCDs that showed that, at 10 krad(Si) dose of Co^{60} , dark current was not influenced by the radiation as long as the interface remained inverted during the integration. The VP CCD had low susceptibility to trapped charge buildup in the oxide resulting in flatband shifts of less than .01 V/krad(Si). [Klassen 2003, Klassen 1984]

5.3.2 Radiation Effects

2 x 2 Summation Mode

The Galileo CCD had the ability to operate in an on chip 2 x 2 summation mode. The summation mode enhances the signal-to-noise since the faster readout rate reduces the radiation exposure duration and secondly the signal charge adds directly while the noise adds as the square root. The outcome of the 2 x

Table 5–4: Performance parameters and physical characteristics of the SSI [from Klassen 1984]

Parameter	Value
Angular resolution	10.16 $\mu\text{rad}/\text{pixel}$
Shortest exposure	4 1/6 ms
Longest exposure	51.2 s
Active CCD area	12.19 mm x 12.19 mm
Array aspect ratio	1 to 1
Pixel aspect ratio	1 to 1
Pixel center-to-center spacing	15.2 μm
Active lines per frame	800
Active pixels per line	800
CCD full-well capacity	1 x 10 ⁵ electrons
Dark current	< 10 electrons/pixel
Bits/picture element	8 raw and 3.24 compressed
Readout noise	~ 30 electrons rms/pixel
Number of filters	8
Gain states	4 (1, 4, 10, 40)
Mass	28 kg

2 summation technique is to transform the 800 x 800 image into a 400 x 400 image allowing it to be read out in ¼ of the time without changing the data rate output.

The first sign that permanent radiation damage had occurred in the SSI occurred on orbit C22 in some images taken using the camera's 2 x 2 pixel summation mode. Almost all the frames in this orbit exhibited a pattern of vertical bars of either higher or lower signal level than that of the average. This artifact gradually affected fewer and fewer lines as the spacecraft moved farther from Jupiter suggesting a possible correlation with radiation dose rate.

In the next SSI imaging case the spacecraft was flown as deep into the Jovian radiation field as Io's orbit. Accumulating radiation dose caused a more serious problem with the summation mode readout. Incomplete charge transfer may have occurred resulting in smeared outputs. Parts in the horizontal clock control circuitry were identified that could cause this failure. As a consequence there was no further use of the summation-modes. [Klassen 1984]

Flood Illumination

The VP CCD, which was frontside illuminated and not thinned, exhibited a phenomenon called "residual bulk image". Light with wavelengths longer than ~ 700 nm can penetrate deeply into the bulk silicon and generate carriers below the shallow, high-resistivity epitaxial layer where most signal electrons are produced. The boundary between the epitaxial layer and the bulk silicon can trap charge. These traps once filled can remain filled from seconds to days at the -110 °C operating temperature of the CCD. The SSI used a 900-nm LED flash lamp to keep these traps filled, maximizing and stabilizing the detector quantum efficiency.

During the mission it was determined that the light flood illumination function could no longer be successfully utilized. Subsequent

testbed analysis indicated that the light flood was not the primary cause, while the probable cause was a specific op-amp in the SSI sample and hold circuit. There was not clear correlation of radiation flux rate with the onset of the anomaly; however, it may have been a cumulative effect. The only apparent remedy was to power cycle the camera. [Klassen 2003]

CCD Column Blemishes

Column blemishes are believed to be a consequence of single-pixel defects or "hot pixels". The hot pixels are believed produced by high-energy particle radiation damage from solar flares and/or by neutrons originating from the radioisotope thermoelectric generator. The defected pixel generates excess dark current, which is collected during the time from the end of one image readout or CCD reset cycle to the beginning of the next image readout. As the image is clocked out, each subsequent charge packet in the same column must pass through this pixel, resulting in excess charge integration for all pixels in the column below the head pixel, forming a column blemish. The detectability of a column blemish in the data from any particular orbit depended strongly on readout rate, gain state, background level of the scene and data compression. In the extended mission, most orbits featured close encounters with Europa or Io. Imaging in these instances used faster frame rates and lower gain states, resulting in the appearance of none to few column blemishes. Other Jovian orbits that used slow frame rates, or lower light level imaging which used high gain states tended to show many column blemishes. A gradual increase in the number of column blemishes was observed throughout the mission.

It is important to note that even after a 12-year flight with 6 years in Jovian orbit, the number of column blemishes were small enough and weak enough in intensity as not to materially affect the quality of the science data from the SSI, except perhaps in the extreme

low light level cases of observations. The robustness is primarily attributed to operation of the CCD as -110°C . [Klassen 2003]

Dark Current

One of the most important parameters of the CCD is its dark current. As mentioned previously in the CCD Section, contributions from surface states in the silicon have been shown to be the dominant contributor to dark current. Use of the virtual phase CCD design greatly suppresses this current through channel inversion. The dark current measured under these conditions was 0.4 nA/cm^2 at 25°C . Dark current spikes, however, were a concern since the virtual phase CCD is typically operated under higher electric fields and is fabricated with more high energy implants

than other types of CCDs. Typical dark current rates for the spikes were in the range of 10^2 to 10^5 nA/cm^2 at 25°C . An operating temperature of -110°C was chosen for the CCD. This device produced $\sim 10^{-5}$ electrons/pixel/s at -110°C with dark current spikes in the range from .01 to 10 electrons/pixel/s. [Klassen 2003, Klassen 1999]

At the very end of the extended mission a number of dark frames were acquired at a series of warmer temperatures. Figure 5–13 plots the observed end of mission dark current rates within selected columns of the CCD as a function of temperature. The pre-launch dark current is also plotted. Every column exhibited some increase in dark current by the end of the mission. The columns with the most dark current behaved irregularly with temperature

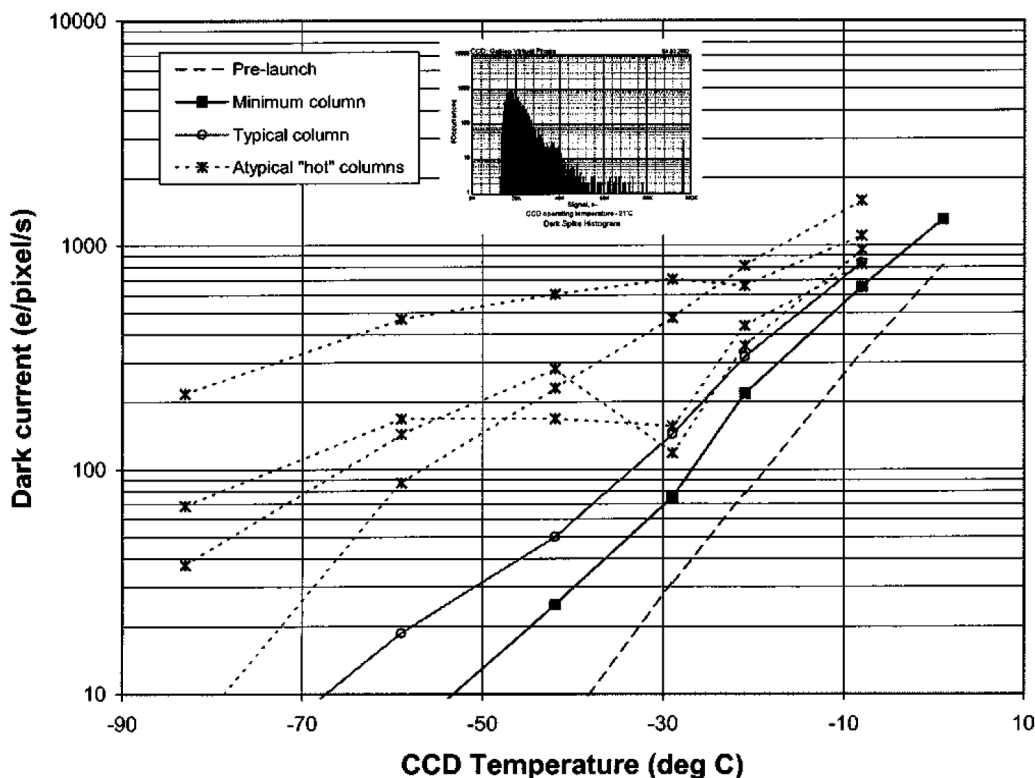


Figure 5–13. End-of-mission CCD dark current rate as a function of temperature. The pre-launch dark current is also plotted. The inserted histogram shows the distribution of signal levels in the -21°C image; the horizontal scale runs from 0 to 100,000 e^- and the signal integration time is $60\frac{2}{3}$ seconds. Signal saturation occurs at 96,400 e^- . [from Klassen 2003]

possibly due to more than one damage site within the column. The end-of-mission dark frame results indicate it would have been acceptable to operate the CCD at a temperature as warm as -70°C without significant degradation in performance. Since a significant level of hot-pixel annealing was observed during the mission, the choice of -110°C now seems conservative. [Klassen 2003]

Transients

The Ta shield together with the optics and other structural elements (primarily aluminum) permitted only $\sim 10^{-4}$ of the externally incident electrons to penetrate to the CCD, with about 25% of them coming from the quartz plug. In the process of stopping most of the high-energy electrons, Bremsstrahlung gamma rays were produced. These rays in turn interact with the shield material and the CCD itself to generate a flux of secondaries. The spectra of both the primary and secondary electrons at the CCD generally peaked around 3 MeV, with about 70% of the particles falling between 1 and 10 MeV.

Empirical data was acquired in the laboratory on the details of the electron interaction with the CCD. A test setup was constructed that used a strontium-90 radiation source that emitted 2 MeV electrons. Individual strontium-90 interactions were observed by reducing the event rate. A mean value of 1440 electrons per hit was measured and compared favorably with a theoretically calculated value of 1500 electrons. In addition it was found that the transient particle generated charge was generally confined within a 3×3 pixel area with the central pixel capturing 65% of the charge and each of the side pixels capturing between 5 and 10% of

the charge. The diagonal pixels of the 3×3 subarray each captured $< 2\%$ of the generated charge. [Klassen 1984]

Increased noise levels in CCDs can be caused by incident energetic particles depositing energy along their pathlengths as they pass through the device. A single radiation “hit” in an image appears as a small cluster of pixels with elevated signal levels.

Data on the effect of transients was acquired during the extended mission down to $5.9 R_J$, enabling the determination of the radiation event rate down to Io’s orbit. It was found that, at least during the epoch of the Galileo encounters, the radiation levels at Io were less severe than the worse case fears. Good quality data could be obtained using the $8 \frac{2}{3}$ second integration time modes.

Analysis techniques used images with rectangular regions that contained only black sky or shadowed areas, free from obvious scattered light, column blemishes and other extraneous signal sources. The size of these regions ranged from 2000 to 120,000 pixels. **Figure 5–14** is a plot of the measured SSI radiation charge rate as a function of the range to Jupiter. [Klassen 2000]

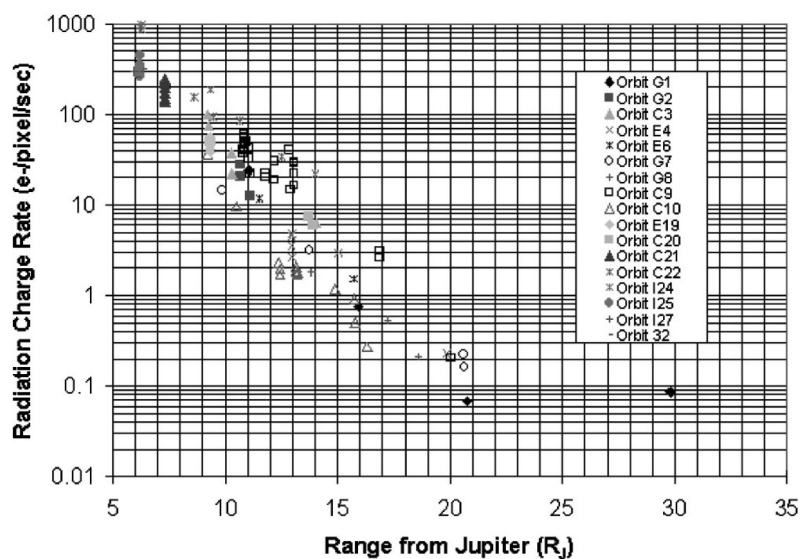


Figure 5–14. Radiation-induced signal rates in the SSI images as a function of the spacecraft distance from Jupiter in Jovian radii ($R_J = 71,398 \text{ km}$). [from Klassen 2003]

Extrapolation of the data to $5R_J$ yields ~ 1000 electrons/pixel/sec induced signal rate. If the average of 1440 electrons per hit of 2 MeV electrons is used then there is an approximate hit rate of 0.69 particles per pixel per second. (It is expected that electrons with energies on the order of 10 MeV are expected for the Europa mission with subsequently lower linear energy transfer rates and therefore lower carrier generation rates. Integration times for the notional Jupiter Europa Mission are in the tens of milliseconds). For the typical $8\frac{2}{3}$ second integration times used for the SSI, there are ~ 6 hits per frame per second. These hits produce $\sim 8,666\text{ e}^-$ per pixel per image frame. As mentioned previously, good quality data could be obtained at Io using the $8\frac{2}{3}$ second integration times.

5.3.4 Summary

The Solid State Imaging subsystem successfully completed a 2-year primary mission and a 6-year extended mission around Jupiter. Photons were detected using a virtual phase CCD with low dark current and which operated at -110°C . The CCD endured the harsh radiation environment of Jupiter. Behind a 1 cm shield of Ta, the device accumulated a total dose of 4 krad(Si). It exhibited increases in dark current as a function of mission time, but the low operating temperature kept the CCD dark current acceptable. Hot pixels were observed to anneal with time during the mission resulting in a conclusion that it would be possible to successfully operate the CCD at -70°C . [Klassen 2003]

Some column blemishes were observed as a result of radiation induced dark current increases in some pixels (hot pixels). After a 12-year flight with 6 years in Jovian orbit, the numbers of column blemishes were small enough and weak enough in intensity as not to materially affect the quality of the science data from the SSI, except perhaps in the extreme low light level cases of observations. The

robustness is primarily attributed to operation of the CCD as -110°C .

The external clock circuitry of the SSI was affected by radiation resulting in the abandonment of the use of the 2×2 summary mode intended to increase signal to noise. The LED flood light technique to improve image quality was also discontinued due to a speculated radiation-induced failure of an operational amplifier.

Finally, data on the effect of transients was acquired during the extended mission down to $5.9 R_J$, enabling the determination of the radiation event rate down to Io's orbit. It was found that, at least during the epoch of the Galileo encounters, the radiation levels at Io were less severe than the worse case fears. Good quality data could be obtained using the $8\frac{2}{3}$ second integration time modes.

Even in the most extreme radiation fluxes encountered, good quality imaging continued to be possible. 1453 images were successfully returned during the extended mission and 1645 images during the primary mission. Some of the problems encountered with the SSI camera system did cause the loss of some valuable data. However, overall the SSI investigation was successful. "The Galileo SSI demonstrated the quality and reliability of the CCD as a detector of choice for spaceborne scientific imagers." [Klassen 2003]

6 Infrared Detector Technology

Two major technologies are envisioned to assist in capturing infrared (IR) science data during the baselines Jupiter Europa Orbiter Mission. They are direct photon detector and the thermal detector. The direct photon detectors of interest are those based on a direct bandgap semiconductor material with a bandgap small enough to detect mid-wavelength photons out to $\sim 5\ \mu\text{m}$. Photons are absorbed in the material's valence band. Energetic minority carriers then transition the bandgap to the conduction band where they are then swept away by a photodiode and counted as signal. HgCdTe is currently the most widely used material. Image detection is achieved by array of photodiode fabricated in the HgCdTe material. These arrays must be cryogenically cooled in order to suppress thermal dark currents that could potentially mask the detected signals.

Thermal detectors and arrays detect IR radiation by an indirect technique. These devices are designed to absorb IR radiation and as a consequence increase their temperature. This minute temperature increase is then detected in each pixel by a series of micro-thermopiles consisting of the connection of two dissimilar metals. A small voltage is generated from the thermopiles as a consequence of a small change in temperature. This small voltage is then amplified by a nearby silicon CMOS amplifier and is then transferred as a signal voltage. These devices are typically uncooled.

The next Section will address the radiation hardness of cryogenically cooled mid wavelength infrared (MWIR) photon detector arrays fabricated in HgCdTe material. This discussion will be followed by a Section dealing with the radiation hardness of uncooled micro-thermopile detector arrays that detect much longer wavelength infrared radiation.

6.1 MWIR Focal Plane Arrays

$\text{Hg}_{1-x}\text{Cd}_x\text{Te}$ is currently the most widely used infrared detector material. It is a single crystal alloy that allows small compositional variations. HgCdTe material can be grown to respond to IR wavelengths ranging from $\sim 1.5\ \mu\text{m}$ to $\sim 20\ \mu\text{m}$ by varying the HgTe-to-CdTe ratio. (The composition that responds out to a cutoff of $\sim 5\ \mu\text{m}$ is $\text{Hg}_{0.7}\text{Cd}_{0.3}\text{Te}$). This ability to tune HgCdTe to the exact cutoff of interest offers a performance edge in terms of lower dark current when compared to a competitive material such as InSb that has a fixed cutoff of $\sim 5.4\ \mu\text{m}$.

Modern infrared focal planes arrays (IR FPAs) are hybrid devices consisting of two different chips; a separate photodiode array of p/n junctions fabricated in HgCdTe material and a separate array of preamplifiers and signal processing circuits fabricated using CMOS silicon technology. There is a one to one correspondence between each IR photodiode unit cell to the underlying silicon circuit unit cell through an indium bump interconnect. Formats ranging from 512×512 to $2k \times 2k$ are readily available. The CMOS silicon readout chip functions in a similar manner to the visible CMOS imager. Each unit cell is directly addressable thus eliminating any charge transfer inefficiencies that could be caused by radiation. The simplest CMOS readout amplifier configuration for the IR FPA is based on a source follower per detector and is equivalent to the common 3 transistor (3T) design used in visible CMOS imagers.

Analogous to the radiation response of the visible imagers, IR imagers are subject to degradation affects as a consequence to exposure to Total Ionizing Dose (TID) and displacement damage caused by energetic particles. These devices are also affected by transient particle irradiation. Since IR FPAs are hybrid devices their radiation response will be a combination of effects induced in both the infrared HgCdTe photodiode array and the underlying CMOS readout array.

6.1.1 Total Dose and Displacement Damage Survivability

Total Ionizing Dose

Multielement arrays require surface passivation between individual detector elements or pixels. In the 1980's deposited ZnS material was utilized as a passivation layer and was found very effective at trapping total ionizing dose induced charge and producing degradation. Thus TID degradation became a critical issue. It was found that the quality of the interface between the passivation layer and the HgCdTe was key to hardened devices. Unpassivated devices were found to be hard to $\sim 3 \times 10^6$ rad(HgCdTe) and ionization induced trapped charge was found to anneal out by 300K. Periodic heating of HgCdTe arrays could effectively remove all the radiation damage [Pickel 2003].

It was found that with proper surface treatments ZnS passivated could be hardened against TID. MWIR linear and 2 dimensional FPAs were irradiated with 2 MeV electrons in 15 ns pulses. R_0 values decreased by a factor of 2 as dose was increased to ~ 1.5 Mrad(Si). R_0 is defined as the inverse differential resistance, $1/dI/dV$, at zero detector bias and is used as a figure of merit for the electrical performance of the device. Higher R_0 is better. No permanent damage was observed. A slight decrease in responsivity was also observed. Both resistance and responsivity changes annealed out at 220K [Williams et al. 1987].

Currently, most manufacturers are believed to utilize CdTe-passivated HgCdTe detector arrays and have adopted a thin p-type layer on an n-type $10 \mu\text{m}$ IR absorbing layer as their standard photodiode architecture. The improved passivation is considered revolutionary to hardness improvement of the detectors. **Figure 6-1** plots a figure of merit, the resistance-area product at zero bias, R_0A , as a function of total dose. CdTe and CdTe/ZnS passivated MWIR HgCdTe detectors are seen to be hard to > 1 Mrad of

TID at the devices operating temperature of 80K [Lee et al. 2006].

Total dose effects can be more severe at cryogenic temperatures for CMOS readout devices. Much of the previous discussion concerning the hardening of CMOS visible imagers is applicable to IR readout devices. Modern trends toward high density and thinner oxides are favorable toward improved hardness. Use of hardened foundry processes and hardening by design practices combined with submicron processes have allowed radiation tolerant readouts to be fabricated in commercial foundries. The formation of leakage paths degrade the analog signal voltages stored in the CMOS unit cells. Radiation hardening by design experiments utilized CMOS imagers that contain similar CMOS readout circuits to IR devices. These circuits were found to be hardened against TID to > 1 Mrad(Si) [Eid 2001, Pain 2004].

Characterization tests were performed on two prototype candidate infrared focal plane arrays for JWST's near-infrared (NIR) instruments [McKelvey et al. 2004]. These were the Teledyne HIRG readout mated to a

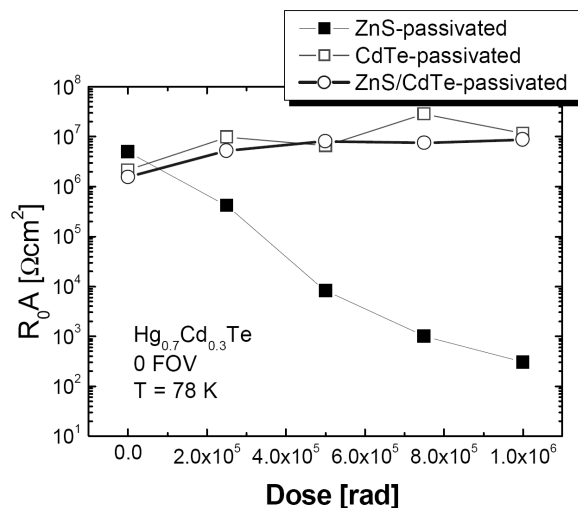


Figure 6-1. Changes of the dynamic resistance-area product (R_0A) values at zero bias as a function of total ionizing dose. CdTe and ZnS/CdTe passivation layers are seen to be hardened against total ionizing dose. [From Lee et al. 2006]

detector array using MWIR HgCdTe and the Raytheon Vision System's SB291 readout mated to an InSb detector array. Both were 1024 x 1024 FPAs that utilized source-followers per detector readout unit cells (similar to CMOS visible imager unit cells) and were not designed to be specifically radiation hardened. The HIRG was operated at 37K and the SB291 at 30K. Of the various total dose related performance factors, radiation activated dark current received most attention.

Since the devices were cooled to 30K or 37K the detector dark current was very low necessitating very long integration times in perfectly dark cryostats to be detectable. The dark currents were hard to accurately characterize. Baseline pre-irradiation dark currents were of the order of milli-electrons per second. (Europa's notional IR Spectrometer will operate at 80K using an MWIR HgCdTe FPA). The devices were irradiated to a total dose of 5 krad(Si) for these measurements using 63 MeV protons. (No fluence was stated). Displacement damage is believed to be the predominant mechanism leading to increased dark current.

The major affect of the irradiation is an increase in the dark current distribution. A "hot" pixel threshold was chosen at 6 sigma to the distribution which resulted in the degradation of 10% of the tested population. It is important to note that the absolute dark currents for this device had "hot" pixels which were still $< 0.8 \text{ e}^-/\text{s}$ due to the 37K temperature. Responsivity was observed to decrease by a few percent. The temperatures and dark currents are well below those expected for the "notional" IR detector of the Visible Infrared Imaging Spectrometer (VIRIS).

Separate CMOS silicon readout chips were irradiated up to 50 krad(Si) with protons. No proton fluence was stated. The source follower output voltage was measured as a function of dose. These measurements are an

indication of the true radiation hardness of the readout. The Teledyne readout showed essentially no radiation damage degradation to a proton induced 50 krad (which was the limit of the test). The Raytheon readout stopped working at between 20 and 30 krad(Si). This device was not intentionally designed as radiation hard.

Displacement Damage Dose

In the 1970's a large number of investigations addressed displacement damage dose in HgCdTe material. Much of this work was on discrete devices. Displacement damage dose was not considered the primary problem in these early years due to the influence of total ionizing dose. This damage was thought responsible for the creation of generation-recombination centers that subsequently degrade single crystal material lifetime. Material lifetime in turn controls the optical response of the detectors. Displacement damage thresholds were defined for HgCdTe in which device responsivity degraded by a factor of two. These levels were high, $6 \times 10^{14} \text{ e}^-/\text{cm}^2$ for 2 MeV electrons, $1 \times 10^{14} \text{ n}^-/\text{cm}^2$ for 14 MeV neutrons and $6 \times 10^7 \text{ rad(HgCdTe)}$ for Co^{60} gammas. Once the TID degradation issues were solved displacement damage again became more important. However, the displacement damage thresholds of many detector materials is still high enough that displacement damage should not be a major issue [Pickel 2003].

Very limited data exists in literature concerning the radiation effects on HgCdTe detectors. The effects of proton irradiation on LWIR HgCdTe photodetectors were examined in a paper by Kelly [M. Kelly et al. 2003]. The large area devices (1 mm in diameter) were engineering grade devices fabricated for the Cross-track Infrared Sounder (CrIS). The devices were operated at $\sim 78\text{K}$ and have very long wavelength responses of $> 15 \mu\text{m}$. Twenty two different detectors were irradiated with a variety of proton energies and fluences.

Current-voltage characteristics were acquired before and after irradiation as a function of bias. All the devices were irradiated to an equivalent rad(Si) of 8 krad. Using 99 MeV protons the equivalence was 8.5×10^{10} p/cm² which yields a displacement damage dose (D_d) of $\sim 1.4 \times 10^8$ MeV/g. At 153 MeV the 8 krad equivalence was reached using a fluence of 1.2×10^{11} p/cm² which yields a D_d of $\sim 1.9 \times 10^8$ MeV/g. These displacement dose values are approximately the same as those that would be experienced by the Europa mission behind 1 cm of Ta shielding.

Dark current was found to increase with higher energy protons. In general the change in dark current was small following lower fluence levels and increased as 4×10^{12} p/cm² is approached. The dynamic impedance at -60 mV bias decreased with increasing fluence for all energy exposures. The threshold for dynamic impedance decrease was $\sim 4 \times 10^{11}$ p/cm² using 99 and 153 MeV protons. The primary microscopic mechanism that increases dark current was attributed to tunneling. The worst-case exposure at 153 MeV at 1.2×10^{11} p/cm² increased the detector noise by only 0.75%. The maximum noise increase was $\sim 47\%$ which occurred at 4×10^{12} p/cm² using 99 MeV protons, corresponding to 372 krad(Si). Annealing at room temperature for 96 hours was found to reduce only some of the noise induced by the high energy protons.

The devices discussed above were very long wavelength devices (cutoff wavelength $>15 \mu\text{m}$) as compared to the VIRIS MWIR HgCdTe notional focal plane with response to $5 \mu\text{m}$. It is expected that the MWIR devices would be much less affected by dark current increases and that the primary dark current mechanism would be from a particle induced generation-recombination center as opposed to a tunneling mechanism. MWIR HgCdTe detectors are expected to be much harder to radiation than the LWIR devices discussed above.

Hot pixel generation in an engineering grade MWIR 2kx2k HgCdTe focal plane array (similar to arrays that would be used in JWST) was recently reported [Marshall *et al.* 2007]. The device was irradiated with 63 MeV protons at a fluence of 3.7×10^{10} cm⁻² (D_d of $\sim 3.7 \times 10^7$ MeV/g which is $\sim 3.5 \times$ less than Europa). Dark current was acquired at the JWST temperature of 37K. At this dark current the absolute values of both the pre and post irradiation were very small as seen in Figure 6–2. The major affect with proton bombardment appears to be an increase in the distribution tail which would be associated with “hot” pixels. For these very low temperatures the tail reached only 0.8 electrons/sec which is still a very low dark current value. Note also the notional MWIR focal plane for the Infrared Spectrometer for Europa will operate at 80K and consequently produce more dark current. However, the main effect of proton irradiation at 37K appears to be an increase in the higher dark current tail of the distribution as opposed to a massive increase in dark current.

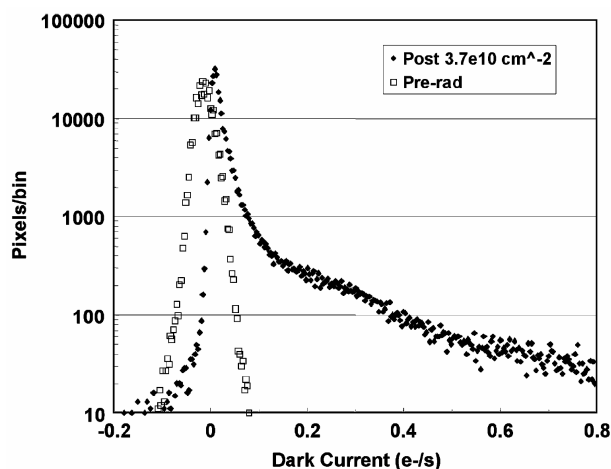


*Figure 6–2. Measured dark current distribution of 266,000 selected pixels of Hg_{0.7}Cd_{0.3}Te IR focal plane before and after irradiation with 3.7×10^{10} cm⁻² 63 MeV protons. The data represent measured absolute values and the negative numbers reflect measurement noise in the system. The mean dark current values are extremely small as expected for operation at 37K. [From Marshall *et al.* 2007]*

Displacement damage effects were found recently to primarily degrade the performance of HgCdTe detector arrays through increased dark current, reduction in responsivity and degraded uniformity [Hubbs *et al.* 2007]. Measured results were shown that indicated a decrease in responsivity with increasing proton flux. The loss in responsivity was isolated to the detector and its root cause is related to detector design.

Use of very small implant areas for HgCdTe photodiode and reliance on the lateral diffusion length of the material to collect photogenerated signal carriers is an interesting potential hardening mitigation approach that also offers increased performance. A small photodiode is used in conjunction with a microlens array, one lens per pixel. The microlens focuses IR photons to a small area in each unit cell. Since the collecting photodiode area is smaller, dark current is smaller. A trade space exists that balances the responsivity and sensitivity performance against operability and proton

fluence performance.

The authors studied HgCdTe detectors fabricated in material responsive to long wavelength infrared (LWIR). The arrays were biased and operational at 40K. A NIEL and Diffusion Length Damage Constant chart was constructed as shown in **Figure 6–3**. The correlation methodology made two assumptions that were validated. The first was that the change in detector performance was due to displacement damage and the change was linear with proton fluence. The second was that lateral collection length and responsivity changes in the detectors have the same energy dependence as NIEL. The measured data at 63 MeV did not exactly correspond to the calculated NIEL. This value would produce a more conservative estimate of the performance change.

Measured data was collected at a proton energy of 12 MeV using a 14 μm implant diameter photodiode pixel. The responsivity decreased $\sim 13\%$ at a high fluence of $6.2 \times 10^{11} \text{ p/cm}^2$ (D_d of $\sim 3.2 \times 10^9 \text{ MeV/g}$ which is

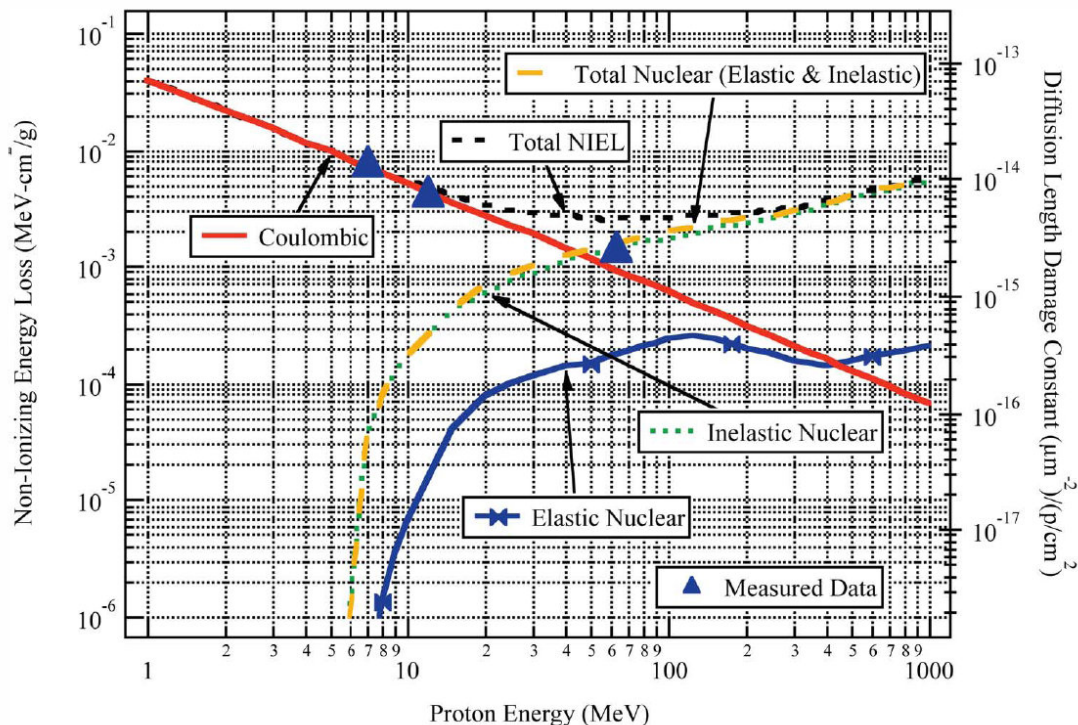


Figure 6–3. Energy dependence of measured lateral diffusion length damage constant on NIEL energy dependence. [From Hubbs *et al.* 2007].

~ 25 x higher than that predicted for Europa). The lateral collection length damage factor was $7.0 \times 10^{-15} \text{ (1/}\mu\text{m)}\text{/(p/cm}^2\text{)}$

The radiation response of the CMOS readout chips which are an integral part of the infrared hybrid focal plane array are expected to be similar to that found in CMOS imagers as discussed previously. In the simplest configuration IR CMOS readouts utilize a source follower per detector amplifier in each unit cell. This is equivalent to the simplest CMOS imager configuration. The major difference is that the IR readout deletes the silicon photodiode and substitutes a HgCdTe photodiode per pixel. The readout pixel and the IR pixel are directly connected via an indium bump. Typical operating temperature for a MWIR HgCdTe hybrid using a CMOS readout is ~ 80K. More advanced readout unit cells are also available using a capacitance transimpedance amplifier per unit cell (CTIA). Readouts and subsequently hybrid focal planes can be hardened using the same radiation hardening by design and/or process as described previously in the CMOS imager section.

6.1.2 Transient Effects

Transient radiation effects occur when an energetic particle (electron or proton) traverses the active signal generating volume of a photodiode detector such as HgCdTe or its corresponding CMOS readout chip and creates an ionization trail thus producing a false signal. HgCdTe material can be viewed as replacing the silicon photodiode in visible CMOS imagers. The underlying readout circuit in many ways is equivalent to the CMOS imager circuits and architecture but minus the silicon photodiode. The most sensitive element is the HgCdTe photodiode which is designed to be very responsive to incident photon signals. Transient particles interact with the sensitive volume of the detector and create additional carriers along their ionizing path. The amount of energy

deposited in the focal plane array is usually small compared to the particle's incident energy. Transient signal effects are not permanent, and the spurious charge is swept out during readout but the additional charge constitutes a source of noise in the image

A key parameter of interest in any sensitive detector is the number of pixels that are compromised or "hit" by a transient energetic particle during an integration time. This is a function of the number of primary hits and also on the number of pixels or the size of the cluster that are compromised due to charge spreading from the primary hit pixel. The rate of primary hits can be calculated from the incident particle flux that arrives behind the shield at the detector array. The total number of hits in a frame of focal plane array data can be found by taking the product of the particle flux behind the shield, the total detector area, and the integration time. For applications that require a very sensitive array, knowledge of the cluster size is also very important. As an example MWIR HgCdTe focal planes for the James Webb Space Telescope (JWST) have a science requirement for an effective read noise of 10 electrons and integration times of up to 1000 seconds.

It is important to note that the notional Europa IR Spectrometer (VIRIS) utilizes a MWIR HgCdTe that operates at 80K as opposed to JWST's 37K and that the nominal read noise of the suggested TMC6604a HgCdTe image sensor is < 100 electrons and integrates for ~ 38 ms to 154 ms as opposed to JWST's requirement of 10 electrons and integration times as long as 1000 seconds. As a consequence, transient effects are still very important to the VIRIS but not nearly as critical as compared to JWST.

Dutton *et al.* performed an energy transfer analysis for silicon and HgCdTe [Dutton *et al.* 1997]. The energy loss per unit length is based on the semiconductor mass, electron densities, ionization energy and the energy of the incident particle. Knowledge of

the material's bandgap is then used to convert loss per unit length to the number of charge particles per unit length, also known as the

Linear Transfer or LET. For compound materials such as HgCdTe the relative compositions of Hg and Cd are considered. The results are plotted in **Figure 6-4** as Energy Loss in keV/ μm as a function of the energy of the incident proton. This plot is for LWIR $\text{Hg}_{.82}\text{Cd}_{.18}\text{Te}$ with a cutoff of $\sim 12\ \mu\text{m}$ although values should be similar for MWIR $\text{Hg}_{.7}\text{Cd}_{.3}\text{Te}$.

LET for HgCdTe layers for protons with 100 MeV of energy is $\sim 3\ \text{keV}/\mu\text{m}$. A constant LET is assumed. Although the IR device is backside illuminated through about $200\ \mu\text{m}$ of a CdZnTe substrate, the substrate does not contribute to the charge generated along the particle track. The CdZnTe substrate is semi insulating and should not generate any charge that would be collected by the IR photodiode. The typical IR absorbing HgCdTe thickness is about $10\ \mu\text{m}$ which implies an energy deposition of $\sim 30\ \text{keV}$. This is only a small fraction of the incident energy which supports the constant LET assumption. In a more recent publication Pickel *et al.* 2005 assumed an LET of $4.0\ \text{keV}/\mu\text{m}$ for 63 MeV protons.

It has been shown [Klein 1968] that the energy required to generate an electron-hole pair, ε , is given by:

$$\varepsilon = (14/5) E_g + r(h\nu_r)$$

where r is treated as an adjustable parameter is between 0.5 and 1.0 eV.

For HgCdTe the pair production number used is $\sim 1.2\ \text{eV}$ [Pickel 2005]. The pair production number routinely used for silicon is 3.6 eV/carrier pair indicating that an energetic particle will produce 3 times as many carrier pairs in HgCdTe as silicon due to bandgap differences. In addition since HgCdTe is more dense than silicon, its Linear Energy Transfer (LET) will be \sim a factor of 2 higher. The average energy of an incident proton that penetrates the Ta shield is expected to be \sim

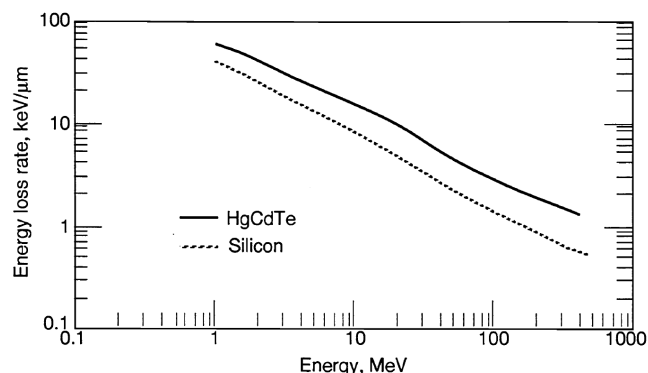


Figure 6-4. Proton stopping power computed using TRIM90. [From Dutton *et al.* 1997]

100 MeV. For a HgCdTe detector of thickness $10\ \mu\text{m}$ the carrier pair production rate for protons is estimated to be $\sim 60,000$ electrons per incident proton. The carrier pair production rate for 10 MeV electrons is estimated to be $\sim 12,000$. [See Section 4.1]

Pickel [Pickel *et al.* 2005] address the issue of transient effects from protons in JWST MWIR HgCdTe detectors. Irradiations were performed using 30 MeV and 63 MeV protons incident at normal, and 45 and 67 degrees off normal. A low flux, typically in the range of 10^3 to $10^5\ \text{p}/\text{cm}^2$ was used to assure the observation of isolated single event transients.

A comparison of their model to measured data is shown in **Figure 6-5** for two energies, 30 MeV and 63 MeV, and two angles, normal or 0 and 67 degrees. The total charge created by one 63 MeV proton incident at normal angle is $\sim 10,000$ electrons. Total charge generation for the 63 MeV protons incident at an angle of 67 degrees off normal is seen to increase by $\sim 3\times$. The higher charge generation is expected since the path length of the proton is now longer since it is traversing the detector in a shallower angle. The total charge generation was found to consist of a central peak charge with small nearest neighbor contributions.

The effects of particle induced transients were also studied by Marshall *et al.* 2003.

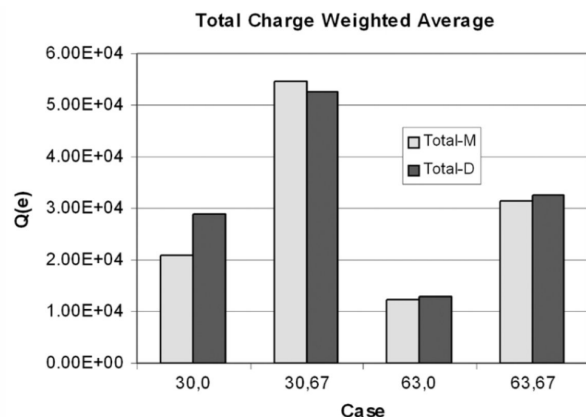


Figure 6-5. Comparison of model and measured data for the total charge distribution created by the path of an incident proton. 30 MeV and 60 MeV cases for 0 or normal incident and 67 degree incident particles are presented. [From Pickel et al. 2005]

The devices were fabricated from LWIR HgCdTe and had cutoff wavelengths of $\sim 11 \mu\text{m}$. Pixel size was $60 \mu\text{m}$ but incorporated a small HgCdTe photodiode of diameter $14 \mu\text{m}$ which was combined with a microlens per unit cell. The function of the microlens was to focus the $60 \mu\text{m}$ of light onto the small $14 \mu\text{m}$ photodiode for charge conversion. The quantum efficiency of the device was $\sim 54\%$ and the array had excellent response uniformity ($\sigma/\text{mean} \sim 4\%$). The device was operated at 40K. Each pixel of the silicon CMOS readout utilized a capacitance transimpedance amplifier (CTIA). Integration times of $\sim 40 \text{ ms}$ were used.

The devices were irradiated with 27 and 63 MeV protons at a 45° incident angle. Figure IR-6 shows the charge histogram measured for $1,000 \text{ p/cm}^2/\text{s}$ for 27 MeV protons. 6,202 hits involved at least one pixel exceeding a 4,000 electron threshold. Above 4,000 electrons the number of events versus total charge declines into a broad peak with a value of $\sim 7 \times 10^4$ electrons which is in good agreement with the estimated peak value for 27 MeV protons incident at 45 degrees onto a $10 \mu\text{m}$ thick layer of HgCdTe.

The 63 MeV proton hits deposited only half as much charge as the 27 MeV protons. The effect of the microlens illumination of a small photodiode is observed while under proton irradiation. The amount of nearest neighbor cross talk is less than 2% for a threshold of 25,000 electrons and increases to 14% for a threshold of only 4,000 electrons. The four side-nearest neighbors are affected while the effect on the corner-nearest neighbors is small. **Figure 6-6** plots the histogram for 63 MeV protons. The effect of the hit on total charge decreases rapidly with the number of pixels affected.

This paper studied the influence of the lateral collection diode on transient charge collection. Small $14 \mu\text{m}$ diameter diodes were fabricated with a pixel pitch of $60 \mu\text{m}$ and a microlens per pixel was used to collect the photons and keep the response of the device high. The small diameter diode collected photogenerated and particle generated charge through its field free region of the detector. The efficiency of this collection depends on

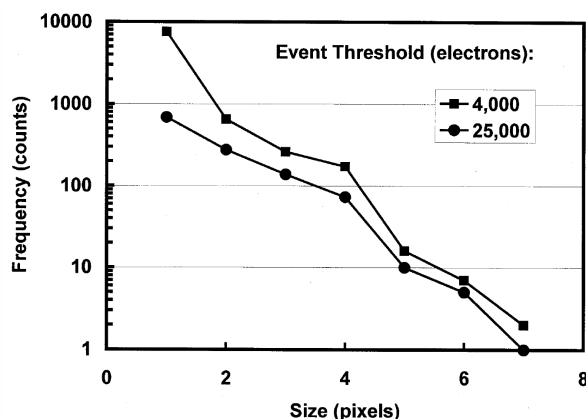


Figure 6-6. Histograms for 63 MeV proton hits as a function of the number of pixels affected. Two thresholds were used to determine each series of points, a threshold of 4,000 electrons and 25,000 electrons. The larger events are restricted to relatively few pixel. Pixel design utilized a micro lens and a small photodiode. Signal and particle induced charge collection occurred by lateral diffusion in HgCdTe to the photodiode. [From Marshall et al. 2003]

the lateral diffusion length of carriers in HgCdTe. The conclusion of the paper is that the lateral collection diodes used in this study present a tremendous advantage to reducing the number of corrupted pixels due to an energetic particle hit.

Finally, the authors performed a separate testing of the readout CMOS silicon integrated circuit chip. This device had a pixel pitch of 60 μm which matched that of the HgCdTe detector. The readout was tested naked, in chip form, not as a hybrid connected to an array of HgCdTe photodiodes. The readout was capable of providing a snapshot mode readout with a frame rate of 100 Hz. The readout utilized a CTIA amplifier per unit cell with on-chip correlated-double-sampling circuit. The CMOS pixels in this device were accessed by a direct X-Y addressing scheme similar to that used for the visible CMOS imagers. This readout had many similarities to the nominal VIRIS readout chip being discussed for Europa. The readout is designed to provide a conversion gain of any input signal of 0.82 $\mu\text{V}/\text{electron}$. The output amplifier was a source follower.

The readout was irradiated with energetic protons in order to discriminate any possible transient response that would occur separate from the HgCdTe photodiode array. The tests yielded no measurable transients even at proton beam currents that were two orders of magnitude higher ($\sim 1 \times 10^5 \text{ p/cm}^2/\text{s}$) than the data analyzed for the hybrid discussed above. Another readout array was also tested separately using the same timing patterns but in an integrate-then-read mode. This device did not show any detectable differences with respect to the cross-talk issue.

Focal plane false signal transients generated by energetic particles need to be considered with respect to the notional visible – infrared spectrometer (VIRIS). Longer exposure times that increase the signal-to-noise ratio for VIRIS are possible through the use of target motion compensation. However these

longer times can also increase the vulnerability to noise induced by background radiation. The flux of particles reaching the HgCdTe detector for different radiation shielding thicknesses can be estimated. With 1 cm of Ta shielding an estimated $3.5 \times 10^6 \text{ particles/cm}^2/\text{sec}$ (at 5 R_j) would reach the detector. Assuming 27 micron pixels and 154 ms exposure time, an estimated 45% of all pixels would be struck by an incident electron during the integration period.

It is estimated that each incident electron will deposit $\sim 12,000$ signal electrons in the HgCdTe detector ($\sim 6\times$ that expected in silicon due to band-gap differences). This level of transients will have a serious impact on the noise of the device. Consequently in order to acquire useable image frames additional radiation shielding will be required for the VIRIS detectors. With 2 cm of Ta shielding approximately 20% of VIRIS pixels would be struck during a 154 ms exposure. With 3 cm of Ta shielding, that rate is reduced to approximately 5%. For the notional VIRIS, a 3 cm tantalum shield is assumed and at this level of shielding the mission dose-depth curve predicts $\sim 10 \text{ krad}$ of total dose received by the VIRIS detectors.

6.1.3 Mitigation Techniques

HgCdTe Detector Arrays

Modern HgCdTe detector arrays appear to be hardened against TID through the use of a CdTe passivation technique that reduces passivation layer charging and generation of interface states during irradiation. In addition dark current, whether created by TID or displacement damage is suppressed as a consequence of nominal operation at 80K.

In general, reducing the collecting volume of a sensor subject to radiation improves performance by reducing the amount of material that can be damaged by the energetic particle or by generating an ionizing charge track as the particle transverses the HgCdTe material. HgCdTe thicknesses of ~ 10

μm are required in order to absorb the incident IR radiation with high efficiency. Consequently only device area changes will affect the interaction volume.

In the previous Section the advantages of using a lateral collection diode scheme were presented. This architecture used a very small implant area to create a small area IR photodiode that is less than the desired pixel pitch. Normally this would result in reduced sensitivity or quantum efficiency. The pixel was designed to take advantage of the lateral diffusion length in HgCdTe to collect absorbed charges from the larger field free region. This approach was combined with a micro lens per unit cell to concentrate photon normally falling on the larger pixel pitch optical area to that of the smaller photodiode. This approach keeps the sensitivity up in the device but reduces the dark current since the dark current is directly proportional to the area of the photodiode. This architecture also assisted in improving the transient response by reducing charge sharing or cross talk that is generate by the ionizing particle track. Engineering signal-to-noise tradeoffs exist that depend on pixel pitch, photodiode area and lateral diffusion lengths.

A more radical approach would be to construct a small area HgCdTe photodiode that is reticulated or nearly separated from its neighbors. The active volume of HgCdTe would be reduced via a etch technique. A micro lens would then be required to focus an optical cross section equal to the detector pitch onto the small photodiode. The reduced HgCdTe material volume would result in a reduced transient particle response while the microlens would be used to concentrate the IR photons into the sensitive photodiode area.

CMOS Readout Devices

Since CMOS readout chips commonly used in IR focal plane array are also based on single crystal silicon material many of the mitigation approaches suggested for visible CCDs and CMOS imagers will be similar.

These include increasing the shielding, choice of device architecture, reducing active region volumes to decrease displacement damage generated dark current and decrease response to transient events. The architecture of the readout should include the capability of varying biases during the lifetime of the readout to accommodate any accumulated offsets. Thin oxides can reduce flatband voltage shifts due to ionizing radiation and can be very effective when used with flexible biasing to further mitigate any threshold shifts.

Dark current and leakage currents in the readout are significantly reduced by cooling since these currents have the same exponential dependence on inverse temperature as other silicon based devices.

Three key approaches for hardening CMOS which were mentioned previously are: 1) radiation hardness by design, 2) use of a radiation hardened foundry process and 3) more recently, use of new process variations in modern submicron fabrication processes to mitigate radiation effects. Radiation hardening by design requires increased silicon real estate, however CMOS readouts have a little more breathing room in this respect as compared to visible CMOS imagers, since each readout pixel does not need a silicon photodiode for photon conversion. Unfortunately there are only a few radiation-hardened foundries, they have longer turn around times, reduced process stabilities and larger feature sizes. The combinational approach which melds radiation hardening by design with key process changes in new submicron processes appears to be more ideal.

Also periodic heating (annealing) could be implemented. Annealing at higher temperature, even to room temperature and perhaps to $\sim 100^\circ\text{C}$, should anneal out trap centers and improve performance and reduce leakage current may be effective.

Data processing software can be utilized to discriminate against transient events and permanent dark current spikes. Techniques

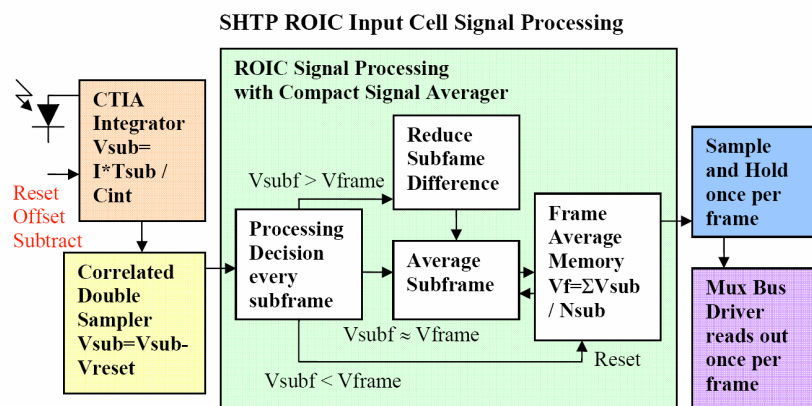


Figure 6–7. Functional block diagram of the Sensor Hardeing Technology Program (SHTP) readout input cell signal processor.
[From Hariston et al. 2006]

include subframe data sampling, thresholding and dropping bad pixels and good pixel averaging. This approach will require additional off chip processing and favors CMOS readout designs that allow storage in the unit cell such as the CTIA design. IR vendors report fabricated designs with signal processing features that include subframe averaging, spatial filtering, temporal filtering, random transient event suppression, motion detection, and edge enhancement.

Subframe data sampling involves dividing the frame integration time into a number of smaller integration times and then processing this subframe data to generate an output. This processing results in the suppression of temporal artifacts, such as charge pulses due to gamma or particle irradiation. Low noise subframe averaging and optical pulse suppression were demonstrated at appropriate integration times and irradiances.

A CMOS silicon readout chip was fabricated using the BAE radiation hard 0.8 μm process available at their Manassas facility. A functional block diagram for this readout's input unit cell is shown in **Figure 6–7**. Gamma suppression is done in the input cell. Each subframe consists of the following operations, Reset, Signal Integration,

Correlated Double Sampling and Signal Averaging. The Signal Averaging circuit compares the incoming subframe with the previous frame average to decide which of the three operations to perform: reset, average or suppress [Hariston et al. 2006].

Pulse suppression was found to be a function of pulse height. A pulse suppression of 50 was measured for a 0.7 V pulse height and was 3.3 for a 50

mV pulse for the readout device utilized. If a significantly higher new subframe is compared to the frame memory, the difference between the new subframe and the memory is reduced before averaging, thus implementing the gamma noise suppression. If a new lower subframe is found much less than the previous frame average, the frame average is set to the new subframe value. This instance occurs only if the first subframe is contaminated, if most of the subframes are contaminated, or if a prompt pulse were to upset the frame memory. Measured pulse suppression of a factor of 50 was demonstrated.

6.1.4 Planetary Protection

Planetary protection concerns would ideally be met through dry heat sterilization of VIRIS although survivability of the HgCdTe detector elements using the currently defined JEO planetary protection protocol is in question. However, a new bake-stable process is under development which produces HgCdTe focal plane arrays that can be baked at 90° to 100°C for extended periods or 110°C for 24 hours. While this proprietary process has not yet been applied to the science grade devices typically used for planetary space missions, it is thought that the bake-stable process can be applied to any HgCdTe focal plane array

[Beletic 2008]. A risk reduction effort to fully quantify the performance impact of high-temperature bake-out on HgCdTe detector elements at the temperatures called for by the JEO planetary protection protocol is recommended. Subsequent to dry heat sterilization of VIRIS, a one-time opening telescope door with bio-barrier seals is employed to prevent recontamination.

6.1.5 Overall Assessment

In general very limited data exist in literature that addresses the radiation hardness of modern HgCdTe focal plane arrays. Much of this data is held as proprietary by the IR vendors. Existing data and common agreement among the focal plane vendors indicate that MWIR focal plane arrays can be hardened to TID levels well in excess of those required for Europa. Europa assumptions are that the devices are behind a 1 cm Ta shield and receive ~ 70 krad(Si) with RDF = 2. Published data on separate HgCdTe detectors passivated with CdTe indicate hardness in excess of 1 Mrad(Si).

Recent data from JWST using an MWIR focal plane similar to the notional IR imager mentioned for VIRIS indicated that the main effect of exposing the focal plane to 5 krad(Si) was an increase in the dark current distribution at the higher dark current tail. JWST, however, operates its MWIR focal plane at 37K (as opposed to ~ 80 K for VIRIS) and is concerned with levels of noise starting around 10 electrons. Dark currents at this temperature were measured in fractions of electrons per second and the “hot” pixel tail observed after the irradiation was still less than 1 electron/second. These are values well below those specified for the notional VIRIS instrument. In addition the 5krad (Si) was acquired through an irradiation of the device with 63 MeV, so displacement damage was also a factor.

A bare potential JWST CMOS silicon readout chip (H1RG from Teledyne) that used

a simple source follower per detector amplifier exhibited essentially no radiation damage to 50 krad(Si). This total dose was produced by bombarding the readout using 63 MeV protons.

Additional experiments were reported on very long wavelength HgCdTe detectors fabricated for the Cross-track Infrared Sounder with an ~ 15 μm cutoff at 78K. These detectors did not exhibit degradation thresholds, as indicated by their resistance-area products, until ~ 3 to 4x of the displacement damage doses from protons predicted for the VIRIS focal plane behind 1 cm Ta.

An $\sim 13\%$ responsivity decrease was observed in HgCdTe detectors after a displacement damage dose of 3.2×10^9 MeV/g which is a factor of ~ 10 x higher than that predicted for Europa behind the 1 cm Ta shield. These were LWIR detectors that were operated at 40K.

It is important to note that all of the reported radiation response data for HgCdTe is a consequence of gamma or proton bombardment. No data was found for irradiations by energetic electrons, which are present in high numbers behind the estimated Ta shield.

The main concern for HgCdTe focal planes in a radiation environment is that of transients.

The notional MWIR focal plane has a 640 x 480 format with 27 μm pixels. The total area of the device is ~ 2.24 cm^2 . It is estimated that there will be ~ 1000 protons/ cm^2/s incident on the focal plane behind the 1 cm Ta shield. Using a nominal 100 ms integration time we find there would be ~ 224 “hits” per frame (0.073 % of the total number of pixels). Each proton would produce enough false signal carriers to corrupt the pixel or pixels traversed. This appears to be small image degradation.

However, it is predicted that for the JEO mission at 5 R_j , 3.5×10^6 electrons/ cm^2/s will

impact the same focal plane array. Each of these impacts is estimated to produce ~ 12,000 carrier pairs in the HgCdTe material (about 6x of that predicted for silicon material).

Assuming a worst case integration time of 154 ms, increasing the thickness further to 3 cm would result in corruption of 5% of the pixels. The increase shielding thickness has a positive outcome of reducing the TID to ~ 10 krad(Si).

Overall, radiation effects will produce a small increase in dark current of IR focal plane arrays which, if a concern, can be reduced by cooling below 80K for MWIR devices. Some decrease in sensitivity, as measured by quantum efficiency, may be experienced but this effect should be $\leq 13\%$ at the worst case of 10x the expected displacement dose damage. Generally the IR vendors agree that their FPAs can be radiation hardened to total doses exceeding the calculated TID expected for Europa behind a 1 cm Ta shield (~ 70 krad(Si)). The vendors also agree that some combination of radiation hardening by design and by foundry will definitely result in the hardness of the silicon CMOS readout devices in excess of the 70 krad(Si) mentioned above.

The major issue for the Europa mission appears to be transient response. Since MWIR HgCdTe has a much smaller bandgap than silicon its carrier pair production rate for energetic particles is expected to be a factor of six higher than silicon. The HgCdTe detectors are sensitive to both IR photons and to charged particle intersections. Consequently, in order to avoid data corruption across a large percentage of the focal plane by incident electrons, the Ta shield thickness should be increased to ~ 3 cm.

The above discussion assumes the utilization of an off-the-self IR focal plane array. IR vendors have indicated they can utilize special detector designs such as the lateral collection diode discussed in the Transient Radiation Section to further reduce the effect of transients. In addition, as discussed previously, transient reduction

signal processing circuits can be used that would further suppress transient pulse heights by a factor of 50 or more depending on original pulse heights.

6.2 Thermal Detector Arrays

Thermal detectors are a class of detectors that include thermistor bolometers, pyroelectric detectors, and thermopiles. These devices operate with a fundamentally different detection mechanism from that of quantum or photon detectors. Incoming photons, rather than exciting carriers across a semiconductor bandgap, heat a thermally isolated absorbing structure. The resulting heat rise is sensed by a process that differs between the different types of detectors in this class. Thermistor bolometers sense the resistance change of a thermistor element on the absorber, pyroelectric detectors measure a polarization change in a pyroelectric material, and thermopiles measure the temperature difference between the absorber and a heat sink (substrate) using thermocouples. The thermal detection mechanism typically provides a lower figure of merit parameter (called Detectivity (D^*)) than can be obtained by quantum detectors. However, thermal detectors are not limited to certain spectral response regions by their bandgaps as is HgCdTe. Thermal detectors are only limited in wavelength by their absorbing structure.

Thermal detectors are often used in two types of applications: those that involve longer wavelengths and higher operating temperatures than are accessible to quantum detectors, and those that require flat spectral response over a broad wavelength range. Space science applications offer a broad range of thermal detector applications. Planetary and astronomical targets often have spectral and thermal signals well beyond the typical capabilities of HgCdTe. (The notional Thermal Instrument (TI) for the baseline JEO mission would require response in six different spectral bands ranging from 8 μm to 100 μm). While

often required to detect long wavelengths, space-based instruments are uncooled whenever possible to reduce mass, size, and cost with increased reliability. In addition, radiation balance measurements of planetary bodies often require flat spectral response [Foote and Jones 1998, Foote et al. 1998, Foote et al. 2002, Foote et al. 2003].

A thermopile consists of several series-connected thermocouples running from a heat sink (substrate) to a thermally isolated infrared absorbing structure. Incident infrared radiation creates a temperature difference between the absorber and substrate, which generates a voltage across the thermopile. The thermopile voltage is proportional to the incident radiant power in excess of the radiant ambient. Thermopiles offer the advantage of operating without temperature stabilization or with greatly reduced stabilization requirements. Thermopiles offer the additional features of negligible $1/f$ noise and high linearity, characteristics that are lacking in some bolometers. The advantages of thermopiles over resistive bolometers for an instrument include 1) reduced or no temperature stabilization requirements, 2) no electrical bias required, 3) no bridge needed, 4) high linearity, and 5) no excess film ($1/f$) noise.

Thermopiles have the ability to produce accurate radiometry thus making them ideal for many space science instruments. Thermopile detector arrays require the combination of three key ingredients— 1) thermoelectric thin films with high figure of merit, 2) arrays of well thermally isolated structures, and 3) low-noise readout circuitry.

The devices use two dissimilar metals to generate the thermal voltage, they are BiTe and BiSbTe. These metallic layers are $\sim 1 \mu\text{m}$ thick. Each unit cell or detector contains 12 thermocouples composed of $3 \mu\text{m}$ lines with $3 \mu\text{m}$ spacing. These layers are deposited onto thin films of silicon nitride and silicon dioxide atop bulk silicon. Linear thermopile arrays are fabricated using bulk silicon micromachining,

in which the silicon substrate is etched from under the detectors to provide good thermal isolation. The entire structure is coated with gold black to act the incident photon absorbing layer. This process is appropriate for single pixels and linear arrays. Specific detectivity (D^*) values of $1\text{--}2 \times 10^9 \text{ cm Hz}^{1/2}/\text{W}$ in vacuum have been routinely achieved for several different detector geometries using this process.

The Mars Climate Sounder consumes 10 W and consists of nine 21-element thermopile linear arrays. They are uncooled and broadband. Signal readout is accomplished by separate CMOS application specific integrated circuit (ASIC) electronics that are packaged at the focal plane but separate from the detector arrays. Thus radiation hardness will depend on the hardness of both the thermopile arrays and the readout electronics.

6.2.1 Total Dose and Displacement Damage Survivability

Total Ionizing Dose

Several thermopile detectors were exposed to radiation from Co^{60} up to 10 Mrad(Si). The total ionizing dose was applied in steps. The resistivity and responsivity of the uncooled devices were measured at each step. Control samples were also utilized. The devices exhibited little change from their pre irradiation performance over the course of the irradiations. A few percent change in both responsivity and in device resistance was observed up to 10 Mrad. Some limited scatter in both the control and irradiated samples was seen and is attributed to the difficulty in reproducing the responsivity measurements on the 0.5% level. Most of the change in responsivity occurred during the first exposure implying that some radiation-induced aging of the gold black absorbing layer [Foote 2000].

The separate silicon CMOS readout circuits were not characterized for TID, displacement damage or transient response. It

is expected that these devices would behave in the same manner as any modern silicon CMOS circuit device under irradiation as discussed previously in this report.

Displacement Damage

The devices were not characterized with incident electrons or protons. However, it is speculated that the active elements of the thermopiles are the two thin ($\sim 1 \mu\text{m}$ each) metallic layers of BiTe and BiSbTe, are hardened against displacement damage. The active elements are very thin, metallic in nature and do not significantly depend on crystallinity.

6.2.2 Transient Response

Thermopiles depend on temperature differences between the two thin electrodes. The device utilizes a gold black absorber layer to absorb the infrared energies of the incident photons and alter the temperature of the device. The gold black layer is approximately $30 \mu\text{m}$ thick but has a very low density which equates to about a $1,000 \text{ \AA}$ of gold. The thickness of each of the BiTe and BiSbTe layers are ~ 1 micron. Incident particles will traverse these very thin layers and deposit energy along their tracks.

The following is an estimate of the impact of energetic electrons and protons on the noise obtained from thermopile focal plane arrays. The focal planes consist of silicon CMOS arrays packaged side-by-side with the thermopile detector arrays. The harsh external environment for the baseline JEO mission would require some shielding to reduce the radiation effects. The detector arrays were found to be hard to $> 10 \text{ Mrad}$, however, the CMOS readouts are not. Assuming CMOS readouts can be hardened to $\sim 400 \text{ krad}$ ($\text{RDF} = 2$), then a 0.3 cm Ta shield would be suitable.

At $5 R_j$ approximately 3×10^7 electrons/ cm^2/sec would penetrate the 0.3 cm Ta shield with an average energy of $\sim 3 \text{ MeV}$.

There would be $\sim 3.9 \times 10^4$ protons/ cm^2/sec also penetrating the shield with an average energy of $\sim 50 \text{ MeV}$.

This treatment assumes a previously determined detector heat capacity of 1×10^{-7} joules/Kelvin, a detector response of 3.6 mV/K , and a detector noise of 140 nV . Each pixel is $240 \mu\text{m} \times 480 \mu\text{m}$ in area and the focal plane is operated at an integration time of 128 milliseconds. The thermopile detectors are assumed to be $2 \mu\text{m}$ thick.

Each electron and proton is found to deposit $\sim 3.2 \times 10^{-16}$ joules and 9.6×10^{-16} joules of energy, respectively, as they transverse detector. The electron and the proton generate $\sim 1.2 \text{E} \times 10^{-11}$ and 9.6×10^{-11} volts of noise, respectively. At $5 R_j$ the total number of particles hitting the detector area in an integration time is $\sim 4,424$ electrons and 6 protons. The noise generated from these electron and proton "hits" is $5.3 \times 10^{-8} \text{ V}$ and $2.2 \times 10^{-10} \text{ V}$ respectively. Detector noise was previously estimated to be 140 nV or $1.4 \times 10^{-7} \text{ V}$. The detector noise is seen to dominate the total noise when this noise is compared to the noise produced by transient electrons and protons. Both energetic transient electrons and protons appear to have no real impact to the noise of the thermopile detectors.

6.2.3 Mitigation Techniques

The thermopile arrays appear inherently hardened against TID and energetic particles. Displacement damage effects also appear to be minimal based on the fact that the thermocouples are thin and do not rely on the crystallinity of the material as in the case of the semiconductor photon detector.

The thermopile arrays depend on CMOS readout circuits in close proximity. All the hardening techniques previously discussed in both the visible CMOS and infrared readout Sections would apply. The key approaches relate to hardening of the CMOS circuits by design and by process.

6.2.4 Planetary Protection

Planetary protection concerns would be met through dry heat microbial sterilization of the micro thermopile arrays. The materials utilized in the fabrication of the devices, silicon, silicon nitride, BiTe, and BiSbTe should be able to withstand the 100 to 125 °C sterilization bake. The stability of the gold black absorption coating under long term bake at 125 °C will need to be addressed via experiments. The stability of mounting adhesives will also need to be investigated.

These circuits would be similar to any modern circuit fabricated using submicron silicon CMOS process. Radiation hardness by design and foundry would be key approaches for the design and fabrication of the readout devices.

6.2.5 Overall Assessment

Thermopile linear arrays are being considered for the baseline Europa mission. Each linear array consists of 21 detectors with a pixel size of 240 μm x 480 μm . The thermopile arrays detect signal through conversion of incident photons into temperature. The minute change in temperature is converted to a small voltage signal using very thin electrodes consisting of BiTe and BiSbTe. The signals are amplified by separate CMOS silicon circuits.

The total dose response of these devices was characterized up to 10 Mrad(Si). Little change in resistivity of the devices or their responsivities was observed. No particle irradiation tests were performed. However, given the thinness of the detecting materials and the fact that the materials are metallic like, it is estimated that displacement damage will have little to no effect.

The response of these devices to transient protons and electrons was addressed through simple calculations. Incident particle energies were converted to temperature changes that would be experienced by the thermopile detectors and found to be insignificant when compared to their estimated signals. The thermopile detectors are extremely thin and appear hardened against transients.

The radiation hardness of the separate silicon CMOS readout circuits was not tested.

7 Avalanche Photodiodes

An avalanche photo-detector is a typical detector choice for space-borne laser altimeters. APDs consist of a PIN-like structure with the addition of a high field region where impact ionization multiplication takes place. This process is in itself noisy so that gains of the order of 100 usually lead to the best system noise level. These detectors can be used in two different modes; either moderate gain of order 100, just below the breakdown voltage, or in so-called Geiger mode just above the breakdown voltage. Geiger mode refers to higher field operation, leading to a breakdown in the diode from which recovery only follows after reduction of the bias voltage. In this case single photons give large output pulses making optical detection straightforward. APDs are available in Si and various narrower band gap materials such as Ge and InGaAs to allow operation further into the infrared than 1 to 1.1 microns.

7.1 Radiation Environment and Effects on APDs

The Jovian radiation environment presents several challenges to the use of APDs. Generally speaking, silicon APDs will have the same radiation induced changes as any other photodiode, with total dose and displacement damage leading to increased dark current while incident electrons and protons produce transient effects. Using the current JEO radiation design point for a 105-day Europa science tour (see Section 3), the respective TID and DDD requirements for APDs are 70 krad(Si) and $1.3\text{E}8$ MeV/g(Si) assuming 1 cm Ta shielding and including a Radiation Design Factor (RDF) of 2. A significant fraction of this exposure, approximately half, would occur while in orbit around Europa while the bulk of the remainder occurs during the Jovian tour phase of the mission. There are several sources of transient noise that can impact APD performance in the Jovian environment:

Electron flux creates background noise within the APD, which is of the same order as the noise level of the APD itself. The size of the electron pulse in the APD for a single incident electron is in the 1000 to 2000 electron range. This electron pulse is amplified by the APD gain to generate an output pulse; for example a gain of 100 produces an output of 100k to 200k signal electrons per incident electron. This is likely to be above any threshold level used for detection in a typical application such as a laser altimeter receiver.

Proton flux will produce larger signals per event than electron flux, well above practical instrument thresholds, in the range 10k to 100k electrons per incident proton prior to gain within the APD.

Cherenkov and luminescence photons are created as charged particles pass through the materials of the instrument optical train. This is expected to create a relatively uniform blue background at the APD. This level should be well below the sensitivity level of the APD, which will also be further protected by a narrow band spectral filter.

Bremsstrahlung photons are generated as high-energy electrons decelerate in shielding and structure materials, but only a small fraction of these incident photons will interact with the active region of the APD. Bremsstrahlung photons are most significant because of their contribution to secondary electron production as they continue to pass through instrument materials and shielding. These secondary electrons form the majority of the total electron flux at the APD level behind a thick radiation shield.

7.2 APD detector survivability

An increase in dark current due to gamma and proton irradiation is the lifetime limiting factor for APDs. In some cases the increase in dark current can be accommodated by instrument electronic adjustments or cooling of the APD.

Silicon APDs

Becker [Becker *et al.* 2003] provided data on 51 MeV protons, and gamma irradiation of several silicon APDs from three manufacturers. They found dark current increases of a factor of 10 to 100 at a dose of 10^{12} protons/cm² with little recovery in annealing. They found no difference between biased and unbiased dose, and used a fixed bias corresponding to an initial gain of 100. Subsequent to dosing, the flat field response was down by a factor of 2 to 4, which recovered with annealing to 25 to 33 % down. A greater loss of sensitivity was found in a thick depletion device intended to have greater sensitivity at 1064 nm. Operating at fixed bias they were unable to separate gain change effects from unity gain responsivity effects.

Gamma irradiation produced little effect on dark current at less than 10 to 50 krad but after that dark current increased more rapidly than the power law effect found for protons, so that the dark currents were almost equal after 300 krad gammas and after 10^{12} protons/cm². In the case of gammas, annealing at 100 °C for 1 hour reduces dark current by about a factor of 2.

In general, APDs are very robust to radiation provided that the increased dark current can be accommodated. A thicker depletion layer to improve efficiency near the long wave cutoff leads to greater radiation sensitivity.

InGaAs and Ge APDs

InGaAs and Ge APDs make suitable detectors for wavelengths as long as 1.7 microns. Becker [Becker and Johnston 2004]

evaluated examples of these diodes after exposure to 63 MeV protons at levels up to 10^{12} protons/cm² and after exposure to gamma rays up to 270 krad. The dose was usually administered with the diodes biased for gain=10, but the authors found insignificant differences compared to unbiased irradiated samples. For proton exposure, the dark currents rose about 10 fold for Ge and as much as 10^4 for one low dark current InGaAs diode. Since InGaAs starts off with a lower dark current than Ge this means that after large doses there is less difference between the devices. The Ge device can be annealed to some extent while annealing has little effect on InGaAs after 1 month at room temperature. For gamma ray exposure the dark current increases are smaller at 10 to 100-fold at 270 krad. This paper does not mention responsivity so it is not clear whether tests were made.

Geiger mode (photon counting)

Becker [Becker *et al.* 2007] made measurements on silicon and InGaAs/InAlAs detectors of modern design intended for photon counting applications. They found severe degradation in performance with high dark current and reduced output at doses as low as 6×10^{10} protons/cm² with 51 MeV protons and after 5 krad of gamma irradiation. This prevented useful operation even at low temperatures. In the absence of new designs, photon counting APDs do not seem useable for the baseline JEO mission.

7.3 Transient effects

Transient effects on APDs are similar to those on silicon detectors in general. An incident electron is estimated to generate 1000 to 2000 signal electrons and an incident proton is estimated to generate 10k to 100k signal electrons, both figures being prior to the gain applied to the APD. The rates at which these events occur are a function of the external radiation flux, the instrument specific radiation shielding and the size (collecting area) of the

detector.. The impact of these events on a particular instrument is determined by instrument design details, but is primarily driven by exposure time or its equivalent in that instrument.

Electron flux creates background noise in the APD, which is of the same order as the noise level of the APD. Depending on the details of the design, this may be mitigated simply by increasing the threshold for pulse detection. However pulse sizes as large as 10 times the noise level are likely, so that these events will probably be registered as signals rather than increased noise.

Using the JEO environment specified in Section 3, an APD shielded with 1 cm of Ta would receive $4.3\text{E}5$ incident electrons per square cm per second while in orbit at Europa (9 Rj). For a typical APD active area of 0.5-mm^2 this results in 2150 transient events per second due to electron flux. For a laser altimeter in a 225 km orbit at Europa (the high end of the suggested range for this study), total time for the return of a laser pulse is ~ 1.5 ms. During this time, an average of ~ 3 incident electrons will cause transient events in the laser altimeter receiver APD. Range-gating, which is routine in laser altimeters, with a window of $150\text{ }\mu\text{s}$ (corresponding to an altitude range of ~ 12 km) reduces the transient rate to $\sim 1/3$ of laser firings. To reduce the transient rate to a more workable level requires additional mitigation, for example additional radiation shielding or shorter duration range-gates. An increase to 3 cm of Ta shielding reduces incident electron flux $\sim 9\text{X}$ resulting in a transient rate of $\sim 3\%$ of laser firings. During Io flybys (5 Rj), electron flux is $\sim 8\text{X}$ that at Europa requiring addition mitigate to avoid degraded instrument operation.

Proton flux will produce much larger signals per event than those generated by electron flux, well above practical thresholding levels, but the proton flux reaching the APD while in orbit at Europa behind 1 cm of Ta shielding is just 50 protons per cm^2 per

second. The probability of such an event in a 0.5 sq mm detector during a range-gate of $150\text{ }\mu\text{s}$ is less than 0.01%. During Io flybys, proton flux is $\sim 18\text{X}$ that at Europa which raises the probability of an APD transient event to $\sim 0.1\%$ per laser firing. No further mitigation beyond 1 cm of Ta shielding should be needed to mitigate transients due to proton flux.

7.4 Planetary Protection

APDs are based on standard PIN diodes and in silicon will have the same temperature limitations as other devices. With suitable packaging, prolonged exposure to $125\text{ }^\circ\text{C}$ should be acceptable. Narrower bandgap materials such as InGaAs may be more temperature sensitive, so manufacturers should be consulted. This would also be the case for thermoelectric cooled devices if they were chosen.

7.5 Overall Assessment

APDs are relatively robust in a radiation environment when used with moderate gains in the 10 to 100 range. The main lifetime limiting effect is an increase in dark current, which can in principle be recovered by cooling. They will normally be used at relatively large bandwidths at which the dark current should not be a limiting factor.

The output transient from a single electron or proton hit will normally be well above the electronics noise threshold, so that each event will produce a spurious signal. The effect of these signals must be considered in the instrument design, and will drive the choice of radiation shielding thickness and in the case of a laser altimeter will drive some instrument operational parameters such as range-gating. Devices used in Geiger mode for photon counting have severe radiation induced changes at doses as low as 5 krad gamma and 6×10^{10} protons/ cm^2 and can not be recommended for use on JEO.

8 Photomultipliers and Microchannel Plates

Photomultipliers (MPTs) and microchannel plates (MCPs) are closely related devices that rely on secondary electron multiplication to produce electron gain in a vacuum. The electron multiplication can be as high as 10^7 to 10^8 so that the pulse produced by a single photoelectron can be detected reliably. Lower gains can be used to increase the average current produced by a flow of photoelectrons to an easily measured current. These devices can be used in a variety of instruments including imagers, energetic particle detectors, plasma detectors and mass spectrometers. Some photomultipliers contain microchannel plates but most rely on discrete dynodes.

8.1 Total Dose Survivability

In a photosensitive application (visible, UV or X-ray), a photocathode ejects one (or more for X-rays) photoelectron into the vacuum with a probability of order 10 % (the quantum efficiency). The photoelectron undergoes secondary electron multiplication at a series of discrete dynodes (PMT) or a continuous high resistance tube (MCP). These actions are unaffected by radiation induced damage because dislocations and even bulk impurities have little effect on photoemission or secondary electron efficiency. Radiation damage does not affect the performance of a PMT or MCP except for radiation darkening of the vacuum window or such high fluences that the tube is aged.

In an MCP the electron multiplication occurs in a glass tube with the inside formed to have relatively good secondary emission, and the glass has sufficient conductivity to provide a voltage gradient at intermediate regions of the tube between the electrically biased ends. These tubes, roughly 10 to 20 μm in diameter, are assembled into large bundles or plates of 10 to 70 mm diameter which thus contain millions of spatially distinct channels. This gives spatial resolving abilities which the

discrete dynode PMT does not have. Additionally the tubes are quite short, of order 1 mm, so that devices are compact and fast, which is why they are sometimes used even in PMTs.

The continuous nature of the 'dynodes' in an MCP leads to a broader distribution of output pulses per incident electron, *i.e.* a broad pulse height distribution (PHD). This is normally compensated by the highly resistive nature of the glass in the tubes, which causes a large pulse of 10^5 to 10^6 electrons to disturb the potential distribution in the tube. This causes the pulse size to saturate, narrowing the PHD. This means that an individual tube has to recover its resting potential distribution with a relaxation time of about 1 ms. There are so many tubes in an MCP that only at very high inputs is there much probability of an input electron entering a disturbed channel before it can recover. So for both these devices the properties depend largely on the surface, specifically the work function of the surface, of the multiplier, and are robust to irradiation.

Each MCP event that initiates electron multiplication, including those due to background radiation, contributes to the total current drawn from the device during its lifetime. MCPs exhibit a gradual reduction of gain as charge is drawn, and it is typical to "scrub" the devices past the more rapid gain changes seen early in life. It is believed that the gain reduction does not fully stabilize but approaches a limiting value only at infinite current draw. The stability of the gain is therefore dependent on the extent of the initial scrubbing. Levels of current draw of 1 to 10 coulombs per cm^2 are considered usable for MCPs and these correspond to a fluence of order $1\text{E}13$ inputs (optical, radiation, etc.) that produce secondary multiplication assuming operation at $1\text{E}6$ gain. PMTs have a more open dynode structure which usually has a more stable, cleaner surface and a lifetime of 100 coulombs per cm^2 is typically quoted.

8.2 Transient effects

Incoming radiation, both electrons and protons, can cause emission from the photocathode and from the dynodes or MCPs. Even if the pulse generated by incident radiation produces several electrons the pulse will not damage the tube, and only one count (event) will be registered by the instrument. After the first few dynodes, or well down the MCP tubes, electron multiplication is limited and the electron shower produced will be too small to be counted by the instrument. This effect limits the areas producing transient count effects to the photocathode, usually near the surface, and the dynodes or MCP very close to the surface.

While ground-based testing of MCPs using high-energy electron and proton beams at normal incidence indicates that 30 % of incident electrons and 70 % of incident protons produce output pulses, flight data from Galileo instruments suggest a substantially lower MCP efficiency for omni directional radiation and relatively thick radiation shielding. The Galileo Energetic Particle Detector (EPD) recorded an average of 33E3 counts per second due to background radiation during 8 Europa flybys on its “start” MCP (start MCP raw singles rate telemetry channel) with ~0.3 cm Ta radiation shielding and 1.54 cm² active area. The 33E3 counts per cm² per second recorded by the EPD MCP is ~1% of the combined 2.7E6 electrons per cm² per second and 2.1E3 protons per cm² per second expected at 9 Rj behind 0.3 cm of Ta shielding. The Galileo UltraViolet Spectrometer (UVS) recorded 1.8E3 counts per second due to background radiation at Europa on an MCP with 28-mm² active area. While the exact amount of UVS MCP radiation shielding is not known to the DWG, the 6.4E3 counts per cm² per second recorded by the UVS MCP is <0.5% of the incident radiation flux expected at 9 Rj behind 0.3 cm of Ta shielding and ~1.5% of the incident radiation flux behind 1 cm of Ta shielding.

Transient effects on instruments employing MCPs and PMTs are a function of the level of radiation shielding (incident flux), the active area of the device (collecting area), the integration time if applicable, and the efficiency of the device in converting incident radiation to an output pulse registered by the instrument (on order of 1% based on Galileo data). These parameters present a relatively large trade-space for instrument designers employing these devices.

8.3 Planetary Protection

MCPs are made of a type of glass, and are normally vacuum baked to at least 200 °C for some time. The photocathodes have varying temperature sensitivities but CsI and CsTe or RbTe should all be capable of the temperatures needed for JEO planetary protection protocols. Visible cathodes containing Cs would not be suitable. The most temperature sensitive part in a vacuum sealed MCP assembly is the seal itself, with some designs being unable to survive to 100 °C. However devices capable of 110°C survive are readily available and devices with even higher seal temperatures have been made.

8.4 Overall Assessment

These detectors will most commonly be used in photon counting mode and will count radiation hits as well as photons. Some mitigation may be possible on the basis of pulse height, but without this individual electron or proton events should be treated as background rate events.

The devices themselves, their cathodes, dynodes and MCPs are all very robust and should suffer no damage from radiation. The effect of the radiation background on tube ageing (its contribution to total tube current) should be included in lifetime calculations. The only part likely to be damaged by high temperature is the vacuum seal in a sealed tube.

9 Lasers and Laser-Related Components

A laser altimeter has three main components: the transmitter, the optical receiver, and the analog electronics. **Figure 9-1** shows the configuration used by the NEAR Laser Rangefinder [Cole 1998]. In this assessment, only the radiation susceptibility of the transmitter is considered.

The transmitter sub-components of interest to this assessment are the diode-laser-pumped Cr:Nd:YAG Q-switched solid-state laser system and the fiber-optic delay assembly (FODA). A 809-nm diode laser is used to pump the 1.064- μm Cr:Nd:YAG lasing medium and is Q-switched for pulsed mode using LiNbO_3 . Calibration of the time-of-flight counters is accomplished by the FODA, which transmits a portion of the Q-switched laser output to the receiver for the purpose of measuring elapsed time between the initial laser firing and the optical backscatter. In the following sections, the radiation susceptibility of each of these key components—diode laser, Nd:YAG lasing medium, LiNbO_3 crystal, and fiber optics—will be discussed.

9.1 GaAs Diode Pump Laser

Modern quantum-well (QW) laser technologies are less susceptible to radiation damage than their older heterojunction counterparts due largely to fabrication

advances and shrinking dimensions of the active layers. Because of these advances, modern semiconductor lasers show overall a reduction in internal loss mechanisms, a decrease in threshold current densities, and an increase in slope efficiencies [Johnston and Miyahira 2003, Johnston 2001, Evans et al. 1993]. The primary concern for radiation effects on semiconductor lasers is due to displacement damage that produces recombination centers [Sporea 2004]. There are two laser diode characteristics that are of primary concern—the current threshold for lasing and the quantum efficiency of the output (optical power output divided by the injection current).

Figure 9-2 shows the effect of increasing fluence of 5.5 MeV proton irradiation on a 808-nm strained InGaAs QW laser [Johnston 2003, Evans et al. 1999]. This laser structure similar to that used to pump the Cr:Nd:YAG media in the NEAR LA, except that additional indium has added to red shift the laser output to 980 nm. The data in **Figure 9-2** shows the threshold current of the laser increases with increasing proton fluence. Others have reported similar more-or-less linear increases of the threshold current with fluence [Zhao et al. 1997]. Note that the quantum efficiency of the laser, as measured by the slope of the line, remains unchanged except at very high fluences.

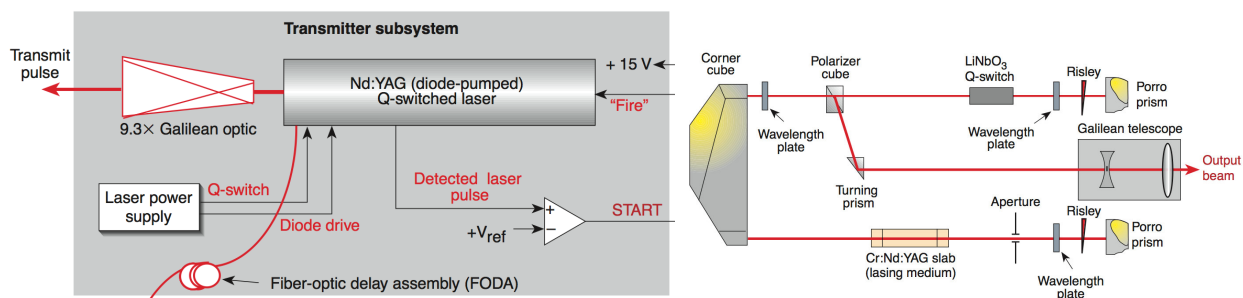


Figure 9-1. Diagrams of the NEAR Laser Altimeter subsystems discussed in this assessment. Left-hand diagram is the Transmitter subsystem and the right-hand diagram is the Nd:YAG laser cavity. The components under consideration in this assessment are the pump laser diode, the Nd:YAG Q-switched laser, and the fiber optics. [From Cole 1998]

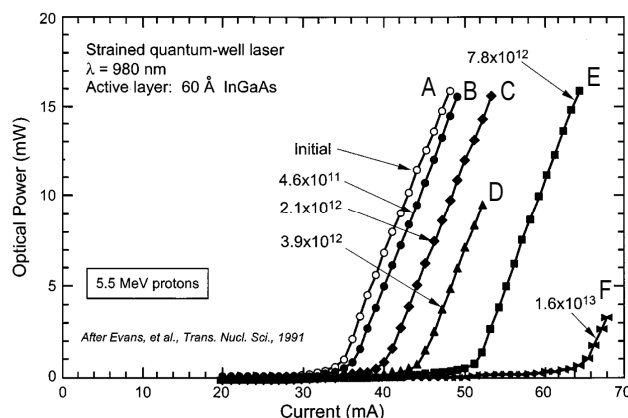


Figure 9–2. A plot of optical output power (mW) versus current (mA) after irradiation with 5.5 MeV of protons with the specified particle fluence. The DDD for each curve can be calculated to be (A) 0 MeV/g, (B) 5.5×10^9 MeV/g, (C) 2.5×10^{10} MeV/g, (D) 4.7×10^{10} MeV/g, (E) 9.4×10^{10} MeV/g, (F) 1.9×10^{11} MeV/g. [From Evans et al. 1993, Johnston 2001]

The data demonstrates that QW laser structures are quite resistant to displacement damage effects. The proton fluence levels in **Figure 9–2** can be converted to a displacement damage dose by using the non-ionizing energy loss (NIEL) value of 1.2×10^{-2} MeVcm²g⁻¹ for 5.5 MeV protons in GaAs [Summers and Walters 1993]. After a displacement damage dose of 5.5×10^9 MeV/g (Si), there has been a minor 6% shift of the lasing threshold current (**Figure 9–2**, curve B), which can be accommodated straightforwardly with electronic adjustments. Thus, nominal Ta shield thickness of 0.3 cm is recommended, which places a requirement for tolerance $\geq 1.3 \times 10^9$ MeV/g (Si), including a RDF of 2.

9.2 Nd:YAG Crystal

Nd:YAG (Neodymium-doped yttrium aluminum garnet or Nd:Y₃Al₅O₁₂) is the crystal used for the lasing medium for solid-state lasers.

The important concern for a Nd:YAG crystal is photodarkening due to displacement damage and ionization damage. Nd:YAG crystals exposed to ⁶⁰Co gamma rays and high-energy 30–50 MeV protons show a reduced optical output when pumped near 800 nm, largely attributed to absorption of the laser emission at 1.064 μ m by defect centers in the crystal [Rose et al. 1995]. Crystals were exposed up to 600 krad, but most of the damage occurred within the first 50 krad and manifested itself as ~20% decrease in power conversion efficiency. For proton fluence levels up to 10^{12} /cm², the authors concluded that the performance loss was comparable to that observed after gamma irradiation and due to the generation of ionization centers rather than lattice disruption.

Doping the Nd:YAG with 1% Cr⁺³ was shown to improve the radiation hardening of the material. No loss of performance with pulsed pumping could be observed after exposure of a Cr:Nd:YAG to 500 krad (Si) or by an additional exposure to 5×10^{11} cm⁻² fluence of 50-MeV protons, as shown in **Figure 9–3**. Without Cr⁺³ doping, these same authors observed that with irradiation doses of 100 krad (Si), lead to a decrease in the Nd:YAG power conversion efficiency, but only for the case of continuous pumping. For pulsed pumping, the power conversion efficiency remained unchanged.

Contrary to the results by Rose [Rose et al. 1995], Kacmarek [Kacmarek 1999] reported that ⁶⁰Co gamma irradiation of Nd:YAG crystals reduces the power conversion efficiency even for the case of pulsed pumping. The author seems to attribute the difference to the different thermal equilibrium reached within their respective experiments. Kacmarek did not investigate Cr-doped Nd:YAG.

The use of Cr-doped Nd:YAG is assumed for the notional instrument and because radiation testing of the Cr:Nd:YAG crystal by Rose was limited to 500 krad, a Ta shield

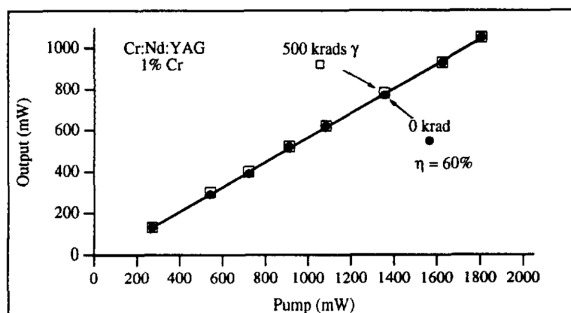


Figure 9-3: Performance of a pulse-pumped 1% Cr-doped Nd:YAG before and after irradiation with 500 krad gamma irradiation. [From Rose *et al.* 1995]

thickness of 0.3 cm is recommended. This shield thickness places a requirement for part tolerance ≥ 400 krad (Si), comfortably below the test limit of Rose [Rose *et al.*]. The NIEL for Nd:YAG crystals is not known and therefore the DDD tolerance cannot be directly compared.

9.3 LiNbO₃ Q-switching Component

The optical modulator in the solid-state laser is made from single crystal LiNbO₃. The main concerns of damage to this component would be significant variations in its electro-optic properties and photodarkening due to

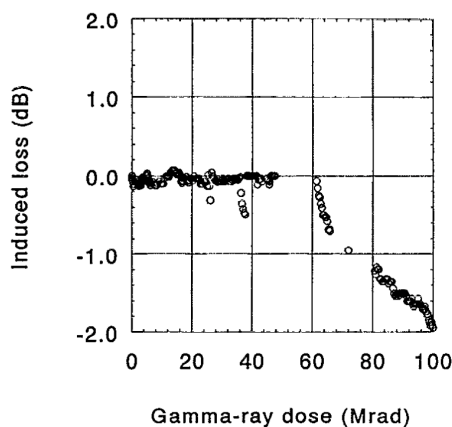


Figure 9-4: A plot of radiation induced insertion loss of a LiNbO₃ optical modulator, used in a Mach-Zehnder configuration, as a function of Gamma-radiation dose. [From Tsang and Radeka 1995]

ionization effects and/or displacement damage. Tsang and Radeka 1995, studied optical modulators using single-crystal LiNbO₃ with Ti in-diffused waveguide structures in a Mach-Zehnder configuration. After a total dose of 100 Mrad from a ⁶⁰Co γ -ray source, the insertion loss was approximately 2dB. Below 50 Mrad, the insertion loss was less than 0.2dB ($< 2\%$), as shown in Figure 9-4. The findings of this paper demonstrate that the electro-optic property of the single crystal LiNbO₃ is negligibly affected by γ -radiation up to 50 Mrad. Additional data discussing the effect of electron or proton flux on the functionality of LiNbO₃ as an optical modulator could not be found.

Given the tolerance of this component to total dose up to 50 Mrad, we do not consider LiNbO₃ to present any significant risk in the JEO environment.

9.4 Optical Fibers

The main concern for radiation effects on optical fibers is photodarkening and embrittlement. There is an extensive amount of work that details the effect of gamma radiation on graded index (GI), Ge-doped pure SiO₂ single mode fibers [Morita and Kawakami 1989, Griscom 1995, Berghmans *et al.* 2008, Henschel *et al.* 2006]. These papers report that the color centers that are formed as a result of irradiation predominantly absorb in the UV and visible wavelength regions with tailing absorption in the infrared. Figure 9-5 shows a plot of radiation-induced attenuation (RIA) versus wavelength [Berghmans *et al.* 2008] for several optical fibers. A variety of single mode pure silica core fibers show a RIA value of less than 0.1 dB/m at 1064 nm after a TID of 10⁶ Gy (SiO₂), which is 100 Mrad (SiO₂). The different traces of this figure indicate that regardless of high OH or low OH content, the optical fiber has negligible loss at this wavelength. In general, at 1064nm, the maximum loss will be less than 0.5 dB/m.

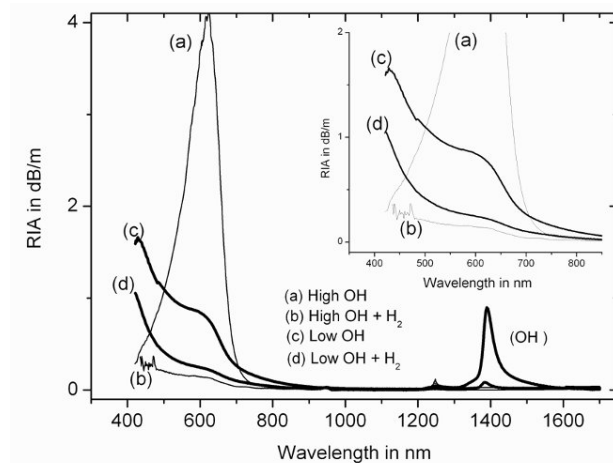


Figure 9-5: A plot of radiation induced attenuation (RIA) versus wavelength pure silica core optical fibers with (a) high OH, (b) high OH + H₂, (c), and (d). The inset is a close-up figure of the four traces in a wavelength range of 350nm–850nm. [From Berghmans et al. 2008]

In regards to the effect of radiation on the fiber strength, it has been found that within a TID of 10⁶ Gy (SiO₂), which is 100 Mrad (SiO₂), the optical fiber can be expected to have greater than 95% of the preirradiated strength when protected with acrylate, silicone + acrylate or polyimide coatings, whereas when protected with fluorinated polymer, the tensile strength was reduced to less than 40% of their preirradiated strength after a TID of 0.1 MGy [Yashima 1982]. Additionally, Henschel et al. 2006 reports that gamma radiation effects of pure SiO₂ single mode fibers were found to have an increase in breaking stress, *i.e.* become stronger when irradiated with less than or equal to 100 Mrad (SiO₂). In excess of this dose, the strength of the fiber will decrease. In general, the tensile strength will be at least 95% of its preirradiated value to a TID of 10⁶ Gy (SiO₂).

The energy deposited per gram of material depends upon the density of the material. The conversion factor of 1 rad (Si) =

0.58 rad (SiO₂) is typically used [Claeys and Simoen 2002]. Thus, the 100 Mrad (SiO₂) dose level used in the discussion above corresponds to ~170 Mrad (Si).

9.5 Transient Effects

There are no transient effects that could be identified for the lasers and laser-related components discussed in this section.

9.6 Planetary Protection

The individual components of the transmitter system are tolerant to elevated temperatures and are expected to easily tolerate the dry heat microbial reduction protocol for planetary protection.

9.7 Overall Assessment

The laser and laser-related components central to the transmitter system for the notional laser altimeter are relatively robust towards radiation. No transient noise effects could be identified for any of the components, thus making the issue of total dose survivability the driving issue for the selection of shield thickness.

From a radiation perspective, the weakest links within the transmitter subsystem are the Nd:YAG crystal and the pump laser diode. Nd:YAG has been tested only up to 500 krad (Si) with gamma irradiation and 5 x 10¹¹ cm⁻² fluence of 50-MeV protons. Although no decrease in Nd:YAG performance was observed after irradiation, it is prudent to place this component behind a nominal shield of 0.3 Ta until additional testing at higher doses can be done. The pump laser diode shows a 6% shift of the laser threshold current after a DDD of 5.5 x 10⁹ MeV/g (Si). Placing the laser diode pump behind a nominal shield thickness of 0.3 cm brings the DDD exposure within the acceptable design requirement.

In summary, to ensure the total dose survivability (TID and DDD) for the diode laser and Nd:YAG crystal, a nominal shield

thickness of 0.3-cm Ta is recommended. A shield thickness of 0.3 cm Ta places a requirement for part tolerance ≥ 400 krad (Si) and $\geq 1.3 \times 10^9$ MeV/g (Si). The pump laser diode and Nd:YAG crystal comfortably meet this requirement. The LiNbO₃ and optical fibers can tolerate significantly more, but it is not practical to separate these components within the transmitter subsystem.

10 Stellar Reference Unit

10.1 System Overview

The JEO Stellar Reference Unit (SRU) would provide the spacecraft with an absolute reference to inertial space. The 3-axis stabilization of the spacecraft would require the SRU to act as a staring mode tracker, measuring stars in potentially any direction. Star scenes will typically move slowly relative to the SRU field of view (FOV), and the SRU would be required to measure stars as dim as magnitude 5 or 6 (dependent on its FOV) to give full sky coverage. Attitude knowledge would be provided by processing a combination of SRU and inertial measurement unit (IMU) measurements. It is assumed that a high accuracy IMU such as the Scalable Space Inertial Reference Unit (SSIRU) would be available to assist in the attitude measurement function at all times. Although the SRU will be required to function during JOI, the Jovian Science Tour, EOI, and Europa science, the tightest pointing requirement would be for HGA pointing, requiring the HGA boresight to be pointed to within an angle of 1 mrad of Earth, 3 sigma (radial accuracy), of which a TBD subset would be allocated to the SRU/IMU subsystem.

The SRU would have two key modes --- initialization (acquisition) mode to solve the lost in space problem by identifying stars without a priori attitude information, and tracking mode where the expected star positions on the SRU focal plane are already very well known due to attitude propagation. Expected characteristics for the SRU are a 15 to 22 degree diameter FOV, and a silicon CCD or CMOS focal plane array for imaging. A typical magnitude 5 star (the dimmest needed) should produce at least 30,000 signal electrons per second (expected exposures are from 0.1 to 0.4 seconds), with the star signal concentrated in a 7x7 pixel (or smaller) centroiding area. SRU accuracy in two axes is derived from star position measurements. Accuracy in the third

axis is determined by a combination of star separation and position accuracy.

10.2 Radiation Environment and Effects on SRU

JEO's radiation environment presents several challenges to meeting SRU performance requirements, and a combination of hardware, algorithm, and system strategies will need to be used to reduce the impact of cumulative and transient radiation effects on the SRU. JPL has had extensive prior experience with radiation mitigation strategies for SRUs in the Jovian environment, as the result of work performed with several SRU vendors for NASA's Juno New Frontiers Mission and the Europa Orbiter SRU Concept Design Study of 1999-2000. In both the Europa Orbiter and Juno SRU study phases, shielding analysis has played a major role, not only in determining what is needed for SRU survival, but also how much additional shielding (and mass) is needed to reduce the production of transient noise and false stars from electron and proton flux. Based on these previous studies, a shielding level of 3 inches equivalent aluminum spherical shell thickness (achieved through a combination of existing SRU body materials and additional mass choices) is considered a realistic regime for the notional JEO SRU focal plane array in order to minimize cumulative degradation effects from total ionizing dose (TID) and displacement damage dose (DDD), and transient noise from particle and photon flux. The following discussion assumes this level of shielding for the notional JEO SRU focal plane array.

Using the current JEO Radiation Design Point for a 105-day Europa science tour (see §3), the respective TID and DDD requirements for the JEO SRU focal plane array are 70 krad(Si) and 1.3E8 MeV/g(Si), which includes a Radiation Design Factor (RDF) of 2. A significant fraction of these exposures occur during Europa science. Only 1/2 of the TID and DDD is experienced prior to EOI. Note

that cumulative dose requirements may change for the SRU FPA with any future trajectory and mission trades.

There are several sources of transient noise that can impact SRU performance in the Jovian environment:

Electron flux creates background noise in the SRU FPA image, which can reduce the number of useable dim stars in the FOV, and decrease the accuracy of bright star measurements. For typical silicon FPA active region volumes, each incident electron may be expected to create a signal on the order of several thousand electrons per pixel on average [Becker et al. 2005, Liebe 2001]. Transient signal distributions will depend on the instantaneous electron spectrum through the specific SRU shielding mass, and each electron hit will typically affect more than one pixel, the geometry of which will depend on incident angle, energy, scattering, and pixel diffusion effects. External integral 30-MeV electron fluxes may be used to estimate the number of electron hits that will reach the SRU FPA through the shielding mass considered here. This FPA hit rate would be as high as $3\text{E}6$ electrons/cm²·s during Jupiter Orbit Insertion at 5Rj. However, during Europa science, where SRU performance requirements are tightest, electron flux would be smaller. For example, at 9Rj (Europa's approximate distance from Jupiter), electron fluxes vary considerably with respect to Jupiter latitude, ranging from $4.28\text{E}5$ electrons/cm²·s at latitude 0 to only 100 electrons/cm²·s at latitude 30 [Insoo 2008]. Additional reductions of up to a factor of three are expected in Europa orbit due to various effects related to the presence of the body itself [Paranicas et al. 2007].

Proton flux at the SRU FPA level can be similarly estimated by considering external integral 100-MeV proton flux levels. This flux would be approximately 900 protons/cm²·s during JOI at 5 Rj and many off the shelf trackers can already handle hundreds of proton

events per frame. During Europa science, this flux would be reduced to only 50 protons/cm²·s. Proton transients can be both detected and “filtered” by looking for signal non-repeatability over several measurements. They are not expected to be a significant source of “false star” signal error for this application.

Cherenkov and luminescence photons are created as charged particles pass through the media of the SRU optical train. This is expected to create a relatively uniform blue background at the FPA plane. Previous SRU studies have addressed these phenomena in detail, and their background noise contributions are considered to be relatively minor compared to stray light. As these wavelengths also tend to be outside of the useable spectra of most SRUs, mitigation by the addition of short wavelength optical cutoff filters is also possible.

Bremsstrahlung photons are generated as high-energy electrons decelerate in SRU materials, however only a small fraction of these incident photons will interact with the pixel active regions of the FPA [Liebe 2001]. Bremsstrahlung photons are most significant because of their contribution to secondary electron production as they continue to pass through SRU material and shielding. These secondary electrons form the majority of the total electron flux at the FPA level in heavily shielded SRUs.

10.3 SRU detector survivability

10.3.1 SRU Detector Technologies and Associated Radiation Effects

Most existing SRU products are based on n-channel CCD or CMOS active pixel sensor (APS) sensor technologies. JEO TID and DDD requirements may be prohibitively challenging for many n-channel CCD-based SRUs because the following radiation degradation effects may become quite severe by 70 krad(Si) and $1.3\text{E}8$ MeV/g:

TID: increased surface dark current and flatband voltage shifts

DDD: decreased charge transfer efficiency, increased bulk dark current, and the creation of “hot pixels”

While p-channel CCDs have higher resistance to charge transfer efficiency losses due to the absence of phosphorous dopant in the buried channel (responsible for the phosphorous-vacancy center, the prime CTE-degrading defect center in n-channel CCDs), a viable p-channel CCD SRU would require custom development, including fabrication with relatively rare epitaxial silicon to reduce the active volume sensitive to transient signal generation.

CMOS FPAs benefit from pixel readout processes which do not require charge transfer over multiple pixel volumes as in CCDs. This not only makes CMOS sensors immune to DDD-induced charge transfer efficiency degradation, but also allows for faster overall signal sampling due to the direct access of pixels. This is especially valuable during tracking modes where only small sub-arrays, or “tracking windows,” need to be accessed because it reduces the amount of time that genuine star signal is vulnerable to corruption from particle and photon transient noise. CMOS sensors are susceptible to the following radiation effects, although many can be mitigated or eliminated by design.

TID: increased leakage current, degradation of on-chip analog-to-digital convertor (ADC) functionality, increased temporal noise, increased dark signal and photo-response non-uniformities, increased dark current, shifts in offsets, fixed pattern noise, reduced amplifier gain and responsivity

DDD: increased temporal noise and dark current, increased dark signal non-uniformities, creation of “hot pixels,” increased fixed pattern noise, changes in responsivity

Single Event Effects in on-chip support CMOS circuitry (e.g. single event latchup in on-chip ADC)

10.3.2 Existing SRU Product Examples

The HAS (High Accuracy Sensor) is the latest generation radiation hardened CMOS APS star tracker sensor product to be produced by Cypress/FillFactory, Belgium. It is a 1024x1024 pixel APS with an on-chip 12-bit ADC [Blarrie *et al.* 2005]. ESA has sponsored an extensive space qualification process for the HAS, including radiation testing to TID levels that are very close to, and DDD levels that are well in excess of, JEO requirements (the formal release of ESA’s HAS qualification report is expected in Summer 2008).

Radiation testing of the HAS was also performed by EADS SODERN for the Juno SRU study phase in 2007. SODERN’s Juno testing was performed with flight wafer lot samples under expected SRU flight conditions, and included irradiation with spectrally-representative electrons to incremental TID levels up to and including 34.4 krad(Si) and DDD levels up to and including 1.1E8 MeV/g(Si). Additional TID testing with Co-60 was performed to 36 krad(Si), the results of which were consistent with those seen during the electron testing. All the TID and DDD-sensitive parameters listed above were characterized, and with the exception of offset shifts and increases in dark current, no significant parametric shifts were observed at any tested radiation level. In addition, the observed changes in offset and dark signal were small enough to have no significant impact on SRU performance for the Juno application.

Several SRU vendors have developed CMOS APS-based SRUs, targeting the lower mass, power, and cost of this architecture compared to CCD-based SRUs. For example, the HAS is the APS used in SODERN’s “HYDRA,” an SRU with a separate optical head and electronics unit, radiation hardened

lens elements, and configuration options that use from 1 to 5 optical heads per SRU [HYDRA brochure]. Hydra's space qualification will be complete in 2008, with the first flight models delivered in 2009. The HAS is also the focal plane array in Selex-Galileo's APS-based Autonomous Star Tracker (AA-STR). The AA-STR was developed for ESA's Bepi Colombo mission, and designed to tolerate the extreme solar flare proton flux environment of Mercury. The AA-STR is currently completing its ground qualification for the AlphaBus GEO Telecommunications platform. A "Flight Demonstration Model" of the AA-STR was integrated in the Proba 2 spacecraft in 2007 and will fly during 2009 [AA-STR brochure]. There are clear options for survivable SRU detector technologies for JEO. The extent to which a given cumulative DDD or TID will affect star signal degradation and SRU performance will be driven by a combination of SRU system features: optical design (i.e. star signal size for a given integration time), the observable sensor parameter degradation under the SRU's specific JEO operational conditions (e.g. FPA temperature), image collection strategies (e.g. readout timing and integration time), operational modes, and image processing techniques.

10.4 Transient Mitigation Approaches

10.4.1 Expected Transient Noise Contribution

Determination of the impact of transient effects on star measurements requires analysis of the probabilities that transient hits will affect star measurements, and the associated accuracy reductions. For simplicity, it is assumed that the star positions on the FPA are known well enough by using gyro based attitude propagation (to within less than 0.5 degrees) that track windows can be placed about the stars and centroid calculations performed (attitude initialization is also discussed below). Analysis of star detection and identification probability is a later activity,

which will follow related trades at the system level that identify the overall pointing strategy.

Measurement accuracy for a typical star tracker configuration is influenced by algorithm choices, star signal, and the transient signals. The following analysis assumes a FPA pixel size of 18 microns (a typical pixel size for current SRUs), which yields approximately 300,000 pixels per cm^2 . Since star images are spread over several pixels, a minimum region of about 7×7 pixels is needed to make a star measurement (Figure 10–1). A 7×7 pixel area is therefore roughly $1/6000 \text{ cm}^2$.

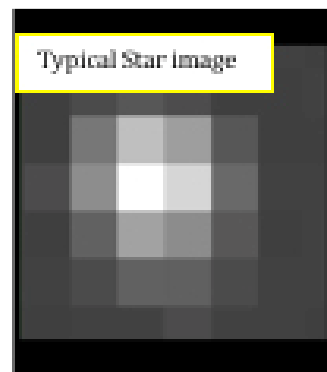


Figure 10–1. Typical star image as seen over a 7x7-pixel track window.

While a proton hit near a star could make the measurement useless, a proton hit can be discriminated based on the size of the generated signal. Therefore, the number of measurements eliminated by protons should be relatively small given good a priori knowledge (about 1/10 during JOI and $<1/100$ at Europa). For initialization, additional proton filtering is expected to be required. Electrons contribute smaller false signal (perhaps 1000 to 2000 electrons per affected pixel per hit), but are much more numerous than protons. The relatively smaller generated signal from electrons can make filtering over many measurements a possible approach. Because of the spatial randomness of the electron strikes, electrons will theoretically produce a flat "white out" effect over many measurements, producing a relatively uniform

Table 10–1: Expected Electron Flux at SRU FPA during Europa Science

latitude 0 (9Rj)*	4.28E5 e/sec·cm ² (Europa's orbit is at 0 degrees latitude with respect to Jupiter)
latitude 15 (9Rj)	1.00E5 e/sec·cm ²
latitude 30 (9Rj)	1.04E2 e/sec·cm ² (latitude 30 is within the “keep out zone” for >25-MeV electrons)

(*)During times when the body of Europa is present for shielding, a factor of 3 reduction in flux may be seen [Paranicas et al. 2007]

background. The dimmest star that can be tracked will depend on the number of hits per second that will hit the “track window.”

Europa Science at 9Rj is used as bounding case for electron flux through 3 inches of equivalent aluminum shielding. The external 30-MeV integral electron flux is used to estimate the electron hit rate at the FPA (see [Table 10–1](#)).

For JOI, the electron fluxes shown in [Table 10–2](#) are assumed.

At 5Rj, approximately 600 electrons will hit the 7x7 pixel area around a star image per second, adding a transient signal of about 600,000 to 1,200,000 electrons per second to the 7x7 pixel star signal. Compared to the collection rate of the dimmest star required (30,000 electrons/second for a magnitude 5 star), the star signal will be effectively invisible, and no measurement is likely. For a magnitude 2.5 star, with a star signal of 300,000 electrons/second, taking account of the spatial randomness of the transient electrons and averaging over multiple samples can possibly provide valid, but noisy measurements. However, availability of very good a priori knowledge will be necessary. A magnitude 1 star (only 16 are available in the sky) produces more than 1.2 million signal electrons, and should be detectable given 0.5 degree knowledge.

At 9Rj, the electron transient hit rate drops to roughly 71 impinging electrons per second (a factor of 8 reduction), and a transient signal contribution of less than 140,000 electrons/second spread over a 7x7 window. The following plot ([Figure 10–2](#)) shows calculated centroid accuracy as a function of star magnitude and electron flux. A 500 ms integration time was assumed for star signal and transient exposure. In order for a star of a given magnitude to be considered useable, at least 1/3 of 100 attempted measurements had to be repeatable at a given electron flux. At 9 Rj, magnitude 4 to 4.5 stars should be trackable without the use of special processing on pixel data, such as frame-to-frame pixel comparison. During the 1.5 hours preceding JOI, the spacecraft will be between 5.5 and 5 Rj. Availability of magnitude 3 stars will be required to maintain tracking. Gyro error over 1.5 hours is estimated at 5.8 mrad (3 sigma/ per axis).

10.4.2 Algorithmic Mitigation Approaches for Initialization and Acquisition

On most spacecraft with good gyros, the lost-in-space problem must only be solved after launch and certain faults, or after very long star outages. Identification can be planned using only bright stars, or bright stars and knowledge of the sun location (this approach is used on Cassini and most star

Table 10–2: Expected Electron Flux at SRU FPA during JOI

5Rj	3.45E6 e/sec·cm ²
6Rj	1.42E6 e/sec·cm ² (latitude dependence is also expected at this location)

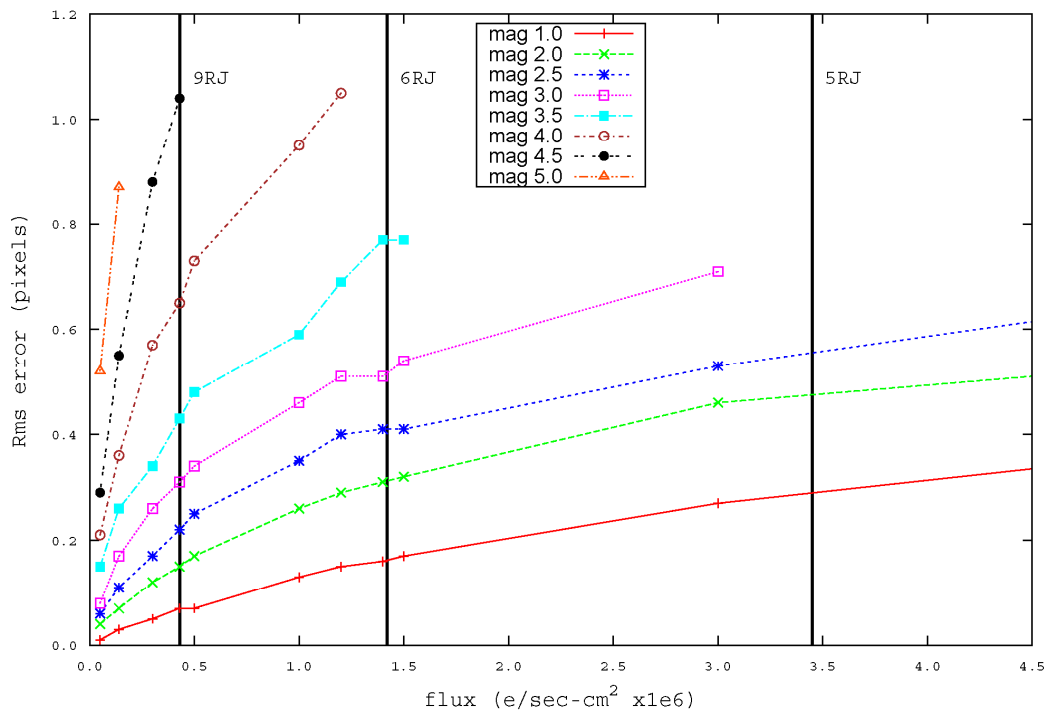


Figure 10–2. Analysis of centroiding error as a function of star magnitude and electron flux. Flux was applied randomly to a 7x7-pixel tracking window with a fixed star image position. A fixed star position was used in this analysis, based on the assumption that estimates of star positions will be accurate enough from gyro propagation to be able to expect less than 1 mrad error in track window positioning. If more than 1/3 of 100 attempted star measurements returned a >1.25-pixel error, the star was considered unusable under the given electron flux level.

scanners on spinning spacecraft). Only mission critical events such as JOI have less flexibility, and if JOI occurs at 5 Rj with extremely high transient levels, the entire JOI sequence may need to be performed on gyros, or on sun-line hold, or with the star tracker pointing at bright stars.

10.4.3 System-Level Mitigation Approach for Tracking on Approach to JOI

Given the potential flexibility of the roll axis direction during JOI, it is likely that tracking can be maintained by orienting the SRU FOV so that magnitude 3 or brighter stars are available. While the particular roll axis

direction for JOI has not yet been evaluated for all-sky pointing, 63 percent of orientations will have at least one magnitude 3 star or brighter star in the SRU FOV, and 32 percent would have at least 2 magnitude 3 or brighter stars (assuming a 20 degree diameter circular FOV).

10.4.4 Algorithmic Mitigation Approaches for Tracking

In the tracking mode, star locations can be propagated accurately over short periods (perhaps periods > 1 hr). Advertised SSIRU IMU gyro bias stability is less (better) than 0.0003 degrees/hour. Including effects of rate random walk error, gyro propagation error

would be 3 mrad in 2 hour (3 sigma/per axis; based on spec sheet values). For the star trackers under consideration, about 3-to-6-pixel error would accumulate after an hour when IMU propagation is used to seed the predicted star location. SRU algorithms can easily compensate for errors of this size without having to go through re-initialization.

10.4.5 Hardware Mitigation Approaches (associated trades)

1. Add shielding to reduce transient hit rate (adds mass)
2. Increase size of optical aperture to increase star signal rates (adds mass, complexity, and perhaps additional Cherenkov radiation)
3. Choose FPA that can be sampled rapidly to help filter transients (increases noise, possibly requires new FPA design)
4. Choose smaller sized pixels to reduce probability of hits (complicates optics, possibly reduces efficiency and full well of detector pixels)
5. Choose FPA that is very “thin” to transients to reduce signal contribution from electrons/protons (possibly requires new FPA, may reduce sensitivity to light)

JPL’s previous experience with the 1999 Europa Orbiter and 2007 Juno SRU study phases has included theoretical and experimental study of Jovian transient effects and mitigation strategies. This work has been performed both internally, and with several prominent SRU vendors (Ball Aerospace, SODERN, and Selex-Galileo). Strategies to improve SRU performance in the presence of electron fluxes as high as $1\text{E}6$ to $1\text{E}7$ electrons/cm²·s have been studied, and included a combination of strategic operational condition choices, shielding, and algorithmic and hardware strategies to reduce the impact of transients and cumulative detector radiation effects.

10.6 Planetary Protection

JEO’s baseline approaches for meeting planetary protection sterilization requirements are 1) dry heat sterilization at 125C for 50 hours for qualification and 115C for 50 hours for acceptance testing, 2) analysis proving that a sterilizing ionizing dose of 7 Mrad(Si) has been reached at all points internal to the SRU by the time of EOI, or 3) unit assembly and test under sterile conditions through ATLO. Dry heat sterilization is viewed as the most practical approach, considering the logistical difficulty of assembly and test under sterile conditions, and the inability of most SRU EEE parts to withstand an ionizing dose of 7 Mrad(Si).

Many existing SRU designs may contain thermal-electric coolers, adhesives, or optical coating processes that will not withstand JEO dry heat sterilization requirements. It is also likely that candidate SRU products may not have been qualified at the assembly level to temperatures as high as those required to achieve dry heat sterilization. Possible optical alignment changes or deformations will need to be investigated early, and may need to be mitigated by a more complex combination of surface and dry heat sterilization techniques during assembly, or by using calibrations to compensate for alignment changes. Although solutions are likely to be achieved with some modification of existing SRU designs and/or a combination of sterilization techniques during assembly, early RFI and study phase activities are recommended to specifically address JEO’s planetary protection sterilization requirements and the degree of redesign and associated cost that would be required to comply.

10.7 Overall Assessment

The radiation and planetary protection challenges facing a JEO SRU are understood. The question of detector survivability is not considered to be a risk issue, provided an appropriate amount of mass may be allocated

to reduce cumulative TID and DDD, as well as instantaneous electron and proton flux. While transient mitigation strategies for similar environments have been extensively investigated on other programs, the hardware and software solutions still need to be implemented for the JEO environment.

It is recommended that early Phase A activities include the release of a Request For Information (RFI) to several SRU vendors, requesting technical and cost input for solutions to meet JEO's rigorous planetary protection, radiation, and SRU performance requirements. A competed study phase with a limited number of candidate vendors is also recommended to allow selection following preliminary SRU design activity, and assessment of potential SRU solutions and radiation mitigation strategies. This will allow a more informed cost versus risk trade, based on a detailed understanding of potential operational modes, algorithmic mitigation approaches for transient noise, SRU performance analyses, and any recommended special operation conditions (e.g. low temperature detector operation for cumulative radiation degradation mitigation). The study phase may also include radiation testing if it is needed to fill knowledge gaps for previously un-tested flight conditions. JPL oversight and independent assessment of study phase results is also recommended.

11 Feasibility of the JEO Notional Payload Detectors

The goal of the DWG was to assess the detector technologies required for the JEO notional payload and determine if a viable pathway exists for acceptable detector performance given the JEO radiation and planetary protection environment. The DWG relied upon publicly available radiation literature and test results, as summarized in the preceding sections, to arrive at their findings. No new detector technology advances were assumed—and, as much as possible, only detectors derived from those with existing flight heritage were considered.

Overall, the DWG concludes that the challenges facing JEO detectors from radiation and planetary protection protocol are understood. Total dose survivability and transient noise impacts are not a high risk issue, providing appropriate shielding mass is allocated and combined with other well known mitigation strategies.

11.1 Science Detectors

The detectors selected for this assessment are derived from the notional payload specified by the international NASA/ESA JSDT. There is no intent in this report to imply that these notional detectors represent the only solution space for these instruments or that these instruments represent the only solution space for meeting the JEO science requirements. They serve to show by existence proof that there is a feasible pathway to meeting the JEO science requirements as specified by the JSDT.

In general, there is a significant trade space available to the instrument provider to balance risk, performance, and science return. Many mitigation strategies for each of the detector technologies have been discussed in the preceding sections and they broadly include shielding, detector design, detector operating parameters, algorithmic techniques, and system-level implementation. The JEO

notional payload represents a single design approach among many that can be envisioned to meet the JSDT science goals. The details of the JEO notional payload design approach may be found elsewhere [*JEO 2008 Study Report*, D-48279].

11.1.1 Radiation Effects

There are two major radiation effects to consider when assessing the suitability of a given detector. First, a detector must be able to tolerate the performance degradation that comes from the integral effects of total dose ionization and displacement damage. The progressive accumulation of radiation effects gives rise to progressive changes in detector performance. These changes must not result in an instrument unable to meet measurement requirements. Thus, the DWG reviewed the radiation literature and test reports to understand how key characteristics of a given detector technology degraded as a function of ionizing and displacement damage dose.

Table 11–1 summarizes the expected tolerance of each technology to TID and DDD, including the performance loss that would likely result from that dose. The shielding that is required to ensure that the total dose environment to which the detector is exposed does not exceed the detector tolerance, including the required radiation design factor of 2, is also provided in **Table 11–1**.

The second major radiation effect to be considered when assessing a given technology is the real-time response of a detector to the incident flux of electrons, protons, and photons. Individual radiation particles generate signals within the detector that are similar to signals generated by the science measurement. The magnitude of this response is dependent upon the detector technology and specifics of the detector design and implementation, as well as the details of the instrument system implementation. This transient noise can potentially swamp the science signal during periods of high particle

flux. The DWG examined the transient noise response during Europa orbit for each detector technology as implemented in the notional payload as a function of shielding thickness. The results are summarized in [Table 11–1](#).

Ultimately, one of the two major radiation effects discussed above will be the driving requirement for selection of the shield thickness. The characteristic that drove the recommended shielding allocation for the JEO implementation is highlighted as bold red text in [Table 11–1](#). The last column of the table summarizes the selected shield thickness and the overall expected impact on the instrument as a result of total dose exposure and transient noise effects, as implemented on JEO.

For example, for the combination of HgCdTe focal plane design and operational parameters for the Vis-IR Spectrometer (VIRIS), a 3.0-cm Ta shield was required to adequately mitigate the transient noise impact to an acceptable level during Europa orbit 5 (9 Rj). This level of shielding effectively mitigates any concern for the total dose survivability (both TID and DDD) of the detector. There will be total-dose-induced degradation of the detector performance—such as an increase in dark current—but the degradation expected behind 3.0-cm Ta can be mitigated by additional techniques such as detector cooling.

For all the detector technologies addressed in this report, the DWG concludes that the radiation challenges are well understood. Assuming the recommended shielding allocations and the JEO instrument design approach, there is no significant risk from total dose effects and degradation of science measurements by transient radiation effects can be limited to a tolerable level. For many of the instruments—WAC+MAC, NAC, VIRIS, LA, UVS, INMS, and PPI—the selection of shield thickness was driven by the need to reduce the impact of radiation-induced transient noise. For others—TI and the laser components in LA—the shielding selection

was driven by total dose concerns or by limited total dose testing.

It should be noted that the assessment of transient noise impacts on the science payload was performed for the particle flux received during Europa orbit at 9 Rj. During Io fly-bys, the JEO spacecraft would see a particle flux that is approximately 8 times higher. It is beyond the scope of this report to be completely quantitative about transient noise effects during Io flyby. For example, imager operation during Io fly-by is likely to be quite different than during Europa orbit as exposure times must vary as the fly-by distance and velocity related image smear changes. The trade space between additional shielding, exposure time, and radiation noise transients must be further explored for specific fly-by scenarios. The high albedo for Io, especially in the infrared, allows for much shorter exposure times, and provides additional trade space.

Table 11-1. Summary of total dose survivability, transient noise impact, and recommended shielding allocation for each detector technology as implemented in the JEO notional payload. The driving characteristic for the shield thickness is indicated in **bold blue text**.

Sensor Technology	Total Dose Survivability			Transient Noise Effect							Conclusions (Assumes Recommended Shield)	
	Expected TID Tolerance	Expected DDD Tolerance	Required Shielding with RDF=2	Instrument	Notional Detector Characteristics Relevant to Transient Effects	Transient Radiation Response at 9 Rj With Given Shielding						Recommended Shield
						0.3- cm Ta	0.6-cm Ta	1.0-cm Ta	1.5-cm Ta	3.0-cm Ta		
	(krad Si)	(MeV/g Si)	(cm Ta)								(cm Ta)	
CCD/CMOS	n-CCD: Tested to 80 krad, I _d =920 pA/cm ² @ 20 °C. ¹ CMOS: Tested to 100 krad, I _d =200 pA/cm ² @ 27 °C ⁸	n-CCD MPP: Tested 4 to 6E7 DDD, I _d =56 to 240 pA/cm ² @ 25 °C. ^{2,3} Tested to 1.4E8 DDD, CTE=0.9993 @ -118 °C. p-CCD: Tested 5 to 14E7 DDD, I _d =1–4 nA/cm ² @ 25 °C ^{4,5} Tested to 7.4E8 DDD, CTE=0.99995 @ -93 °C. ^{6,7}	1.0	WAC	13 μm pixel 77 ms exposure	35.66% of pixels corrupted	11.4%	5.6%	2.2%	0.6%	1.0	• Shielding: 1.0-cm Ta (requires TID tolerance to 70 krad Si, DDD tolerance to 1.3E8 MeV/g Si) • Shielding driven equally by total dose survivability and transient noise • Dark current increases from TID and DDD mitigated by cooling detector • CMOS is favored (hardened by design and/or process), but TID and DDD requirement allows for CMOS, p-CCD, and possibly n-CCD.
		MAC		13 μm pixel 7.7 ms exposure	3.6% of pixels corrupted	1.1%	0.6%	0.2%	0.06%	1.0		
		NAC		13 μm pixel 0.77 ms exposure	0.4% of pixels corrupted	0.1%	0.06%	0.02%	0.01%	1.0		
HgCdTe	MWIR HgCdTe detector tested to 1 Mrad, no change in R ₀ . ⁹ CMOS readout similar to visible detector above	LWIR HgCdTe detector tested up to 1E9 DDD with no change in R ₀ @ 78 K. ¹⁰	1.0	VIRIS	27 μm pixel 154 ms exposure	307% of pixels corrupted	98%	48%	19%	5%	3.0	• Shielding: 3.0-cm Ta (requires TID tolerance to 20 krad Si, DDD tolerance to 1.9E6 MeV/g Si) • Shielding driven by transient noise, which mitigates total dose survivability concerns • No dark current data available; mitigation by focal plane cooling

Sensor Technology	Total Dose Survivability			Transient Noise Effect								Conclusions (Assumes Recommended Shield)
	Expected TID Tolerance	Expected DDD Tolerance	Required Shielding with RDF=2	Instru- ment	Notional Detector Characteristics Relevant to Transient Effects	Transient Radiation Response at 9 Rj With Given Shielding					Recom- mended Shield	
						0.3- cm Ta	0.6-cm Ta	1.0-cm Ta	1.5-cm Ta	3.0-cm Ta		
	(krad Si)	(MeV/g Si)	(cm Ta)								(cm Ta)	
Thermopiles	Thermopile detector tested to 10 Mrads with negligible change in performance ¹¹ CMOS readout similar to visible detector above	Thermopile detector: No data, but displacement damage not expected to be a concern for the metal-like thin active area. Gold black absorber could degrade, needs testing CMOS readout similar to visible detector above	0.4	TI	No transient noise effects because thermal energy deposited by bckgrnd radiation is beneath the noise floor of the instrument	---	---	---	---	---	Not a concern	<ul style="list-style-type: none">• Shielding: Nominal 0.4-cm Ta (requires TID tolerance to 300 krad Si)• No transient noise concerns• CMOS readout hardened by design and/or process• DDD testing of gold black absorber on thermopile recommended
Avalanche Photodiodes	Si APDs tested to 300 krads with 10–100X increase in dark current & some loss of sensitivity. ¹²	Tested to 4E9 DDD with 10–100X increase in dark current. ¹²	0.3	LA	<ul style="list-style-type: none">• 0.5-mm² APD active area• 1.5 ms time to return laser pulse• 150 μs range-gating window	198% of laser firings corrupted	~66%	~33%	~13%	~3%	3.0	<ul style="list-style-type: none">• Shielding: 3.0-cm Ta (requires TID tolerance to 20 krad Si, DDD tolerance to 1.9E6 MeV/g Si)• Shielding driven by transient noise, which effectively mitigates all concerns over total dose survivability.• Dark current increases mitigated by detector cooling.• Geiger mode is not recommended for JEO
Diode Laser	No TID concern	Tested to 5.5E9 MeV/g with 6% threshold current shift and no change in QE. ^{13, 14}	0.3	LA	No transient noise effects	---	---	---	---	---	0.3	<ul style="list-style-type: none">• Shielding: 0.3- cm Ta (requires TID tolerance to 400 krads Si, DDD tolerance to 1.3E9 MeV/g Si)• Shielding driven by DDD; no transient noise concern• Shift in laser threshold current mitigated by electronic adjustments
Nd:YAG crystal	Tested to 500 krads with no loss of performance if Cr ³⁺ doped. ¹⁵	Tested to 5 x 20 ¹¹ cm ⁻² with 50-MeV protons w/ no loss of performance ¹⁵ (NIEL not known)	0.3	LA	No transient noise effects	---	---	---	---	---	0.3	<ul style="list-style-type: none">• Shielding: 0.3-cm Ta (requires TID tolerance to 400 krads Si, DDD tolerance to 1.3E9 MeV/g Si)• Shielding driven by TID test limit• No NIEL value found for Nd:YAG, so DDD tolerance not known. Should be calculated.• No performance degradation anticipated

Sensor Technology	Total Dose Survivability			Transient Noise Effect								Conclusions (Assumes Recommended Shield)
	Expected TID Tolerance	Expected DDD Tolerance	Required Shielding with RDF=2	Instrument	Notional Detector Characteristics Relevant to Transient Effects	Transient Radiation Response at 9 Rj With Given Shielding					Recommended Shield	
						0.3- cm Ta	0.6-cm Ta	1.0-cm Ta	1.5-cm Ta	3.0-cm Ta		
	(krad Si)	(MeV/g Si)	(cm Ta)								(cm Ta)	
LiNbO ₃	Tested to 50 Mrad w/ <0.2 dB loss. ¹⁶	No data	0.3	LA	No transient noise effects	---	---	---	---	---	Not a concern	<ul style="list-style-type: none">Shielding: 0.3-cm Ta (requires TID tolerance to 400 krad Si, DDD tolerance to 1.3E9 MeV/g Si)Not a shielding driver; benefits from shielding required by other laser componentsNo TID concerns, but no DDD data found. Should be tested even though TID is likely dominant effect.
Optical Fibers	Tested to 170 Mrads with <0.1 dB/m loss and no sig change in fiber strength. ¹⁷	No data	0.3	LA	No transient noise effects	---	---	---	---	---	Not a concern	<ul style="list-style-type: none">Shielding: 0.3-cm Ta (requires TID tolerance to 400 krad Si, DDD tolerance to 1.3E9 MeV/g Si)Not a shielding driver; benefits from shielding required by other laser componentsNo TID concerns, but no data found for DDDTID expected to be dominate effect
MCP / PMT	No significant total dose effects	No significant total dose effects	Not a concern	UVS	<ul style="list-style-type: none">MCP w/ 160 mm² active area;Assumes 2% efficiency in registering cts from radiation "hits"	8.8E4 cts/s bckgrnd rate	2.8E4 cts/s	1.4E4 cts/s	5.4E3 cts/s	1.5E3 cts/s	1.0	<ul style="list-style-type: none">Shielding: 1.0-cm Ta (requires TID tolerance to 70 krad Si, DDD tolerance to 1.3E8 MeV/g Si)Shielding driven by transient noise; mitigates to an acceptable level within capabilities of detector electronic designBkgrnd rate is for full detector. Pixelation of detector in imaging application reduces effective rate for use in SNR calculationsNo total dose concerns.
				INMS	<ul style="list-style-type: none">18 mm MCP with 1-ns time window;Assumes 100% of particles cause corruption	0.6% A/D samples corrupted	0.2%	0.1%	0.04%	0.01%	0.6	<ul style="list-style-type: none">Shielding: 0.6-cm Ta (requires TID tolerance to 140 krad Si, DDD tolerance to 3.6E8 MeV/g Si)Shielding driven by transient noiseNo total dose survivability concerns
				PPI-Particles	<ul style="list-style-type: none">50 mm MCP w/ ~5 cm² active area;worst-case bckgrnd rateAssumes a 2% efficiency in the PPI registering cts as a result of a radiation particle "hit"	2.7E5 cts/s bckgrnd rate	8.7E4 cts/s	4.4E4 cts/s	1.7E4 cts/s	4.8E3 cts/s	0.6	<ul style="list-style-type: none">Shielding: 0.6-cm Ta (requires TID tolerance to 140 krad Si, DDD tolerance to 3.6E8 MeV/g Si)Shielding driven by transient noise; mitigates to an acceptable level with typical coincidence logic appliedNo total dose survivability concernsPPI-Plasma is similar

Note 1: [Julian and Vaillant 2001]

Note 4: [Hopkinson 1999]

Note 8: [Bogarets et al. 2003]

Note 11: [Foote 2000]

Note 14: [Johnston 2001]

Note 17: [Berghmans et al. 2008]

Note 2: [Hopkinson 1999]

Note 5: [Becker and Elliot 2006]

Note 9: [Lee et al. 2006]

Note 12: [Becker et al. 2003]

Note 15: [Rose et al. 1995]

Note 3: [Becker et al. 2006]

Note 6: [Hardy et al. 1998]

Note 10: [Kelly et al. 2003]

Note 13: [Evans et al. 1993]

Note 16: [Tsang and Radeka 1995]

For Planning and Discussion Purposes Only.

Table 11–2. Summary of SRU characteristics, assuming 3-inch Al shielding (~1.0-cm Ta) allocation.

Sensor Technology	Total Dose & Displacement Damage Tolerance	JEO EOM TID & DDD at Detector Behind Shield (1.0-cm Ta, RDF 2)	Transient Radiation Noise during Europa Science (9Rj) and Io Fly-bys (5Rj) for Notional Detector	Conclusions
CMOS or CCD	CMOS detector for JUNO SRU tested to 34 krad and 1.1×10^8 MeV/g with no significant parametric shifts other than acceptable offset and dark current increases	TID: 70 krad (Si) DDD: 1.3×10^8 MeV/g (Si)	9 Rj: ~71 electrons/s “hit” track window— mag 4.5 or brighter star trackable 5 Rj: ~600 electrons/s “hit” track window— 2.5-mag star will be noisy, 1-mag star detectable given 0.5-degree knowledge	<ul style="list-style-type: none"> • 1-cm Ta shielding allows for use of existing SRU system products in terms of total dose survivability. • Transient noise mitigated by shielding, algorithmic and system-level approaches. • Additional testing to JEO flight environment required

11.1.2 Planetary Protection Effects

Dry heat sterilization is desired as the most practical approach to meeting planetary protection requirements for the baseline JEO mission. Silicon CCDs and CMOS imagers are fairly robust to the temperature and times required for sterilization, but attention must be given to ensure that device packaging materials (i.e., adhesives, ceramic packages, optical coatings, thermal-electric coolers, etc.) will tolerate dry heat sterilization. HgCdTe detectors present a concern for the dry heat sterilization protocol. A proprietary bake-out protocol for military HgCdTe detectors now exists and has been recommended by at least one commercial supplier, but testing is needed to qualify this procedure for scientific imaging. Thermopiles are expected to withstand dry heat sterilization, but the stability of the gold black absorbing layer requires qualification. Si APDs, lasers, laser-related components, and MCP detectors are expected to tolerate the dry heat sterilization protocol quite well, as long as attention is given to packaging.

11.2 Stellar Reference Unit

Given the recommended shielding allocation, there is no significant risk from total dose radiation effects for a JEO SRU and transient radiation effects can be mitigated to an acceptable level, as summarized in [Table 11–2](#). In addition to shielding, the SRU design

relies on a combination of hardware and software mitigation techniques that are similar to solutions investigated on other programs and would require specific implementation for the JEO environment.

11.3 Test As You Fly

Much of the radiation literature reviewed in this report utilizes high-energy proton irradiation to investigate DDD effects in devices. High-energy electrons, however, dominate the JEO environment. Caution must be used in inferring detector performance in the Jovian environment based on existing DDD test results where the irradiation species was not representative of JEO’s expected flight spectra. While the concept of NIEL scaling has often been successful in allowing prediction of device performance in a proton dominated flight environment based on monoenergetic proton test data, there is concern that NEIL scaling can not be extended to comparing proton and electron irradiation degradation for a given DDD. The qualitative nature of the displacement damage created by electrons of approximately 10-MeV and lower is that of mostly isolated point defects, while higher energy electrons, and protons, create a greater number of larger cluster defects [Becker *et al.* 2005, Becker *et al.* 2006]. Srour and Palko [Srour and Palko 2006] have recently identified a “transition NIEL regime” where NIEL scaling breaks down for dark

current damage factors. This transition region encompasses the NIEL values for electrons from energies of a few MeV to several hundred MEV, and is of particular relevance to the Jovian environment.

The implication is that using existing high energy proton test data to gauge dark signal degradation in an electron-dominated DDD environment is not straightforward. The Juno Project has adopted a rigorous test-as-you-fly policy with respect to sensor radiation testing, including irradiation with flight-representative species and energies for TID, DDD, and transient testing, to address this concern. A similar policy is recommended for flight sensors selected for JEO.

A References

- AA-STR product brochure, Selex-Galileo,
http://www.selexgalileo.com/EN/Common/files/Galileo_Avionica/Relazioni_Esterne/Scheda_Prodotto_2/Space_2/STR.pdf
- Bai, Y., Baja, J., Beletic, J., Farris, M., Joshi, A., Lauxtermann, S., Petersen, A., Williams, G. (2008), "Teledyne Imaging Sensors: Silicon CMOS imaging technologies for x-ray, UV, visible and near infrared," Proc. SPIE Conference on Astronomical Instrumentation (Marseille, France).
- Bebek, C., Bebek, C. J., Groom, D. E., Holland, S. E., Karcher, A., Kolbe, W. F., Lee, J., Levi, M. E., Palaio, N. P., Turko, B. T., Uslenghi, M. C., Wagner, M. T., Wang, G. (2002), "Proton radiation damage in high-resistivity n-type silicon CCDs," Proceedings of SPIE vol. 4669, pp. 161 – 171
- Becker, H. N., Miyahira, T. F. and Johnston, A. H. (2003) IEEE Trans. Nucl. Sci., Vol. 50 No. 6, 1974-1981
- Becker, H. N. and Johnston, A. H. (2004), IEEE Trans. Nucl. Sci., Vol. 51 No. 6, 3572-3578
- Becker, H.N., Alexander, J.W, and Elliott, T., (2005), "High-energy electron testing of CCDs for a Jovian science mission," Proc. of SPIE, vol. 5902, pp. 59020Q-1 – 59020Q-11
- Becker, H. N., Elliott, T., and Alexander J. (2006), "Electron-Induced Displacement Damage Effects in CCDs," IEEE Trans. Nuc. Sci. vol. 53, no. 6, pp. 3764-3769.
- Becker, H. N. and Elliott, T. (2006), "Radiation Test Results for Semiconductor Technology Associates STA0100 and STA0120 P-channel CCDs," NEPPP, FY06 Sensor Technology Task Report, JPL Project 102197, JPL Task #3.21.4.
- Becker, H. N., Farr, W. H., and Zhu, D. Q. (2007), IEEE Trans. Nucl. Sci., Vol. 54 No. 4, 1129-1135
- Beletic, J. (2008), Teledyne Imaging Sensors, private communication.
- Berghmans, F., Brichard, B., Fernandez, A.F., Gusarov, A., Van Uffelen, M. Girard, S. (2008), "An Introduction to Radiation Effects on Optical Components and Fiber Optic Sensors", Excerpt from W.J. Bock *et al.*(eds.) Optical Waveguide Sensing and Imaging. Springer, p 127-165
- Bigas, M., Caruja, E., Forest, J., Salvi, J., (2006) "Review of CMOS image sensors," Microelectronics Journal, vol. 37, pp. 433-451
- Blarre, L., Perrimon, N., and Airey, S., (2005), "New Multiple Head Star Sensor (HYDRA) description and development status: a highly autonomous, accurate and very robust system to pave the way for gyroless very accurate AOCS systems," AIAA 2005-5932, AIAA Guidance, Navigation, and Control Conference and Exhibit, 15-18 Aug. 2005.
- Bogarets, J., B. Dierickx, Meynants, G., and D. Uwaerts, (2003) "Total Dose and Displacement Damage Effects in a Radiation Hardened CMOS APS," IEEE Trans. Nuc. Sci. vol. 50
- Claeys C. and Simoen, E. (2002), "Radiation Effects in Advanced Semiconductor Materials and Devices", Springer-Verlag, p 10
- Cole, T. (1998), "NEAR laser rangefinder: a tool for the mapping and topological study of Asteroid 433 Eros," John Hopkins APL Technical Digest, Vol. 19(2), 142-157.
- Cypress Document (2005), "Radiation hardening of Cypress STAR Sensors – AN5001, Cypress Doc. No. 001-14739
- Cypress Data Sheet (2007), "Star1000 1 meg pixel rad-hard CMOS image sensor," Doc. No. 38-05714
- Dale, C., Marshall, P. Cummings, B., Shamey, L., Holland, A. (1993), "Displacement

- Damage Effects in Mixed Particle Environments for Shielded Spacecraft CCDs”, *IEEE Trans. Nucl. Sci.*, Vol. 40(6), pp. 1628-1637
- Dawson, K., Bebek, C., Emes, J., Holland, S., Jelinsky, S., Karcher, A., Kolbe, W., Palaio, N., Roe, N., Saha, J., Takasaki, K., and Wang, G. (2008), “Radiation Tolerance of Fully-Depleted P-Channel CCDs Designed for the SNAP Satellite,” *IEEE Trans. Nuc. Sci.*, vol. 55, pp. 1725-1735
- Dutton, T., Woodward, W. and Lomheim, T., (1997), “Simulation of Proton-Induced Transients on Visible and Infrared Focal Plane Arrays in a Space Environment,” *Proc. SPIE*, vol. 3063, pp. 77-95
- Duvet, L., Martin, D. and Owens, A. (2006), “Current progress of active pixel sensor developments for future European Space Agency planetary and sun observation missions,” *Proc. SPIE* vol. 6276
- Eid, E., Chan, T., Fossum, E. (2001), “Design and Characterization of Ionizing Radiation Tolerant CMOS APS Imager Sensors up to 30 Mrd (Si) Total Dose,” *IEEE Trans. Nuc. Sci.*, vol. 48, no. 6
- Eid, E., Ay, S., and Fossum, E. (2002), “Design of Radiation Tolerant CMOS APS System-on-a-Chip Imager Sensors,” *IEEE Aerospace Conference Proc.*, pp. 4-2005 – 4-2011.
- Evans, B.D., Hager, H.E., Hughlock, B.W. (1993), “5.5 MeV proton irradiation of a strained quantum-well laser diode and multiple quantum-well broadband LED,” *IEEE Trans. Nuc. Sci.* Vol. 40 (6), p 1645.
- Foote, M., Jones, E., and Callat, T. (1998), “Uncooled Thermopile Infrared Detector Linear Arrays with Detectivity Greater than 10^9 cm Hz^{1/2}/W,” *IEEE Trans. Elect. Dev.* vol. 45, pp. 1896-1902, 1998
- Foote, M., and Jones, E. (1998), “High Performance micromachined thermopile linear arrays,” <http://trs-new.jpl.nasa.gov/dspace/bitstream/2014/19459/1/98-0849.pdf>
- Foote, M. (2000), “High Performance Micromachined Thermopile Arrays,” Jet Propulsion Laboratory Internal Report, November 2000
- Foote, M., Kenyon, M., Krueger, T., Schofield, J., McCleese, D., McCann, T., Jones, E., Soll, S., and Dickie, M. (2002), “Linear and 2-D Thermopile Detector Arrays Using High-Z Thermoelectric Materials,” 21st International Conference on Thermoelectrics
- Foote, M., Krueger, T., Schofield, J., McCleese, D., McCann, T., Jones, E., and Dickie, M. (2003), “Space science applications of thermopile detector arrays, *Proc. SPIE*, vol. 4999
- Griscom, D.L. (1995), “Radiation hardening of pure-silica-core optical fibers by ultra-high-dose γ -ray pre-irradiation” *J. App. Phys.* Vol. 77 (10), p 5008.
- Hardy, T., Murowinski, R., and Deen, M. (1998), “Charge Transfer Efficiency in Proton Damaged CCD’s,” *IEEE Trans. Nuc. Sci.* vol. 45, no. 2
- Hariston, A., Stobie, J., and Tinkler, R., (2006), “Advanced Readout Integrated Circuit Processing,” *Proc. SPIE*, vol. 6206
- Henschel, H., Kohn, O., Schmidt, H.U., Bawirzanski, E., Landers, A. (2006), “Optical Fibres for High Radiation Dose Environments.” *IEEE Trans. Nuc. Sci.* Vol. 41 (3), p 1994
- Hopkinson, G. (1996), “Proton Effects in Charge-Coupled Devices,” *IEEE Trans. Nuc. Sci.*, vol. 43, no. 2, pp 614 -627
- Hopkinson, G. (1999), “Proton Damage Effects on P-Channel CCDs,” *IEEE Trans. Nuc. Sci.*, vol. 46, no. 6, pp. 1790 - 1796

- Hopkinson, G. (2000), "Proton induced changes in CTE for n-channel CCD's and the effect on star tracker performance," IEEE Trans. Nuc. Sci., vol. 47, pp. 2460-2464
- Hopkinson, G. (2001), "Proton-induced charge transfer degradation at low operating temperatures," IEEE Trans. Nuc. Sci., vol. 48, pp. 1790-1795
- Hopkinson, G. (2002), "A Radiation Tolerant Video Camera for High Total Dose Environment," IEEE Trans. Nuc. Sci. vol/page xx
- Hopkinson, G. (2003), Sira Electro Optics Limited, "Final Report Radiation Testing of CCD and APS Imaging Devices," p. 84, June please confirm date OK
- Hopkinson, G. (2003), "Comparison of CCD Damage Due to 10- and 60-MeV Protons," IEEE Trans. Nuc. Sci., vol. 50, no. 6
- Hopkinson, G. (2004), "Radiation Effects on a Radiation-Tolerant CMOS Active Pixel Sensor", IEEE Trans. Nuc. Sci. vol. 51
- Hubbs, J., Gramer, M., Arrington, D., Dole, G., Jepson, D., Takeall, S., (2005), "Total Ionizing Dose and Proton Radiation Characterization of Si P-i-N Visible Hybrid Focal Plane Arrays," Proc. SPIE vol. 5902
- Hubbs, J., Marshall, P., Marshall, C., Gramer, M., Maestas, D., Garcia, J., Dole, G., and Anderson, A., (2007), "Lateral Diffusion Length Changes in HgCdTe Detectors in a Proton Environment", IEEE Trans. Nuc. Sci., vol. 54
- HYDRA product brochure, EADS SODERN, http://www.sodern.com/site/docs_wsw/fichiers_communs/docs/HYDRA%20.pdf
- Insoo, J. (2008), private communication
- Janesick, J., Soli, G., Elliot, T., and Collins, S., (1989), "Radiation damage in scientific charge-coupled devices," IEEE Trans. Nuc. Sci. vol. 36, no.1, pp. 572-578
- Janesick, J., (2001), "Scientific Charge Coupled Devices," SPIE Press, ISBN: 9780819436986, Jan. 2001.
- Janesick, J. and Putnam, G. (2003), "Developments and Applications of High-Performance CCD and CMOS Imaging Arrays", Annu. Rev. Nucl. Part. Sci., vol. 53, pp 263-300
- Janesick, J., (2004) "Charge Coupled CMOS and hybrid detector arrays," Proc. SPIE, vol. 5167, pp. 1 – 18
- Janesick, J., Andrews, J. and Elliott, T., (2006), "Fundamental performance differences between CMOS and CCD imagers; Part II," Proc. SPIE, vol. 6276
- Janesick, J., Andrews, J., Tower, J., Gryogon, M., Elliott, T., Cheng, J., Lesser, M., Pinter, J. (2007), "Fundamental performance differences between CMOS and CCD imagers; Part II," Proc. SPIE, vol. 6690
- Janesick, J., Elliott, T., and Tower, J. (2008), "CMOS Detectors: Scientific monolithic CMOS imagers come of age", Laser Focus World, July 2008.
http://www.laserfocusworld.com/display_article/332970/12/none/none/Feat/CMOS-Detectors:-Scientific-monolithic-CMOS-imagers-come-of-ag
- JEO 2008 Study Report, D-48279
- Johnston, A.H. (2001), "Proton Displacement Damage in Light-Emitting and Laser Diodes" *IEEE Trans. Nuc. Sci.* Vol. 48(5), 1713.
- Johnston, A.H., Miyahira, T.F. (2003), "Displacement Damage Characterization in Laser Diodes" *Proc. RADECS 2003: Radiation and its Effects on Components and Systems*, Noordwijk, The Netherlands, ESA SP-536, 3.
- Julian, F., Vaillant, J. (2001), "TH7890M & TH7891M Image Sensors for Star Trackers", 6th Annual European Conf. on Radiation and

- Its Effects on Components and Systems, pp. 462-463
- Kaczmarek, S.M. (1999), "Influence of Ionizing radiation on Performance of Nd:YAG Lasers" *Cryst. Res. Technol.* Vol. 34 (9), p 1183.
- Kelly, M., Ringdahl, E., D'Souza, A., Luce, S., and Cascio, E. (2003), "Proton Irradiation of Large Area $\text{Hg}_{1-x}\text{Cd}_x\text{Te}$ Photovoltaic Detectors for the Cross-track Infrared Sounder," *Proc. SPIE* vol. 4820, pp. 479-490
- Klaasen, K., Clary, M., Janesick, J. (1984), "Charge-coupled device television camera for NASA's Galileo mission to Jupiter," *Opt. Eng.* Vol. 23(3), 334-342
- Klein, C., (1968), "Bandgap Dependence and Related Features of Radiation Ionization Energies in Semiconductor," *J. App. Phys.*, vol. 39, pp. 2029-2039
- Lee, M., Kim, Y., lee, N., Lee, Y., Sivananthan, S. and Lee, H. (2006), "An analysis of gamma radiation effects on ZnS- and CdTe-passivated HgCdTe photodiodes," *Proc. SPIE* vol. 6206
- Liebe, C.C. (2001), "Charged Particle-Induced Noise in Camera Systems," *IEEE Trans. Nucl. Sci.*, Vol. 48(4), pp. 1541-1549
- Magnan, P., (2003), "Detection of visible photons in CCD and CMOS: A comparative view," *Nuc. Instr. And Methods in Phys. Research A*, vol. 504, pp. 199-212
- Marshall, P., Hubbs, J., Arrington, D., Marshall, C., Reed, R., Gee, G., Pickel, J., and Ramos, R., (2003), "Proton-Induced Transients and Charge Collection Measurements in a LWIR HgCdTe Focal Plane Array," *IEEE Trans. Nuc. Sci.*, vol. 50, pp. 1968-1973.
- Marshall, C., Marshall, P., Waczynski, A., Polidan, E., Johnson, S., and Cambell, A. (2004), "Comparisons of proton induced dark current and charge transfer efficiency of n- and p-channel CCDs," *Proc. of SPIE* vol. 5499, pp. 542 -552
- Marshall, C. Marshall, P., Waczynski, A., Polidan, E., Johnson, S., Kimble, R., Reed, R., Delo, G., Schlossberg, D., Russell, A., Beck, T., Wen, Y., Yagelowich, J., and Hill, R. (2005), "Hot pixel annealing behavior in CCDs irradiated at $-84\text{ }^{\circ}\text{C}$," *IEEE Trans. Nuc. Sci.*, vol. 52, no. 6, pp. 2672-2677
- Marshall, C., Marshall, P., Howe, C., Reed, R., Weller, R., Mendenhall, M., Waczynski, A., Ladbury, R. and Jordan, T., (2007), "Comparison of Measured Dark Current Distributions With Calculated Damage Energy Distributions in HgCdTe," *IEEE Trans. Nuc. Sci.*, vol. 54, pp. 1097-1103
- McKelvey, M., Ennico, K., Johnson, R., Marshall, P., McMurray, R., McCreight, C., Pickel, J. and Reed, R. (2004), "Radiation environment performance of JWST prototype FPAs," *Proc. SPIE* vol. 5167, pp. 223-234
- Messinger, S.R., Burke, E., Summers, G., Xapsos, M. Walters, R., Jackson, E. and Weaver, B. (1999), "Nonionizing energy loss (NIEL) for heavy ions," *IEEE Trans. Nuc. Sci.*, vol. 46, pp. 1595-1602
- Morita, Y., Kawakami, W. (1989), "Dose Rate Effect on Radiation Induced Attenuation of Pure Silica Core Optical Fibers" *IEEE Trans. Nuc. Sci.* Vol. 36(1), p 584.
- Norris, J.O.W., Norman, S.A., Tribble, M.J. (1990), "Mechanical Degradation of Polymer-Coated Glass Optical Fibers under γ irradiation" *Proc. SPIE* Vol. 1314, (Testing, Reliability, and Applications of Optoelectronic Devices), p 199
- Pain, B., Hancock, B., Cunningham, T., Seshadri, S., Sun, C., Peddada, P., Wrigely, C., and Stirbl, R. (2004), "Hardening CMOS Imagers: Radhard-by-design or Radhard-by-foundry," *Proc. SPIE*, vol. 5167, pp. 101-110

- Paranicas, C., Mauk, B. H., Khurana, K., Jun, I., Garrett, H., Krupp, N., Roussos, E. (2007), Europa's Near-Surface Radiation Environment, *Geophys. Res. Lett.*, vol. 34, L15103
- Pickel, J. (2003), "Radiation Effects on Photonic Imagers – A Historical Perspective," *IEEE Trans. Nuc. Sci.*, vol. 50, pp. 671-688
- Pickel, J., Reed, R., Ladbury, R., Marshall, P., Jordan, T., Gee, G., Fodness, B., McKelvey, M., McMurray, R., Ennico, K., McCreight, C., Waczynski, A., Polidan, E., Johnson, S., Weller, R., Mendenhall, M. and Schrimpf, R., (2005), "Transient Radiation Effects in Ultra-Low Noise HgCdTe IR Detector Arrays for Space-Based Astronomy," *IEEE Trans. Nuc. Sci.*, vol. 52, pp. 2657-2663.
- Rose, T.S., Hopkins, M.S., and Fields, R.A. (1995), "Characterization and control of gamma and proton radiation effects on the performance of Nd:YAG and Nd:YLF lasers" *IEEE J. Quantum Electron.* Vol. 31(9), p 1593
- Sporea, D. (2004), "Effects of Gamma-Ray Irradiation on Quantum-Well Semiconductor Lasers" *Radiation Effects Data Workshop, 2004 IEEE*, (2004) 137.
- Srour, J. R. (2000), "Universal Damager Factor for Radiation-Induced Dark Current in Silicon Devices," *IEEE Trans. Nuc. Sci.*, vol. 47, no. 6
- Srour, J. R., Palko, J.W. (Dec. 2006), "A Framework for Understanding Displacement Damage Mechanisms in Irradiation Silicon Devices", *IEEE Trans. Nucl. Sci.*, vol. 53, no. 6
- Summers, G., Burke, E., Shapiro, P. and Messenger, S. (1993), "Damage correlations in semiconductors exposed to gamma, electron and proton radiations," *IEEE Trans. Nuc. Sci.*, vol. 40, no. 6, pp. 1372-1379
- Summers, G. P., Walters, R. J. (1993), "Damage Correlations in Semiconductors Exposed to Gamma, Electron and Proton Radiations", *IEEE Trans. Nuc. Sci.* Vol. 40, No. 6, p 372
- Tsang, T. and Radeka, V. (1995), "Electro-optical modulators in particle detectors," *Rev. Sci. Instrum.* Vol. 66, p 3844.
- Waczynski, A., Polidan, E., Marshall, P., Reed, R., Johnson, S., Hill, R., Delo, G., Wassell, E., and Cheng, E. (2001), "A Comparison of Charge Transfer Efficiency Measurement Techniques on Proton-Damaged n-Channel CCD's for the Hubble Space Telescope Wide-Field Camera 3," *IEEE Trans, Nuc, Sci.*, vol. 48, no. 6, pp. 1807-1814
- Williams, G., Vanderwyck, A., and Blazejewski, E., (1987), "Gamma Radiation Response of MWIR and LWIR HgCdTe Photodiodes," *IEEE Trans. Nuc. Sci.* vol. NS-34, pp. 1592-1596
- Wrigley, C., Twiss, P. and Cunningham, T. (2006), "Summary of Radiation Testing of CMOS Visible Focal Plane Arrays," Internal JPL Report.
- Yashima, H. (1982), "Effect of Gamma Radiation on Optical Fiber Strength" *IEEE Trans. Nuc. Sci.* **NS-29**, 1, p 1026.
- Zhao, Y. F., Patwary, A. R., Schrimpf, R. D., Neifeld, M. A., Galloway, K. F. (1997), "200 MeV proton damage effects on multi-quantum well laser diodes", *IEEE Trans Nucl Sci.*, Vol. 44, 1898-1905

B Radiation Behind the Shield and Detector Response to Single Event Effects

The incident electron and proton flux incident on a component behind a nominal 1-cm-thick Ta shield was discussed in §4.1. The response within a detector active volume for silicon and HgCdTe-based detectors was

derived in §4.2. This appendix provides the incident electron and proton flux and the response of these detectors to these single event effects for several additional shield thicknesses (0.3-cm Ta and 3.0-cm Ta).

Table A–1: *Expected electron and proton flux incident on detectors behind a 0.3-cm Ta shield during Europa science (9 Rj) and Io flybys (5 Rj)*

	Electrons	Protons
Flux at 5 Rj	$3.0 \times 10^7 \text{ e/cm}^2\cdot\text{s}$	$3.9 \times 10^4 \text{ p/cm}^2\cdot\text{s}$
Flux at 9 Rj	$2.7 \times 10^6 \text{ e/cm}^2\cdot\text{s}$	$2.1 \times 10^3 \text{ p/cm}^2\cdot\text{s}$
Signal Electrons per “hit” for Si	~1,500	~16,000
Signal Electrons per “hit” for HgCdTe	~10,000	~100,000

Note 1: Estimates incident electron flux based on Integral Flux of 10 MeV external electrons. This external energy is the minimum required to penetrate 0.3-cm Ta.

Note 2: Estimates incident proton flux based on Integral Flux of 50 MeV external protons. This is the minimum energy required to penetrate 0.3-cm Ta.

Note 3: Estimates signal generation for electron “hits” based on 3 MeV average energy for incident electron

Note 4: Estimates signal generation for proton “hits” based on 50 MeV average energy for incident proton

Note 5: Assumes charge collection thickness of 10 μm with an additional geometrical factor of 1.7 (longest pathlength in a 10 μm cube). An additional factor of 1.5 is assumed to account for variations in pathlength and variations in diffusion charge collection.

Table A–2: *Expected electron and proton flux incident on detectors behind a 3-cm Ta shield during Europa science (9 Rj) and Io flybys (5 Rj)*

	Electrons	Protons
Flux at 5 Rj	$2.0 \times 10^4 \text{ e/cm}^2\cdot\text{s}$	$20 \text{ p/cm}^2\cdot\text{s}$
Flux at 9 Rj	$4.6 \times 10^4 \text{ e/cm}^2\cdot\text{s}$	$2 \text{ p/cm}^2\cdot\text{s}$
Signal Electrons per “hit” for Si	See note 3	See note 3
Signal Electrons per “hit” for HgCdTe	See note 3	See note 3

Note 1: Estimates incident electron flux based on Integral Flux of 100 MeV external electrons. This external energy is the minimum required to penetrate 3-cm Ta.

Note 2: Estimates incident proton flux based on Integral Flux of 200 MeV external protons. This is the minimum energy required to penetrate 3-cm Ta.

Note 3: Environmental models are not reliable at electron and proton energies required to penetrate this shield thickness. Therefore, the flux estimates are not reliable and serve only as zero-order estimate. The signal generation estimation is not provided.

C Acronyms and Abbreviations

A	Amperes
ADC	Analog to Digital Converter
APD	Avalanche Photodiode
APL	Applied Physics Laboratory
APS	Active Pixel Sensor
ASIC	Application Specific Integrated Circuit
ATLO	Assembly, Test and Launch Operations
BiSbTe	Bismuth Antimony Telluride
BiTe	Bismuth Telluride
C22	Calisto encounter number 22 (Galileo)
CCD	Charge-Coupled Device
CdTe	Cadmium Telluride
CdZnTe	Cadmium Zinc Telluride
CID	Charge Injection Device
cm	centimeter
CMOS	Complementary Metal-Oxide-Semiconductor
CrIS	Cross-Track Infrared Sounder
CRISM	Compact Reconnaissance Imaging Spectrometer for Mars (Mars Reconnaissance Orbiter)
CS	Charge Share
CsI	Cesium Iodide
CsTe	Cesium Telluride
CTE	Charge Transfer Efficiency
CTI	Charge Transfer Inefficiency
CTIA	Capacitance Transimpedance Amplifier
CTX	Context Camera (Mars Reconnaissance Orbiter)
D*	Detectivity
D _d	Displacement Damage Dose (=DDD)
DDD	Displacement Damage Dose
DSI	Deep Space 1
DWG	Detector Working Group
e	Electron
EJSM	Europa Jupiter System Mission
EOI	Europa Orbit Insertion
FET	Field-Effect Transistor
FIPS	Fast Imaging Plasma Spectrometer (MESSENGER)

FODA	Fiber Optic Delay Assembly
FOV	Field of View
FPA	Focal Plane Array
FPN	Fixed Pattern Noise
g	Gram
GaAs	Galium Arsenide
GEANT4	GEometry ANd Tracking
Gy	Gray
HAS	High Accuracy Sensor
HGA	High Gain Antenna
HgCdTe	Mercury Cadmium Telluride
IMU	Inertial Measurement Unit
InGaAs	Indium Gallium Arsenide
INMS	Ion and Neutral Mass Spectrometer
IPR	Ice Penetrating Radar
IR	Infrared
JADE	Jovian Auroral Distributions Experiment (Juno)
JEDI	Jupiter Energetic-particle Detector Instrument (Juno)
JEO	Jupiter Europa Orbiter
JFET	Junction Field-Effect Transistor
JJSDT	Joint Jupiter Science Definition Team
JPL	Jet Propulsion Laboratory
JWST	James Webb Telescope
LA	Laser Altimeter
LBNL	Lawrence Berkeley National Laboratory
LED	Light Emitting Diode
LET	Linear Energy Transfer
LIDAR	Light Detection and Ranging
LiNbO ₃	Lithium Niobate
LOLA	Lunar Orbiter Laser Altimeter (Lunar Reconnaissance Orbiter)
LORRI	Long Range Reconnaissance Imager (New Horizons)
LRO	Lunar Reconnaissance Orbiter
LROC	Lunar Reconnaissance Orbiter Camera (Lunar Reconnaissance Orbiter)
LWIR	Long Wavelength Infrared
MAC	Medium Angle Camera
MAG	Magnetometer (MESSENGER, Galileo, Juno)
MARCI	Mars Color Imager (Mars Reconnaissance Orbiter)
MCNPX	Monte Carlo N-Particle eXtended

MCP	Multi Channel Plate
MDIS	Mercury Dual Imaging System (MESSENGER)
ME	Mars Express
MESSENGER	MErcury Surface, Space ENvironment, GEochemistry, and Ranging mission
MMM	Xxxx (Chandrayaan)
MOS	Metal-Oxide-Semiconductor
MPP	Multi Pinned Phase
MRO	Mars Reconnaissance Orbiter
MTF	Modulation Transfer Function
MVIC	Multispectral Visible Imaging Camera (New Horizons)
MWIR	Mid Wavelength Infrared
NAC	Narrow Angle Camera
Nd:YAG	Neodymium-doped yttrium aluminum garnet
NEAR	Near Earth Asteroid Rendezvous
NIEL	Non-Ionizing Energy Loss
NLR	NEAR Laser Rangefinder
NMOS	n-channel Metal-Oxide-Semiconductor
p	Proton
PD	Photodiode
PEPE	Plasma Experiment for Planetary Exploration (Deep Space 1)
PEPSSI	Pluto Energetic Particle Spectrometer Investigation (New Horizons)
PG	Photogate
PHD	Pulse Height Distribution
PMT	Photomultiplier Tube
PPD	Pinned Photodiodes
PPI	Particle and Plasma Instrument
QE	Quantum Efficiency
QW	Quantum Well
RbTe	Rubidium Telluride
RDF	Radiation Design Factor
Rj	Jovian Radii
ROSINA	Rosetta Spectrometer for Ion and Neutral Analysis
RS	Radio Science
RTOF	Reflectron-type Time-of-Flight (ROSINA)
RTS	Random Telegraph Noise
SEE	Single Event Effect
SET	Single Event Transient
Si	Silicon

SNAP	SuperNova Acceleration Probe
SRU	Stellar Reference Unit
SSI	Solid-State Imager
SSIRU	Scalable Space Inertial Reference Unit
Ta	Tantalum
TBD	To Be Determined
TI	Thermal Instrument
Ti	Titanium
TID	Total Ionizing Dose
UVIS	UltraViolet Imaging Spectrometer (Cassini)
UVS	UltraViolet Spectrometer
UVS	UltraViolet Spectrograph (Juno)
VIRIS	Vis-Infrared Imaging Spectrometer
VP	Virtual Phase
WAC+MAC	Wide Angle Camera and Medium Angle Camera
WFC3	Wide Field Camera 3